Laboratoire d'études spatiales et
d'instrumentation en astrophysique
L'Observatoire de Paris

University of Belgrade
Faculty of Mathematics

LESIA
Laboratoire d'Études Spatiales et d'Instrumentation en Astrophysique

Ecole Doctorale Astronomie et
Astrophysique d'Ile de France

École Doctorale d'Astronomie & Astrophysique
d'Île-de-France

IN-SITU DUST DETECTION USING RADIO ANTENNAS OF DIFFERENT SPACECRAFT - SPACE OBSERVATIONS AND MODELING

KRISTINA RACKOVIĆ BABIĆ

Doctoral dissertation

Meudon, Belgrade, 2022.

Kristina Racković Babić: *In-situ dust detection using radio antennas of different spacecraft - space observations and modeling*

Laboratoire d'études spatiales et
d'instrumentation en astrophysique
L'Observatoire de Paris

Univerzitet u Beogradu
Matematički Fakultet

Ecole Doctorale Astronomie et
Astrophysique d'Ile de France

NEPOSREDNA DETEKCIJA KOSMIČKE PRAŠINE RADIO - UREĐAJIMA SVEMIRSKIH LETELICA

KRISTINA RACKOVIĆ BABIĆ

Doktorska disertacija

Medon, Beograd, 2022.

Kristina Racković Babić: *In-situ dust detection using radio antennas of different spacecraft - space observations and modeling*

Supervised by:

Karine Issautier,

Directeur de recherche CNRS, Observatoire de Paris, LESIA

Dušan Onić

Faculty of Mathematics, University of Belgrade, Serbia

Jury:

President:

Laurence Rezeau

Professeur, Sorbonne Université, LPP, PSL, Ecole Polytechnique

Co-menthor (French):

Karine Issautier

Directeur de recherche CNRS, Observatoire de Paris, LESIA

Co-menthor (Serbian):

Dušan Onić

Faculty of Mathematics, University of Belgrade, Serbia

Reviewers:

Herve Lamy

Senior Scientist Belgian Institute for Space Aeronomy IASB/BIRA

Christian Mazelle

Directeur de recherche IRAP

Examinators:

Marko Stalevski

Assistant Research Professor Astronomical Observatory - Belgrade, Serbia

Vladimir Zeković

Research Associate, University of Belgrade, Faculty of Mathematics

Department of Astrophysical Sciences, Princeton University

Invited member:

Arnaud Zaslavsky

Sorbonne University and LESIA - Observatoire de Paris

Date of defense: _____

ABSTRACT

Interplanetary dust grains contain important information about the Solar System. Analyzing these particles is an important aspect of the heliosphere study. Dust impacts have been observed using radio and wave instruments onboard the spacecraft since the 1980s. The interaction between the impact-generated plasma cloud and antenna – spacecraft system elements generates the characteristic signal waveform. The present work focuses on the detection and interpretation of the dust generated signals from radio instruments onboard various spacecraft orbiting at 1 AU.

In the first part of the thesis, we aim to develop a model which links the observed electric signals to the dust impact properties. We propose a new model which takes into account the effect of impact - ionization - charge collection and electrostatic-influence. Our model provides an analytical expression for the pulse. It allows us to measure the amount of total ion charge, the fraction of escaping charge, the rise timescale, and the relaxation timescale. The proposed model is simple and convenient for large data fitting. To validate the model, we use the Time Domain Sampler (TDS) subsystem of the STEREO/WAVES instrument, which generates high-cadence time series of voltage pulses for each monopole. Since the beginning of the STEREO mission in 2007, we have collected all the dust events detected by S/WAVES/TDS simultaneously on all three monopoles at 1 AU. Our study confirms that the rise time vastly exceeds the spacecraft's short timescale of electron collection by the spacecraft. Aside from electron dynamics, we also obtained interesting results regarding the cloud's electron temperature. The presented model provides an effective tool for analyzing

dust waveforms, and is applicable for different space missions which investigate the distribution of dust particles, e.g., Solar Orbiter and Parker Solar Probe.

In the second part of the thesis, we focus on the interstellar dust (ISD). Interplanetary and interstellar dust are the two main dust populations at 1 AU. Our objective is to search for interstellar dust by analyzing the data sets collected by STEREO and Wind, starting from the beginning of the missions. Between 2007 and 2012, while being at the solar minimum with a solar dipole pointing southward, all three spacecraft recorded ISD flux at 1 AU. However, before and after that period, the disappearance of the interstellar component was noticeable. The observed change of the impact rate suggests that the flux of interstellar dust at 1 AU varies with the solar cycle. Each time the magnetic dipole field changes its polarity during the solar cycle, small interstellar grains experience focusing or defocusing. Consequently, the dust grains are systematically deflected either towards, or away from the solar magnetic equator plane by the solar wind magnetic field which thus affects the dust dynamics and the total interstellar dust flux in the inner heliosphere. Our study provides the first quantitative description of the time variation of ISD flux at 1 AU.

Key words: heliosphere, dust grains, interplanetary dust, modeling, interstellar dust, analyze

Scientific field: Astronomy and Astrophysics

Scientific subfield: Physics of Heliosphere

RÉSUMÉ

Les grains de poussière interplanétaires contiennent des informations importantes sur le système solaire. L'analyse de ces particules est un aspect important de l'étude de l'héliosphère. Depuis les années 1980, les impacts de poussières sont observés à l'aide d'instruments radio et à ondes embarqués à bord de sondes spatiales. L'interaction entre le nuage de plasma généré par l'impact de poussières et les éléments du système antenne-sonde spatiale génère la forme d'onde du signal. Le présent travail se concentre sur la détection et l'interprétation des observations de poussières à partir d'instruments radio à bord de divers sondes en orbite à 1 AU.

Dans la première partie de la thèse, nous avons développé un modèle qui lie les signaux électriques observés aux propriétés d'impact des poussières. Nous proposons un nouveau modèle qui prend en compte les effets d'impact - ionisation - collection de charges et d'influence électrostatique. Il s'agit d'une expression analytique de l'impulsion. Elle nous permet de mesurer la quantité de la charge ionique totale, la fraction de la charge qui s'échappe, l'échelle du temps de montée et l'échelle du temps de relaxation. Le modèle proposé est simple et pratique pour l'ajustement à un grand jeux de données. Pour valider le modèle, nous utilisons le sous-système Time Domain Sampler (TDS) de l'instrument STEREO/WAVES, qui génère des séries temporelles d'impulsions de la tension à haute cadence pour chaque monopole. Nous avons collecté tous les événements de poussière détectés par S/WAVES/TDS simultanément sur les trois monopoles à 1 AU depuis le début de la mission STEREO en 2007. Notre étude confirme que le temps de montée dépasse largement la courte échelle de temps de

collecte des électrons par la sonde. Outre la dynamique des électrons, nous avons également obtenu des résultats nouveaux concernant la température des électrons du nuage. Le modèle présenté constitue un outil efficace pour analyser les formes d'onde de la poussière et est applicable à différentes missions spatiales qui étudient la distribution des particules de poussière, par exemple sur Solar Orbiter et Parker Solar Probe.

Dans la deuxième partie de la thèse, nous ètudions la poussière interstellaire (ISD). La poussière interplanétaire et la poussière interstellaire sont les deux principales populations de poussière à 1AU. L'objectif de cette partie est d'analyser les jeux de données pour la poussière interstellaire collectés par les sondes STEREO et Wind, sur une grande échelle de temps, dès le début des missions. Entre 2007 et 2012, au moment du minimum solaire avec un dipôle solaire pointant vers le sud, les trois sondes ont enregistré un flux ISD à 1 AU, mais avant et après cette période, la disparition de la composante interstellaire est notable. La disparition d'impacts suggère que le flux de poussière interstellaire observé varie avec le cycle solaire. Lorsque le champ dipolaire magnétique a changé de polarité au cours du cycle solaire, les grains interstellaires ont subi une focalisation ou une défocalisation. Par conséquent, les grains de poussière sont systématiquement déviés vers - ou loin - du plan de l'équateur magnétique solaire, par le champ magnétique du vent solaire, ce qui affecte la dynamique de la poussière et le flux total de poussière interstellaire dans l'héliosphère interne.

Mots clés: heliosphère , grains de poussières , poussières interplanetaires, modèle, poussières interstellaires , analyse

Domaine scientifique: Astronomy et Astrophysique

Sous-domaine scientique: Phisique des Heliosphere

REZIME

Međuplanetarna prašina sadrži važne informacije o Sunčevom sistemu. Neposredna posmatranja kosmičke prašine različitog porekla (od kometa, asteroida, planeta, prirodnih satelita, međuzvezdane materije, itd) rutinski se obalja u okviru postojećih svemirskih misija koje su opremljene odgovarajucim instrumentima. Udari prašine primećeni su korišćenjem radio i instrumenata za detekciju talasa na svemirskim letelicama još 1980-ih godina. Interakcija izmedju oblaka plazme nastalog usled udara čestica prašine i elemenata sistema antena–svemirska letelica, dovodi do pojavljivanja karakterističnog talasanog oblika u signalu. Ovaj rad se fokusira na otkrivanje i tumačenje takvih talasnih oblika u signalu sa radio instrumenata različitih svemirskih letelica koje kruže na udaljenosti od jedne AJ.

U prvom delu rada predstvaljen je teorijski model koji objašnjava proces nastanka pomenutih signala, te nam omogućava da procenimo fizička svojstva prašine na osnovu analize detektovanih talasnih oblika. Predlažemo novi model koji uzima u obzir uticaj jonizacije u prikupljanju naelektrisanja, kao i elektrostatički uticaj. Kroz ovaj model želimo da pokažemo da svojstva detektovanog signala u velikoj meri zavise od lokalnog okruženja letelice, kao i od dinamike oblaka jonizovanog gasa nastalog sudarnom jonizacijom. Predloženi model je jednostavan i pogodan za upotrebu na velikom broju podataka. U svrhu testiranja pouzdanosti modela koristimo podsistem Time Domain Sampler (TDS) instrumenta STEREO/WAVES, koji generiše često ponavljajuće vremenske serije naponskih impulsa za svaki monopol. Naše istraživanje dalo je zanimljive rezultate u vezi sa temperaturom elektrona u oblaku. Predstavljeni model pruža efikasan alat za analizu talasnih ob-

lika prašine i primenjiv je na podatke sa različitih svemirskih letelica.

Drugi deo teze odnosi se na detekciju i analizu međuzvezdane prašine (**ISD**, eng. *interstellar dust*). Međuplanetarna prašina i međuzvezdane prašina predstavljaju dve primarne populacije na udaljenosti od 1 AJ. Naš cilj je analiza podataka za međuzvezdanu prašinu koje prikupljaju STEREO i Wind sateliti, od početka misija. U periodu od 2007. do 2012. godine, kada je zabeležen minimum Sunčeve aktivnosti, a magnetni dipol orijentisan ka jugu, sve tri letelice detektovale su fluks međuzvezdane prašine na 1 AJ. Međutim, pre i nakon tog perioda primetan je nestanak međuzvezdane komponente. Kada magnetno polje promeni polaritet, snop sitnijih zrna međuzvedanih prašine pretrpi svojevrsno fokusiranje ili pak defokusiranje. Shodno tome, kao rezultat dolazi do toga da se zrnca prašine sistematski odguruju ka, ili dalje od ravni Sunčevog ekvatora. To umnogome utiče na dinamiku i ukupan protok međuzvezdane prašine u unutrašnjoj heliosferi. Naše istraživanje pruža prvi kvanitativni prikaz varijacije ISD na 1 AJ tokom vremena.

Ključne reči: heliosfera, čestice prašine, međuplanetarna prašina, modelovanje, međuzveydana prašina, analiza

Naučna oblast: Astronomije i Astrofizika

Uža naučna oblast: Fizika heliosfere

ACKNOWLEDGEMENTS

"U ogromnosti prostora i neizmerju vremena radost je moja što delim jednu planetu i jedno razdoblje sa Nikolom." Thank you!

CONTENTS

1

INTRODUCTION

A surprising amount of dust is present in the solar system. In spite of the fact that you might not be aware of the presence of this dust, you have probably seen its effect : a strange, conical glow emanating from the horizon just before sunrise or after sunset. Interestingly, the Persian poet and astronomer Omar Khayyam may have been referring to this phenomenon when he spoke of the "false dawn" in one of his poems, but the phenomenon is more properly known as the zodiacal light. Researchers have been studying dust in the solar system through ground observations or through space missions.

Solar system travels through interstellar space in our part of the Milky Way Galaxy, a region called the Orion Arm. More specifically, "we" are moving through a mixture of hydrogen and helium atoms called the Local Interstellar Cloud (LIC) (Figure 1). On this journey, dust particles from the LIC can pass through the heliospheric boundary and start their journey across the solar system. Since they originate from the local interstellar cloud, such dust particles are known as interstellar dust (ISD). The micron and submicron sized particles of interstellar dust are naturally influenced by the solar gravity, the interplanetary magnetic field, and the radiation pressure. During the solar cycle, the flow of ISD grains inside the heliosphere is modulated by interactions with the interplanetary magnetic field. The primary sources of interplanetary dust (IDP) are asteroids and comets. An array of physical processes generate, transport, and destroy interplanetary dust particles in the solar system. Dust evolution illustrates how the Universe recycles material in analogous ways to the

daily recycling steps with which most people are familiar: production, storage, processing, collection, consumption, and discarding. The Poynting-Robertson drag causes the particles to slowly move inward as they orbit the Sun, which limits their lifetimes. IDPs close to the Sun are mainly lost through mutual collisions, sputtering, and sublimation. Through these loss processes, atoms, molecules, nanometer, and sub-micron sized particles are generated locally. Ionized atoms and molecules accelerate outward by interacting with the solar wind magnetic field. β - meteorites are formed from these sub-micron sized dust grains, which are accelerated outward due to solar radiation pressure dominating gravity. Some planetary systems exhibit interesting dust particle phenomena. The main rings of Saturn are composed of boulders as well as dust particles. Neptune, Jupiter, and Uranus also have dusty rings. Due to ongoing bombardment from IDPs and micrometeoroids, airless bodies, like moons and asteroids, emit dust particles. In summary, by detecting and analyzing dust particles, we can learn about the dynamics in the solar system. The initial motion of the particle, the particle's material properties, the surrounding plasma, and the magnetic field determined its arrival at the dust detector.

Cosmic dust in our solar system can be studied in various ways. Laboratory experiments can be used to examine samples arriving at or passing through the Earth's vicinity. This applies to micrometeorites collected at the surface, interplanetary dust particles collected in the stratosphere, as well as natural and anthropogenic cosmic dust collected in low Earth orbit. The large orbital velocities of dust particles in interplanetary space make intact particle capture difficult. Instead, in-situ dust detectors are generally devised to measure parameters associated with the high-velocity impact of dust particles on the instrument and then derive the physical properties of the particles (usually mass and velocity). Few interplanetary missions have flown dedicated and well-calibrated dust instruments in recent decades (e.g., Helios,
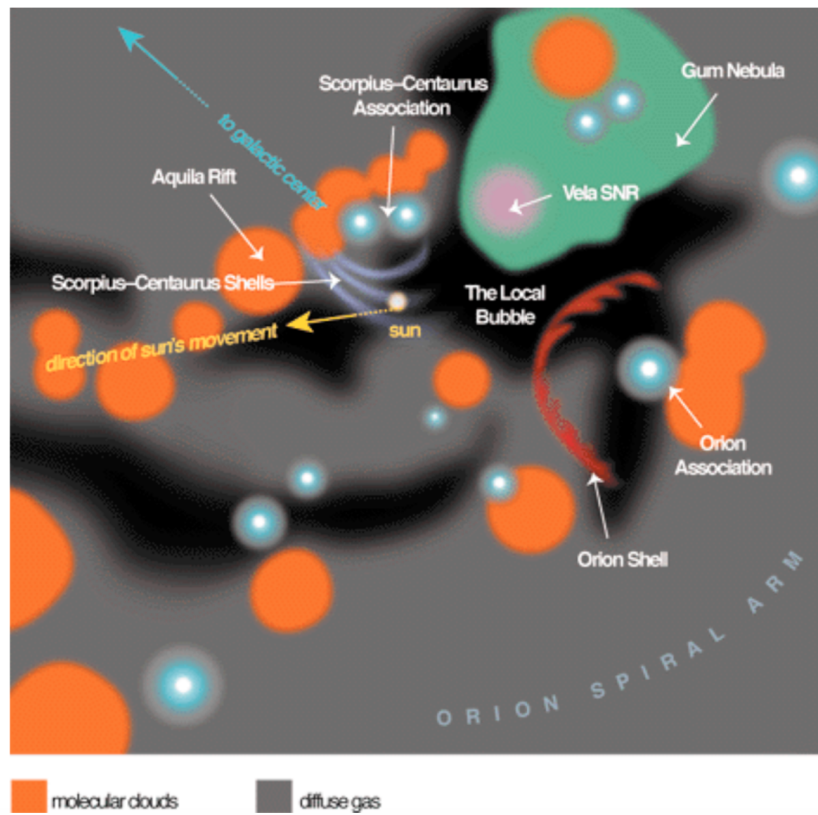
Figure 1: The galactic environment within 500 pc of the Sun. Currently, the Sun is passing through the Local Interstellar Cloud, represented by violet, which is flowing away from the Scorpius-Centaurus Association of young stars. Local Bubble (colored black) is a low-density hole in the interstellar medium where the LIC resides. In the near vicinity, high-density molecular clouds, including the Aquila Rift, surround star-forming regions (highlighted in orange). A region of hot ionized hydrogen gas is the Gum Nebula (green). Inside the Gum Nebula is the Vela Supernova Remnant (depicted in pink) which is expanding to create fragmented shells of material like the LIC.

Image Credit: P. C. Frisch, University of Chicago

Pioneer 10, Pioneer 11, Giotto, Galileo, Ulysses, Cassini). Heliophysics missions, however, often carry antenna-equipped plasma wave instruments. Since Voyager's flyby of Saturn, such instruments have been known to be sensitive to dust impacts. It turns out that dust detection by antennas is complementary to measurements by dedicated dust instruments. Their larger collection area (the entire spacecraft surface) also allows them to gather more statistics on dust populations with lower fluxes. However, the utility of dust detection data by antenna instruments has been limited due to the lack of a detailed understanding of how dust impacts generate electrical signals that can be measured. Hence the importance of developing models of how signals are generated to be able to link the electric signals observed to the physical properties of the dust impact. A vastly accepted explanation is one where dust impacts the spacecraft body and generates clouds of ions and electrons through a process known as impact ionization. Still, a lot of questions remain open on this subject. Thus, different models, ideas, and laboratory experiments are developed in order to gain a better understanding of the process.

This thesis will be focused on in-situ radio detection of dust on various spacecraft. The data we used came from three missions, Wind, STEREO, and Solar Orbiter. The Wind spacecraft was launched with the goal of studying the solar wind upstream of Earth. A solar observation mission, STEREO consists of two twin spacecraft orbiting the Sun at 1 AU. Solar Orbiter is novel mission, launched in 2020, with the goal to study the vicinity of the Sun as close as 0.3 AU. In all three missions, the probes are equipped with radio instruments equipped of electric antennas connected to a sensitive receivers. This thesis involved developing a simple model for dust signal generation. The model takes into account all the effects of charge collection by the spacecraft and the electrostatic influence from charges in its vicinity. The reliability of the model was evaluated using STEREO data. Throughout the years,

each mission collected a large amount of dust related measurements. Taking advantage of extensive data sets from Wind and STEREO mission, ISD flow can be followed over different periods of solar activity. The second part of the thesis is dedicated to this study.

The thesis is organized as follows. Next chapter outlines the dust populations that can be observed in – situ within the solar system, followed by a description of the fundamental physical processes responsible for dust evolution. In addition, dust particle detection and analysis instruments, as well as their history in previous missions, are described. Chapter 3 is based on the paper from Rackovic Babic et al., 2022 (Article A). A summary of the theoretical work presented in the paper is presented in the chapter, along with an application to STEREO data and a discussion of the results. In Chapter 4, after a general overview of the ISD population at 1 AU, in – situ detection and their general properties, the dust data from Wind and STEREO A and B probes are analyzed. Based on long–term solar cycle variations, the ISD contribution to each data set is estimated. The results obtained during this thesis project are summarized in Chapter 5.

DUST IN THE SOLAR SYSTEM

Let us begin by introducing the population we will deal with in this thesis. Dust grains are a common constituent of the Solar System. It is common for dust particles to form as a result of the fragmentation of larger solid bodies. Small quantities of dust are transported into the Solar System from the interstellar medium. The vicinity of comets as well as ring systems, magnetospheres, and atmospheres of planets are also home to dust particles of various origins. The following chapter provides an overview of two major dust populations found in the Solar System, followed by a discussion of the forces that affect dust grains. The characteristics on dust particles can be obtained through various detection methods, including the observation of scattered solar radiation, thermal emission, or in situ measurements. This chapter discusses dust detection methods as well.

2.1 DUST POPULATION

Before we introduce the dust detection methods, we will summarize the current understanding of the Solar System dust environment. Figure 2 illustrates the different dust components and dust interactions near the Sun. Interplanetary dust population (IDP) and interstellar dust (ISD) are two primary dust populations in our Solar System. There are differences between these two groups in terms of origins, dynamics, and composition. As a result of various impact dust detectors flown on various spacecraft in the past, a great deal of our knowledge of dust comes from in-situ dust detection methods. First
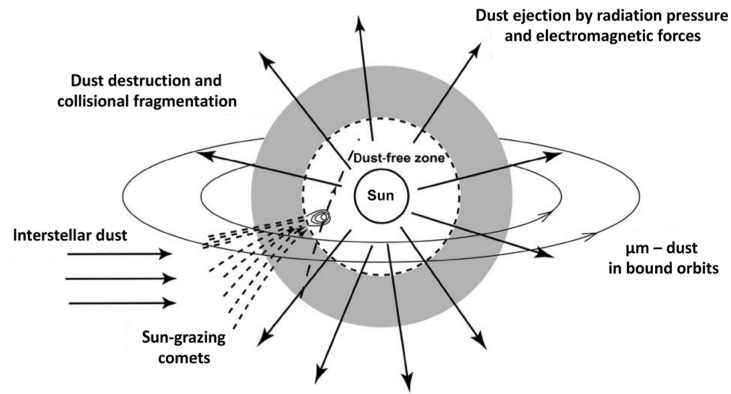
Figure 2: An illustration of the different dust components and dust interactions near the Sun. A large fraction of dust is destroyed in the inner heliosphere, in sublimation and other destruction processes, and this generates a dust-free zone.
Image Credit: Mann et al., 2019

available data sets cover a heliocentric distance range between 0.3 and 5 AU, obtained by the dust particle experiments during milestone missions such as Galileo, Ulysses, Helios, Cassini (Grun et al., 1993; Gurnett et al., 2004; Bougeret et al., 1995). The properties of interplanetary dust have been examined through in–situ or remote optical sensing observations over the past few decades. First indications about the presence of interstellar dust in the Solar System were provided by the Ulysses mission, which allowed us to investigate this dust population further (Grun et al., 1993).

Mutual collisions, sputtering, and sublimation are the major dynamic processes of dust grains close to the Sun. Interplanetary dust particles can be identified by their parent bodies and the dynamical interactions that lead to their orbital evolution. They are mainly generated by collisions in the asteroid belts, Kuiper objects, and various comets populations (Figure 3). The large grains, larger than micrometres, orbit the Sun in Keplerian orbits and are mostly fragments of asteroids and comets. Such particles are produced in dust–dust colli-

sions for which the rates increase with decreasing distance from the Sun. Therefore, as their distance from the Sun decreases, their velocities and number density increase. Fragments smaller than a micrometre typically are pushed outward by radiation pressure and deflected by electromagnetic forces (see Section 2.2) (Mann and Czechowski, 2004; Mann et al., 2010).

In addition to the IDP, a stream of interstellar particles passes through the Solar System originating from the Local Interstellar Cloud (LIC) (Grun et al., 1993). ISD particles stream into the inner heliosphere from an interstellar upstream direction and move roughly parallel to the ecliptic plane (Mann et al., 2010). The radiation pressure force repulsion allows only the large interstellar dust grains to reach the inner heliosphere. A more detailed analysis of the ISD population will be presented in Chapter 4. In order to accomplish such a task, STEREO and Wind data will be used.

There is also a mass-based approach to dust classification. Assuming that the dust particles are compact spherical particles with a bulk density of 2.5 g.cm^{-3} the given masses can be converted to sizes, and vice versa. Table 1 presents the dust types with their corresponding masses and radii. *Meteors*, the most popular, are light phenomena caused by solid particles entering the atmosphere of the Earth from space. The approximate mass ranges are $> 10^{-1}$kg for fireballs, 10^{-8}kg $< m < 10^{-1}$kg for optical meteors, and $< 10^{-5}$kg for radio meteors (Mann, 2009). *Meteoroids* are solid objects that move in space between the planets, with masses of $m < 10^{-8}$kg. *Meteorites*, the solid remains of meteoroids that reach the surface of the Earth without being completely vaporized; their masses range from 10^{-3}kg $< m < 10^4$kg. *Zodiacal dust* particles are responsible for generating Zodiacal light brightness; brightness is roughly proportional to dust cross-sectional area per unit volume in space and orig-

Name	mass	radius
Meteors fireballs	$m > 10^{-1}kg$	$r > 2cm$
Optical *meteors*	$10^{-8}kg < m < 10^{-1}kg$	$100\mu m < r < 2cm$
Radio *meteors*	$m < 10^{-5}kg$	$r < 0.1cm$
Meteoroids	$m < 10^{-8}kg$	$r > 100\mu m$
Meteorites	$10^{-3}kg < m < 10^{4}kg$	$0.5cm < r < 25cm$
Zodiacal dust	$10^{-15}kg < m < 10^{-8}kg$	$0.5\mu m < r < 100\mu m$
β - *meteoroids*	$10^{-15}kg < m < 10^{-18}kg$	$90nm < r < 140nm$
Nanodust	$m < 10^{-18}kg$	$1nm < r < 100nm$
Interstellar dust	$m < 10^{-12}kg$	$0.1\mu m < r < 0.4\mu m$

Table 1: The dust types list with corresponding masses and radii (assuming a spherical grain of radius r and mass density $\rho = 2.5 \ gcm^{-3}$).

inates from masses of $10^{-15}kg < m < 10^{-8}kg$. β - *meteoroids* are dust grains strongly influenced by radiation pressure and as a result, move in hyperbolic orbits in the interplanetary medium; mass range interval $10^{-15}kg < m < 10^{-18}kg$. *Nanodust* is usually described with 3 external dimensions in the size range of 1–100 nm; mass range $m < 10^{-18}kg$. *ISD* mass range for those observed in –situ $m < 10^{-12}kg$. If $m < 10^{-19}kg$ particle is deflected from entering the Solar System (Mann et al., 2000). The categories reflect the properties and methods of detection.
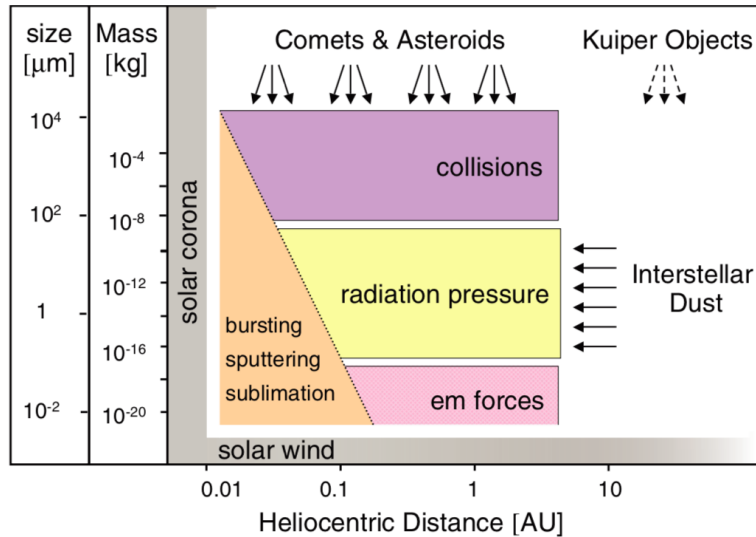
Figure 3: An illustration of dust in different masses and sizes in the **solar** system corresponds to dominant forces and effects.
Image Credit: Mann et al., 2010

2.2 DUST DYNAMICS

Interactions between dust grains and their environment are likely to influence grain dynamics. Gravitational force, radiation pressure, Poynting - Robertson force, a solar wind drag, and the Lorentz force are the main forces acting on dust grains. Each of these forces has a different contribution depending on the radial distance from the Sun, the geometric shape, as well as the composition of the dust grain. Figure 3 depicts the production and loss mechanisms as well as the dominating dynamical processes of dust particles in the solar system as a function of dust size and heliocentric distance. These forces will be briefly summarized in the following paragraphs.

- *Gravitation forces* In a Solar System where more than 99 % of the mass is concentrated in the Sun, it makes sense to assume that the Sun is the primary source of gravity. When a dust grain of mass m_{dust} is located in the Solar gravitational field, the gravitation force acting on the grain is:

$$\mathbf{F_{grav}} = \frac{-GM_{\odot}m_{dust}}{|\mathbf{r}|^3}\mathbf{r},$$ (1)

where $M_{\odot}$ is the Sun's mass and G the gravitational constant. This is a radial force that is directed toward the Sun.

The Solar System is also a home for planets and other massive bodies that can be the gravitational source. In the present work, we completely neglect the effect of the gravitational force of these sources since we interest ourselves only in the dust particles in the vicinity of the Sun. However, if we are inside the influence sphere of a planet, however, dynamics change entirely since, in this case, the dominant gravitational potential is the planet's one, not the Sun's. Planet influence sphere radius can be presented as

$$r_{influence} = D\left(\frac{M_p}{M_{\odot}}\right)^{2/5},$$ (2)

where M_p is the mass of the planet, located at the distance D from the Sun. For our study, using measurements from STEREO and Solar Orbiter, we will never be as close as this distance to the planet so we can neglect this effect.

- *Radiation pressure* Radiation pressure is the mechanical pressure exerted upon any surface due to the momentum exchange between the object and the electromagnetic field. Electromagnetic radiation can be viewed in terms of particles (photons) rather than waves. Poynting (1903) demonstrated that dust grains react with photons from the Sun to create pressure which affects dust movement in the solar system. The expression of this force in terms of non-relativistic dust grains that absorb and scatter sunlight was proposed by Burns et al., 1979. This force depends on

the wavelength of the incoming light, the heliocentric distance, the optical surface properties, the grain shape, and it acts radially. Photons move at the speed of light and acquire a momentum $p = \frac{h}{\lambda} = \frac{E_p}{c}$ where p is momentum, h is Planck's constant, λ is wavelength, c is speed of light in vacuum and $E_p = h\nu$ is energy of the photon for the frequency ν. Accordingly, the associated force will be

$$F_{rad} = \frac{P_\odot(\nu)}{c}. \tag{3}$$

where $P_\odot$ corresponds to the power that the Sun emits at frequency ν. Following is an expression for the radiation pressure force onto a dust grain of cross section S that takes into account the decrease of this power as the square of heliocentric distance r, the scattering of light, and the solar Planck curve

$$\mathbf{F_{rad}}(\mathbf{r}) = \frac{P_\odot S Q_{pr}}{|\mathbf{r}|^3 c}\mathbf{r}, \tag{4}$$

Q_{pr} presents the efficiency of radiation pressure accommodated by the solar spectrum. In contrast to the gravitational force that attracts particles towards the Sun, radiation pressure repels particles from the Sun.

- *Poynting–Robertson effect* Poynting-Robertson effect results in dust grains slowing down since their energy and angular momentum are dissipated, causing them to drift towards the Sun. Radiation pressure tangential to grain motion is responsible for this effect. Dust that is small enough to be affected by this drag, but too large to be blown away from the star by radiation pressure, spirals slowly into the star, where the grain finally evaporates.Thus, the dust grain spirals slowly into the star while its orbital speed increases continuously. A Poynting–Robertson force equals **to**

$$F_{PR} = \frac{r^2 L_\odot}{4c^2}\sqrt{\frac{GM_\odot}{R^5}}, \tag{5}$$

where c is the speed of light, r is the radius of the grain, G is the universal gravitational constant, $M_\odot$ is the mass of the Sun, $L_\odot$ is the solar luminosity and R is the orbital radius of the grain. The Poynting-Robertson effect affects the long-term evolution of dust orbits, thereby reducing their orbital radii.

- *Solar wind drag* A solar wind is expanding through our solar system up to a radius greater than 100 AU. When a solar wind proton collides with a dust grain, momentum is transferred from the solar wind protons to the dust grain. The interaction between them is analogous to radiation forces, depending on the cross section of the dust grain, the surface chemical composition, and the proton momentum flux density. With increasing heliocentric distance, the solar wind proton interaction intensity decreases due to the variation of the proton number density as r^{-2}. Therefore, the ratio between the proton pressure and the radiation pressure (Eq.3) is mostly independent of r, but it depends on the proton velocity; this ratio has been found from in-situ measurements at 1 AU to be about 10^{-4} (Gustafson, 1994).

- *Lorentz force* The Lorentz force on a charge q moving with the velocity **V** relative to the field **B** is

$$\mathbf{F_{Lorentz}} = q\mathbf{V} \times \mathbf{B}, \tag{6}$$

In the heliocentric frame, the magnetic field **B** is convected by the solar wind at the speed $\mathbf{V_{sw}}$. If $\mathbf{V_g}$ is the heliocentric grain velocity, the Lorentz force becomes

$$\mathbf{F_{Lorentz}} = q(\mathbf{V_g} - \mathbf{V_{sw}}) \times \mathbf{B}. \tag{7}$$

$\mathbf{V_g} - \mathbf{V_{sw}}$ is the expression of the relative velocity of dust relative to the solar wind, if $\mathbf{V_{sw}}$ is expressed in the same heliocentric frame. As the dust particles move through the magnetic field they see the Lorentz force acting on them alternately changing direction as they pass through the current sheet. Depending on dust's q/m ratios, particles can be accelerated up to the solar wind speed and ejected from the solar system by the Lorentz force (Horanyi (1996) and Mann and Czechowski (2004)).

It is common to introduce the β-ratio between the forces due to gravitation and radiation pressure, in order to evaluate their relative strength. Because of the same dependence on the gravitation and radiation pressure forces on the heliocentric distance, the β-ratio is independent of r and is a function of parameters like the grain radius, the grain chemical composition, the grain shape and the grain material density. From Eq. 4 and Eq. 1 the expression of the β-ratio can be derived **as**

$$\beta = \frac{|\mathbf{F_{rad}}|}{|\mathbf{F_{grav}}|} = \frac{Q_{pr}SP_{\odot}}{GM_{\odot}m_{dust}c}.$$ (8)

One can see that the β function depends of the grain mass, but it also constrains the material properties of the dust grains. The dust grain shape is usually assumed to be spherical with a typical density of 2.5 grams per cubic centimeter (Draine and Lee, 1984). This dust grain model is commonly used for both interplanetary and interstellar dust. Even more, this model may not be too far of the actual reality, at least for the large grains responsible for the Zodiacal light scattering, since it can be used to reproduce key characteristics of zodiacal light scattering (Giese, 1973).
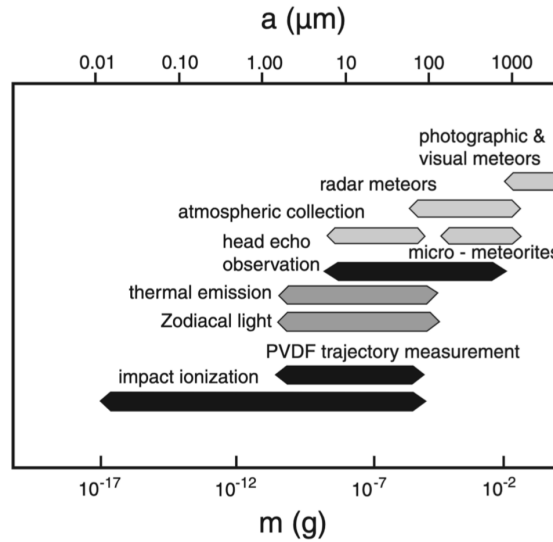
Figure 4: The different ranges of dust grain masses detectable by the different detection methods.

Image Credit: Mann et al., 2006

2.3 DETECTION METHODS

By understanding the size and spatial distribution of dust particles as well as their dynamical properties and compositions properties, we can gain a better understanding dynamics inside the solar system. The presence of the ISD grains in the Solar System, for example, is a proof that it cannot be considered as a closed isolated system in the interstellar medium. Additionally, ISD grains contain crucial information about the past physical conditions that once governed their formation since they are witnesses to their past formation.

A variety of detection methods can be used to obtain the main features about dust particles, including thermal emission, the observation of scattered solar radiation, and in situ measurements. Figure 4 provides an overview of the various detection methods that can be applied depending on the size and mass of the particle.

As an example, cosmic dust in the inner heliosphere can be observed by observing zodiacal light, which is sunlight scattered by interplanetary dust particles. As a result of photometry, polarization, and spectroscopic observations, one can determine their sizes, densities, and spatial distributions (Mann et al., 2006). Due to their low flux, larger particles ($>$ 100 μm) can be observed individually only through remote sensing observations, for instance, by meteor radars, when the particles enter Earth's atmosphere. Particles in the micron and sub-micron size range have sufficiently large fluxes for in situ detection using instruments carried on space missions. In – situ dust grain detection measurements are based on their surface charge, or on the consequences of their impacts at high speeds on a target (Auer (2001) and Grün et al. (2005)). Detectors based on the principle of impact ionization are most widely used, although, there are other methods that can be used as well. In particular, radio instruments, composed of antenna connected to a radio receiver enable us dust measurements. We focus on that method in this thesis.

2.3.1   *Dust detectors*

Throughout history, dust detection instruments onboard spacecraft have evolved. First detectors were based on the dust penetration impact. Nowadays, in – situ dust grain detection measurements are based on their surface charge. Here are some of the main types of dust detection instruments onboard space probes.

In the early days of dust exploration, dust detectors were based on the effect of penetration of grains of dust. Originally, they were designed to assess how dust grains would impact space probes in the Earth orbit. Dust impacts are measured by their rate of passing
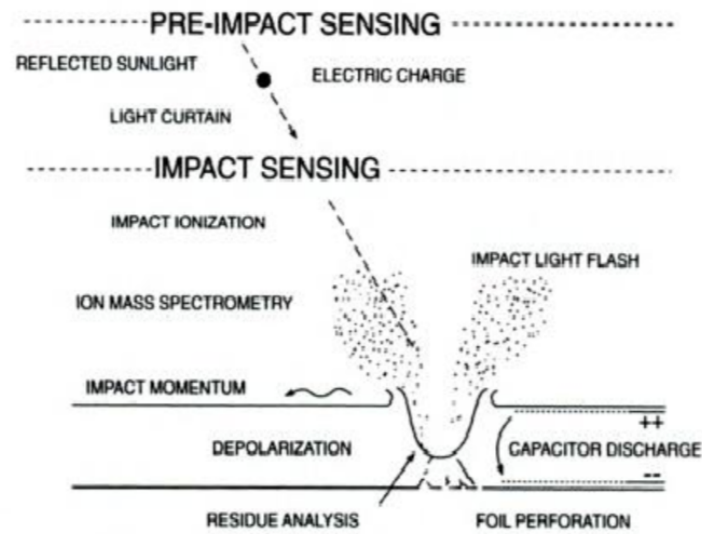
Figure 5: An illustration of in − situ detection methods of dust impacts.
Image Credit: Grün et al., 2001

through a target, and their detection range is between 10^{-13} and 10^{-9} kg. Based on what is predicted as a result of grain penetration, there are four categories of those detectors. First, those made up of cells containing pressurized gas whose pressure decrease indicates that a grain of dust has perforated the wall of a cell (McDonnell, 1978). Second, the ones which consist of capacitors whose discharge indicates that dust particles have penetrated the surface electrode of the capacitor (Zel'Dovich (1968)). Third, the ones detecting the perforation of a target sheet with the help of the charges emitted by the edges of the perforation hole and the dust particles. The impact ionization was considered for the first time in this method. These charges are separated and collected thanks to an electric field maintained between the target sheets and an array of sensors (Berg and Richardson, 1969). The last but not the least, those whose target sheets were polarized. An impact of a grain of dust would cause a total depolarization inside and at the ends of the perforation hole. A rapid electrical impulse is induced by

local volume depolarization (Simpson and Tuzzolino, 1985).

Second-generation detectors rely on impact ionization to achieve better sensitivity. A schematic illustration of the impact ionization detection method is shown in Figure 5. It is possible to measure the mass, impact velocity, trajectory, electrical charge, and chemical composition of dust grains using these instruments. Generally, the main assumption is that the dust grain hits the spacecraft with high velocity (faster than a few kilometers per second). As a result of the impact, the impact triggers a shock wave, which shatters, vaporizes, and ionizes the dust as well as the material of the target, where an impact crater forms. In the vicinity of the impact, crater material forms the cloud (Auer, 2001; Grün et al., 2001). The ions and free electrons thus produced are separated using an electric field, and then these charges are collected by electrodes and converted into an electric signal. The mass and speed of the particle responsible for the impact determine the amplitude and the rise time of the signal. Additionally, the mass spectrum of the released ions provides information about the particle's chemical composition.

Several missions, which have carried dedicated dust instruments, have been flown on since the beginning of the space age. Among them are Helios, Ulysses, Galileo, and LADEE (Lunar Atmosphere and Dust Environment Explorer) (Grun et al., 1985, 1993; Srama et al., 2004; Horányi et al., 2014). There is now a good deal of evidence that space missions equipped with dust instruments can provide a detailed in situ characterization of dust populations within the solar system; including their dynamics and composition characteristics, to study microscopic solid particles. In order to properly calibrate the detectors, high-velocity impacts on a target are simulated in the laboratory to determine the relationship between the measured electrical signal and dust grain properties. Particles used during calibration and

the impact surface composition play a significant role in determining the precision of dust grain properties obtained from electrical signals. The detection area of these instruments is generally $\sim$ 0.01m². In terms of dust grain mass, the detection range is between 10^{-19} and 10^{-11} kg. Such a dust detection method has many advantages, but its main disadvantage is its limited impact detection area.

2.3.2 *Radio instruments*

With the Voyager mission, it became apparent that dust impacts on spacecraft produce measurable electrical signals, which may be used to detect dust in situ. In 1982, the Voyager 1 and 2 space probes used a radio instrument to detect dust for the first time in the Saturn dust rings. This discovery paved the way for an entirely new method of detection of dust grains, with a radio receiver. After Voyager 1 and 2 (Aubier et al., 1983; Gurnett et al., 1983; Meyer-Vernet et al., 1986; Gurnett et al., 1997), antenna dust detection has been demonstrated on several other missions, including Wind (Malaspina et al., 2014; Wood et al., 2015; Kellogg et al., 2016), Cassini (Kurth et al., 2006; Meyer-Vernet et al., 2009, 2017; Ye et al., 2014; Ye et al., 2016a; Ye et al., 2018), STEREO (Zaslavsky et al., 2012; Thayer et al., 2016), Juno (Ye et al., 2020), MMS (Vaverka et al., 2018; Vaverka et al., 2019), Solar Orbiter (Zaslavsky et al., 2021), Parker Solar Probe (Malaspina et al., 2020).

A radio instrument primarily is used to detect electromagnetic waves emitted by distant sources, as well as to diagnose in–situ the ambient plasma. Due to their sensitivity to local electric field fluctuations, electric antennas can be used as in-situ detectors. Radio instruments consist of electric antennas connected to a sensitive receiver, covering a large frequency range, and allow the collection, sampling, and real-
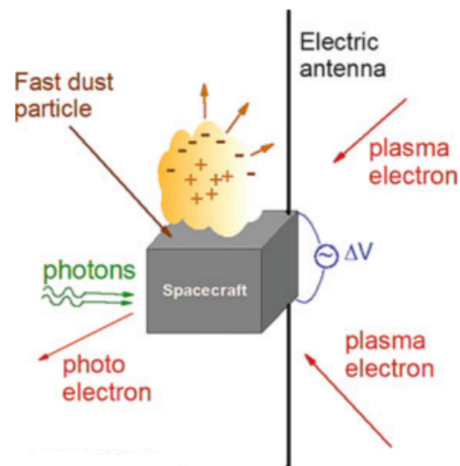
Figure 6: Principle of in situ measurements with an electric antenna onboard a spacecraft in a dusty plasma. Dust impacts at fast speed produce partial ionization of the dust and target, generating an expanding plasma cloud. As a result, voltage pulses are produced whose analysis reveals some dust properties.

Image Credit: Meyer-Vernet and Zaslavsky, 2012

time transmission of observed events (Bougeret et al., 2008; Gurnett et al., 2004).

Figure 6 illustrates the different charging processes responsible for the spacecraft polarization, and how impact ionization can perturbate these processes to produce transistent in the spacecraft potential. The instrument can then be used to measure electrical potential pulses caused by high-speed impacts of dust grains on the space probe at low frequencies (Zaslavsky, 2015). From the 1980's until the present day, several physical mechanisms have been proposed to explain how dust particles produce electrical signals. The first proposed models (Aubier et al., 1983; Oberc et al., 1990) relate to charging mechanisms that can lead to voltage signals, charging an antenna or charging a spacecraft. The models illustrate the importance of the system geometry, the impact cloud geometry, and whether the measurements are

in monopole or dipole mode. According to these and subsequent proposed models, voltage pulses result from the generation of free electric charges resulting from impact ionization after hypervelocity dust particles hit a spacecraft.

This type of dust detection relies on impact ionization. Previously, when we presented second-generation dust detectors, we discussed such a process. The same process can be found here, fast particle hits target, but the targets themselves have changed. Rather than a specially designed dust detector, it is the body of the spacecraft. The potential impacting area is larger, the material of the target varies from mission to mission, and the target's charge can differ. What remains the same, there is no doubt that in the case of a grain of dust colliding with the probe's body (or electric antennas), the impact's velocity V_{impact} influences the outcome. Increasing impact speeds lead to increasing impact energy implying that the entire grain is eventually consumed by the vaporization and ionization processes. Whereas V_{impact} is large enough, $V_{impact} > 10 \ \mathrm{kms^{-1}}$, the impact is violent enough for the grain of dust to be completely disintegrated and ionized in addition to creating a micro crater. Furthermore, the same outcome occurs, and that is the formation of an expanding plasma cloud in the crater vicinity.

The most important result of the collision is the formation of a plasma cloud. Charge from the cloud affects the equilibrium potentials of the antennas and probe body. Similarly to conventional ionization impact instruments (such as the dust detectors mentioned earlier), some of the charge created by the plasma cloud is collected by the target. Consequently, an electrical pulse is created whose duration is related to the perturbation and to the response of the impacted surface. Such electrical pulses are strongly influenced by the characteristics of the impact grain, as well as by the spacecraft's charge. The most im-

portant characteristics of the dust grain in this process are their mass m and speed V. Overall, free charge produced, Q, can be described by the empirical relation

$$Q_{[C]} \simeq \alpha m^{\beta} V^{\gamma}, \tag{9}$$

given by McDonnell, 1978. The parameters α, β, and γ are determined by the velocity of the impact particle, the composition of the target and the particle, as well as the impact geometry. According to McBride and McDonnell, 1999 it is possible to estimate these parameters, for impacts on aluminum, as follows:

$$Q_{[C]} \simeq 0.7 m V^{3.5}, \tag{10}$$

where $m[\text{kg}]$ and $V[\text{kms}^{-1}]$. A recent experiment conducted by Collette et al., 2014 on the effect of hypervelocity on materials relevant to the STEREO spacecraft, supported the estimation. The experiment showed that, the selection of spacecraft material does not substantially influence charge yield at $V_{impact} \simeq 10 \text{kms}^{-1}$ and may only affect it within a factor of 2–5 at $V_{impact} \geqslant 50 \text{kms}^{-1}$. It is commonly assumed that $\gamma \sim 3.5$, which is suitable for STEREO probe as well.

Charged particles from the impact cloud can be re-collected by the spacecraft or escape to free space, determined by the surface potential of the spacecraft. In the solar wind, spacecraft are usually positively charged due to the strong photoelectron current they emit because of their exposition to the Sun's UV radiation. As a result, it is likely that the spacecraft attracts electrons while repelling positive ions from the impact-produced cloud. A change in the spacecraft potential amplitude $\delta V_{sc} \sim Q/C_{sc}$ is produced by the recollection of total charge Q from the cloud by the spacecraft's surface of capacitance C_{sc}. Electric field radio instruments can be operated as a monopole, where the voltage difference between an antenna boom and the spacecraft body is measured, or a dipole, where the voltage difference between

two antenna booms is measured. It has been noted that the amplitude of the generated voltage pulse measured by monopole antennas is significantly larger than that measured by the dipole antennas (Meyer-Vernet, 1985; Meyer-Vernet et al., 2014). The low sensitivity of the dipole came from the fact that it is essentially the spacecraft potential that is varying while the antenna's one stays roughly constant.

Recent advances in the performance of radio detectors have allowed us to gain an improved understanding of the mechanisms that generate voltage pulses. Missions such as Wind (Bougeret et al., 1995), Cassini (Gurnett et al., 2004), or STEREO (Bougeret et al., 2008) have provided us a large number of electric waveforms that are direct characteristic of dust impacts. As a result of the large amount of available data, more sophisticated physical mechanisms have been suggested. Zaslavsky, 2015 proposed a description of the response of a spacecraft to the collection of electric charges generated after the hypervelocity impact of a dust grain. He attributed voltage signals to electron collection, but was unable to explain the observed rise time of signals. Meyer-Vernet et al., 2017 demonstrated that the electrostatic influence of positive ions in the vicinity of the spacecraft needs to be considered and that the positive charge timescale controls the pulse rise time. An analysis of spacecraft charging processes in various plasma environments and an application to dust impacts on MMS is presented by Lhotka et al., 2020. A few models have been developed on the basis of the antenna signal generation processes in the laboratory. Collette et al., 2015 identified three mechanisms for signal generation: induced charging, antenna charging, and spacecraft charging. According to the O'Shea et al., 2017 numerical analysis, the antennas can only collect charge from impacts that occur in close proximity to the antenna base. Recently, Shen et al., 2021 developed a detailed electrostatic model for a generation of antenna signals, applicable to waveforms measured in the laboratory using a dust accelerator, but neglected the plasma effect.

In this thesis, we will present a model, which, for the first time, takes into account all the effects of charge collection by the spacecraft and electrostatic influence from charges in its vicinity. We also compared the present model to the previously used model. This study was published in Rackovic Babic et al., 2022 (see Article A). Main results of this work and large part of the text was transposed from the paper in the following Chapter 3.

MODEL FOR DUST IMPACT VOLTAGE SIGNALS, APPLICATION TO S/WAVES DATA

This chapter is based on the paper from Rackovic Babic et al., 2022 (Article A). We will make an overview of the main theoretical work included in this paper. We will also present the application to STEREO data and put some additional results.

As already mentioned, dust impacts on spacecraft produce measurable electrical signals. Such transient voltage signals are generated by the expanding plasma cloud after impact ionization. The antenna instruments can measure these voltage signals that provide information about dust particles. Through photoelectron emission and the collection of electrons and ions from the ambient plasma, the antenna and spacecraft acquire equilibrium potentials in space. Depending on the relative magnitudes of the charging currents, the equilibrium potential may be positive or negative. Naturally, the equilibrium potential affects the expansion of the impact ionization plasma cloud. Dust impact produce transient perturbations of this equilibrium potential, which then relax back to their equilibrium values over time scales which are characteristic of the environment. It is of great importance developing models of how signals are generated to be able to link observed electric signals to the physical properties of the impacting dust. The obtained parameters from fitting the model to measured waveforms can provide information on dust particles and characteristics of impact-generated plasma cloud, as well as characteristics of the ambient plasma environment. Several models have attempted to describe the physical mechanisms leading to the generation of voltage signals

measured by antennas. We will first introduce the evolution of physical models and then present our model that takes impact – ionization – charge collection and electrostatic – influence effects into account.

Gurnett et al., 1983 assumed that a significant fraction α of the impact charge electrons is collected by the antennas with positive equilibrium potentials. The voltage measured by the antenna is then $V = Q/C_a$, assuming C_a is the capacitance of the antenna. In this case the charge collected on the antenna is $Q = \alpha Q_{impact}$. Aubier et al., 1983, based on the observations during Saturn-Voyager 2 encounter, noticed that the electrostatic noise on the antennas resulting from the passage of electrons and ions near the antennas leads to order of magnitude much lower than the observed values. The author explains this phenomena by introducing the shot noise due to grain impacts. Namely, they proposed that the detected shot noise is consequence of dust grains impacting the spacecraft and/or antennas with velocity high enough that the grains will be vaporized and ionized. Before impact, the grain had a much lower charge than the one resulting from the impact. The part of the charge will be subsequently collected by the target (spacecraft body) with a small time constant. Therefore, this generates a shot noise that is more intense than if the grains were not vaporized and ionized. As a result of this approach, one can see the importance of the spacecraft body in the impact ionization process. Additionally, based on the observations from Voyager 2, Aubier et al., 1983 showed that dust impacts can also be detected as wide-band noise in the antenna signals' power spectrum. Later, Gurnett et al., 1987 examined the collection of the impact charge by the spacecraft in the dipole configuration, on the example of the Voyager 2 spacecraft. In this case, a small fraction of the spacecraft voltage is measurable by the antennas, given as $V = \gamma Q_{impact}/C_{sc}$, where C_{sc} is the spacecraft capacitance, and γ is the electronics coefficient. Oberc, 1996 expanded on these ideas and include sensing of the charge separation electric field as potential mech-

anism s that can lead to the generation of voltage signals. According to him, the antennas detect the electric field of the ion cloud during the expansion of the impact plasma. Based on this model, the impact plasma expands over time as it moves away from the impact area. Electrons decouple from the plasma cloud during the expansion, leaving behind a cloud of slower ions with a positive space charge potential on the order of the electron temperature. As a result, the antennas detect the separated electric field of the cloud. Moreover, Oberc, 1996 noted that the measured signals generated by antenna charging would also strongly depend on the impact geometry, i.e., where the impact occurs in relation to the antennas and the spacecraft. Signals generated by spacecraft charging, however, would not be affected by impact geometry. In addition, spacecraft charging is the dominant mechanism for monopole antennas. Alternatively, for dipole antennas, the measured signals come from differential charging and sensing the separated electric fields. A floating potential perturbation model was proposed by Zaslavsky, 2015, based on data collected by the WAVES instrument and monopole antennas. According to this model, both the spacecraft and the antenna recollect some fraction of the impact plasma. The measured signal is the difference between the voltage perturbations on the antenna and the spacecraft due to charge collection. The characteristic shapes of the measured waveforms are determined by the different discharge time constants through the ambient plasma corresponding to the two elements. According to Meyer-Vernet et al., 2017, an analytical model can be used to calculate antenna signal rise times. It is suggested that the electrons in the impact plasma acquire an isotropic velocity distribution due to their high thermal speed. As a result, half of the electrons move toward the spacecraft instead of away from it after charge separation. In a review article by Mann et al., 2019 one can find the description of the different approaches for antenna signal generation processes.

3.1   MODELING OF THE VOLTAGE PULSE

As a next step, we will present a theoretical model for the generation of voltage pulses caused by dust grains colliding with a spacecraft. The proposed model is an extension of the work of Zaslavsky, 2015, which gave a description, in the linear approximation, of the response of a spacecraft (or an antenna) to the collection of electric charges generated after the hypervelocity impact of a dust grain. His model proved its capability to reproduce most of STEREO's dust impact shapes, confirming the electron collection as the main mechanism through which voltage signals are produced. However, it was unable to explain the observed rise time of the signals – of the order of some tens of microseconds, despite a quick analysis of the electron dynamics, showing that the collection time should be much smaller. This point, which was left as a question mark in Zaslavsky, 2015, was explained by Meyer-Vernet et al., 2017, who showed that the effect of electrostatic influence from the positive ions in the vicinity of the spacecraft needs to be taken into account. Indeed, the negative change in the spacecraft's potential due to the collection of charges, $-Q$, from an initially neutral cloud is almost exactly compensated for by the electrostatic influence from the charges, $+Q$, left unscreened in the close vicinity of the spacecraft. Therefore, Meyer-Vernet et al., 2017) showed that the rise time of the pulse is not controlled by the electron dynamics time scale but by the positive charge time scale, that is, the time needed for the positive charges to be screened by the photoelectrons or the ambient plasma or to move far enough from the spacecraft for the influence effect to become negligible and for the drop in the potential due to electron collection to become apparent. Another consequence of the influence effect, which was noted in the same paper, is the possible occurrence, on very short time scales, of a precursor in the voltage pulse associated with the electron dynamics. Indeed, a fraction of the electrons

escaping away from the spacecraft will leave some ion charge un-screened, inducing a positive change in the spacecraft potential that is not compensated by the collection of negative charges – resulting in the observation of a short voltage pulse, on a typical time scale of the electron dynamics. Mann et al., 2019 summarized these processes without providing quantitative analysis on the basis of a description through "escaping currents." In a nutshell, the charge conservation in a volume V bounded by a surface S that includes the spacecraft is

$$\frac{dQ}{dt} = -\iint_s \mathbf{j} \cdot \mathbf{dS} \tag{11}$$

$$\frac{dQ}{dt} = -I_{out} + I_{in} = -I_{dust}(t) - I_{ph} + I_{sw} + ... \tag{12}$$

Here I_{dust} is the impact ionization charge leaving the volume V. One takes for I_{dust} whatever "dynamical" model, including electrons and ions motions with their different time scales (described in Section 2.1 of Article A). Finally, I_{dust} is the current leaving the surface S, rather than the collection current (hence leading to the difference in time scales with Zaslavsky, 2015).

3.1.1 *Model for a signal generated by a dust impact on the spacecraft*

This section provides a brief overview of our model. A detailed explanation can be found in the rticle A, Section 2. The following paragraphs will guide you through the ideas that led us to the final equation.

The potential of an element is a linear combination of the charge carried by each of the elements. Considering the system composed exclusively of the dust plasma cloud, of charge Q_{cloud} and potential

$\varphi_{\texttt{cloud}}$, and the spacecraft (indices sc), the linearity of the problem translates into the existence of a matrix Λ such that

$$\begin{pmatrix} \varphi_{\texttt{cloud}} \\ \varphi_{\texttt{sc}} \end{pmatrix} = \begin{pmatrix} \Lambda_{\texttt{cloud}} & \Lambda_{\texttt{cloud,sc}} \\ \Lambda_{\texttt{sc,cloud}} & \Lambda_{\texttt{sc}} \end{pmatrix} \begin{pmatrix} Q_{\texttt{cloud}} \\ Q_{\texttt{sc}} \end{pmatrix}. \tag{13}$$

Here Λ is the inverse of the capacitance matrix, $\Lambda = C^{-1}$, also known as the elastance matrix. Since the size of the spacecraft is very large with respect to the size of the dust cloud that influences it (so its self capacity is much larger), the change in self-capacitance of the spacecraft due to the presence of the cloud in its vicinity can be neglected, thus

$$\Lambda_{\texttt{sc}} \simeq C_{\texttt{sc}}^{-1} \simeq \frac{1}{4\pi\epsilon_0 R_{\texttt{sc}}}, \tag{14}$$

where $C_{\texttt{sc}}$ is the spacecraft capacitance in a vacuum and $R_{\texttt{sc}}$ its typical size. This parameter is then a good approximation independent of the position of the dust cloud concerning the spacecraft. The evaluation of $\Lambda_{\texttt{sc,dust}}$ requires more exertion. The evaluation offered by Jackson, 1962, which assumes the dust cloud is a point charge, and the spacecraft is a sphere, neglects many factors. Especially the fact that the dust-spacecraft interaction does not occur in a vacuum, and that the interaction potential is screened by the photoelectron sheath. Hence, we chose to model the mutual elastance, $\Lambda_{\texttt{sc,cloud}}$, by

$$\Lambda_{\texttt{sc,cloud}}(r) = \frac{1}{C_{\texttt{sc}}} F(r), \tag{15}$$

where $F(r)$ is a decreasing function (with a typical length scale, $\lambda_{\texttt{ph}}$, the screening length of the photoelectron sheath), with limiting values of 1 for $r \to 0$ and 0 for $r \to \infty$. Evidently, there are many options available, though we decide to choose

$$F(r) = \exp(-r/\lambda_{\texttt{ph}}). \tag{16}$$

With our model for electrostatic influence, we can study the effects of a transient as a dust impact on the SC potential. In order to do this, we use Eq. (13) to write the derivative of the spacecraft potential,

$$
\frac{d\varphi_{sc}}{dt} = \Lambda_{sc}\frac{dQ_{sc}}{dt} + \frac{d}{dt}\left(\Lambda_{sc,cloud}Q_{cloud}\right). \tag{17}
$$

The first term of the right-hand side in this equation corresponds exactly to what was solved in the paper by Zaslavsky, 2015. The second term of the right-hand side of the equation was not taken into account in this paper. However, it contains the description of the effects of electrostatic influence.

The solution of Eq. (17) can be obtained by linearizing the expression for the currents around the equilibrium value, $\varphi_{sc,eq}$, of the potential, as was done in Zaslavsky, 2015. The potential perturbation, $\delta\varphi_{sc} = \varphi_{sc} - \varphi_{sc,eq}$, is then found to evolve according to the first-order linear differential equation

$$
\frac{d}{dt}\delta\varphi_{sc} + \frac{1}{\tau_{sc}}\delta\varphi_{sc} = \frac{1}{C_{sc}}\left(I_{collected} + \frac{d}{dt}\left[F(r(t))Q_{cloud}(t)\right]\right), \tag{18}
$$

where τ_{sc} is the linear relaxation time of the spacecraft potential

$$
\tau_{sc} = \frac{C_{sc}T_{ph}}{en_e\nu_eS_{sc}}, \tag{19}
$$

with T_{ph} the photoelectron sheath temperature expressed in electronvolts, n_e the local plasma electron density, $\nu_e = \sqrt{kT_e/2\pi m_e}$ the electron mean velocity divided by 4, with k the Boltzmann's constant, e the electron charge and m_e the electron mass, respectively. T_e the local plasma electron temperature and S_{sc} the spacecraft conductive surface in contact with the surrounding plasma. The solution of Eq. (18), assuming the spacecraft is in equilibrium with the surrounding plasma when $t \to -\infty$, is

$$\delta\varphi_{sc}(t) = \frac{1}{C_{sc}} e^{-t/\tau_{sc}} \int_{-\infty}^{t} \left(I_{collected}(t') + \frac{d}{dt'} \left[F(r(t')) Q_{cloud}(t') \right] \right)$$
$$e^{t'/\tau_{sc}} dt'. \tag{20}$$

This expression can be used in a pretty general manner to model the shape of the pulse – as long as the linear assumption is fulfilled, which is the case for the large majority of the impacts recorded.

We aim to make a simple model, depending on only a few parameters. The model that is adapted to a fitting of massive spacecraft data sets. Several assumptions were implemented in order to accomplish our goal. We implemented the simple assumption that the ions are streaming out of the spacecraft surface with a constant velocity, v, and that the motion of the electrons occurs fast enough that it can be considered as instantaneous. We also consider the possibility that the photoelectrons in the sheath neutralize the ion cloud, since this effect was shown to be important by Meyer-Vernet et al., 2017. For the function F – which is proportional to the mutual elastance of the cloud-spacecraft system, we use the exponential model Eq. (16) with a cutoff length λ_{ph} on the order of the photoelectron sheath Debye length. Since we consider ions streaming freely out of the spacecraft, the spacecraft-ion cloud distance is given by $r(t) = vt$, with v a constant. Therefore, the term accounting for electrostatic influence reads

$$\frac{d}{dt} \left(F(r(t)) Q_{cloud}(t) \right) = \left(\frac{dQ_{cloud}}{dt} + \frac{1}{\tau_d} Q_{cloud} \right) e^{-t/\tau_d}, \tag{21}$$

where $\tau_d = \lambda_{ph}/v$ is the ion cloud dynamics time scale, characteristic of its transit time (or expansion time) in the photoelectron sheath. Now one must model the effects related to the motion of the cloud's electrons. For this, we use the following equation, which expresses the change in the cloud's charge due to currents of electrons from it and

the neutralization of the cloud by the photoelectrons on a typical time scale τ_{ph}:

$$\frac{d}{dt}Q_{cloud} + \frac{1}{\tau_{ph}}Q_{cloud} = -I_{collected}(t) - I_{escaped}(t), \qquad (22)$$

where $I_{escaped}$ is the current of charges escaping away from the spacecraft.

The assumption that the escape and collection of the electrons is instantaneous (the "massless electron assumption") translates into the following expressions for the currents

$$I_{collected}(t) = -(1-\epsilon)Q\delta(t), \qquad I_{escaped}(t) = -\epsilon Q\delta(t), \quad (23)$$

where $Q > 0$ is the total amount of free charges released in the impact ionization process, ϵ is the fraction of electrons escaping away from the spacecraft, and $\delta(t)$ is the Dirac's delta function. It is then clear that one must have, from the Eq. (22),

$$Q_{cloud}(t) = e^{-t/\tau_{ph}} \int_{-\infty}^{t} \left(-I_{collected}(t') - I_{escaped}(t')\right) e^{t'/\tau_{ph}} dt'$$
$$= Qe^{-t/\tau_{ph}}H(t),$$
$$(24)$$

where $H(t)$ is Heaviside's step function.

All the source terms appearing in the right-hand side of Eq. (20) have now been given by an explicit expression, and it is straightforward to compute the integral. The potential perturbation obtained is

$$\delta\varphi_{sc}(t) = \left[\frac{\epsilon Q}{C_{sc}}e^{-t/\tau_{sc}} - \frac{Q}{C_{sc}}\frac{1}{1-\tau_i/\tau_{sc}}\left(e^{-t/\tau_{sc}} - e^{-t/\tau_i}\right)\right] H(t).$$
$$(25)$$

where $\tau_i = \tau_d\tau_{ph}/(\tau_d + \tau_{ph})$ is the characteristic rise time of the pulse. It is on the order of the smaller of the ion characteristic time scale, τ_d,

and the time, τ_{ph}, for the cloud to collect enough ambient photoelectrons to be able to shield its charge, Q (Meyer-Vernet et al., 2017).

The shape of this time profile is comparable to that of the dust signal (see Fig 1. Article A). The next step is to test the model's reliability. To accomplish this, we will use the S/WAVES data.

3.2 STEREO/WAVES TIME DOMAIN SAMPLER DATA

We performed an analysis of dust grain impacts from both of the STEREO satellites in order to validate the proposed model's reliability. STEREO (Solar TErrestrial RElation Observatory) is a NASA mission that was launched in 2006. The primary objective of the mission is to study coronal mass ejections. STEREO is composed of two twin spacecraft orbiting the Sun at approximately 1 AU, one following the Earth (STEREO B) and one leading (STEREO A). Data from S/WAVES radio receivers has proven to be very valuable for studying dust (Meyer-Vernet et al., 2009; Zaslavsky et al., 2012). The S/WAVES radio instrument is constituted by three orthogonal 6 m long antennas connected to a sensitive radio receiver. The antennas are operated in a monopole mode. The instrument can perform observations in the frequency range 2.5 KHz to 17 MHz (Bale et al., 2008; Bougeret et al., 2008). The Time Domain Sampler (TDS) is a subsystem of the S/WAVES instrument that generates high-cadence time series of voltage pulses for each monopole. The TDS subsystem quickly and continuously samples the voltage on the antennas and simultaneously records the results via four channels (Bougeret et al., 2008). Each of the three S/WAVES monopole antennas is connected to the input channel of its own. The fourth channel is connected to a pseudo-dipole obtained from the analog difference between two monopoles and is of no significance for our data analysis. As part of our work, we use TDS
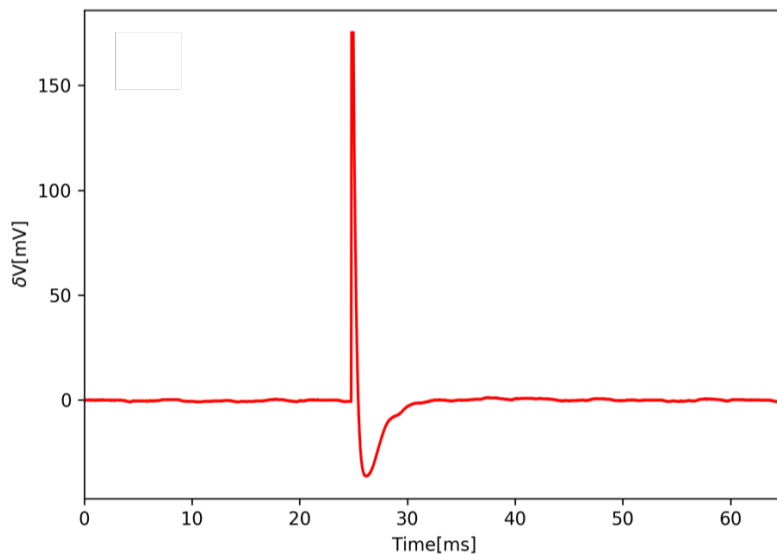
Figure 7: An example of a voltage impulse recognized as dust impact detected by the TDS on-board STEREO.
Image Credit: Rackovic Babic et al., 2022

data to examine how voltage changes occur when dust grains impact the spacecraft.

Two TDS data sets are available: (1) the *TDSmax* data give the maximum amplitude or peak signal detected on the antennas each minute; and (2) the *TDS Events* data set provides complete voltage time series captured by the instrument with a sampling rate of a few μs (Zaslavsky et al., 2012). The TDS Events data set will be used in this Section. The TDSmax data set will be introduced and used later, in Section 4. Measurements can be conducted in several modes with different time resolution and total event duration. For our study snapshots with a time resolution of 4 or 8 ms (which constitute the vast majority of the signals) are used. They correspond to snapshot durations of 65 ms and 130 ms. Signals with a high amplitude are automatically selected for telemetry out of a continuously recorded waveform. Analysing the electrical waveforms of the TDS Events one can reveal that they con-

tain a variety of signals with distinctly different shapes. The observed signals include variations in electric potential due to inhomogeneities of local plasma density. Panels a–c of Figure 2 in the Article A illustrate some of the types of signals present in the data: plasma waves oscillating at the local plasma frequency (Langmuir waves), plasma waves around the local cyclotron frequency, and low-frequency density fluctuation. The impact of energetic particles such as protons and electrons from the Solar System or coming from galactic origin can also produce an electric field signal. All these signals are well known and have been the subject of many works (e.g, Kellogg et al., 1996, Bale et al., 1998, Henri et al., 2011, Malaspina et al., 2011). Figure 7 shows a signal of characteristic shape recognized as a dust impact signal (Zaslavsky et al., 2012). This signal is characterized by an abrupt increase in voltage followed by a rapid relaxation to equilibrium potential. There are two distinct types of these signals: a strong peak detected by one monopole or a similarly shaped signal appearing simultaneously on all three antennas. Our study is focused on signals almost simultaneously generated on all three antennas.

3.2.1   *Survey of TDS dust data*

The TDS waveform sampler on-board both STEREO satellites has observed a large number of voltage pulses interpreted as dust impact signatures since the launch of the mission. We examines TDS events recorded from 2007 to 2018 for STEREO A and from 2007 to 2015 for STEREO B. As already mentioned, the data set contains snapshots of a wide variety of phenomena. Therefore, we needed to find a way to automatically identify only very sharp and impulsive events, recognized as dust events, in between all those other varieties of occurrences.

We intended to collect a large number of data for our work. In order to detect dust signals on all monopoles simultaneously, a first step was to find a way to perform automatically detection. It is necessary to define the range of signal amplitudes generated under the influence of the dust. In order to avoid signals which involve saturation of the instrument, the upper limit amplitude of the signal is 175 mV. The lower limit is at 15 mV, so that we can clearly distinguish the characteristic peak. We know that only dust and some waves produce the signal with the same order of magnitude on all three antennas. If we take into consideration only signal from two monopoles, one can see that majority of dust events are located inside the ellipse (Fig. 3 from Article A). If we add a third antenna signal, we can presume that the dust events simultaneously by each monopole will be inside the cone. We select all data in a cone of aperture $\alpha = 17°$. In parallel with dust events, we have also detected Langmuir waves with a corresponding amplitude. Insofar as we limit the signal to just two points at an intersection of one-third of the height of the maximum amplitude, we eliminate all Langmuir waves from our obtained dust database. An auto-detection algorithm that meets all the above criteria was tested using three months of observations over which several dozen measurements of dust impacts were made. As a result, dust-related events were found to be detected with high accuracy by this approach. Then we applied our algorithm to the entire TDS Events data set.

We have gathered all dust events measured on all three monopoles simultaneously with maximum amplitudes between 15 and 175 mV from the TDS Events data set in 2007–2018 to create a single database. We will take a brief look at the data base obtained. Our earlier statement stated that we were searching for signals with characteristic shapes appearing almost simultaneously on all three monopoles. Nevertheless, the obtained data base can be categorized into several groups based on their characteristics. As shown in Figure 8, these events can
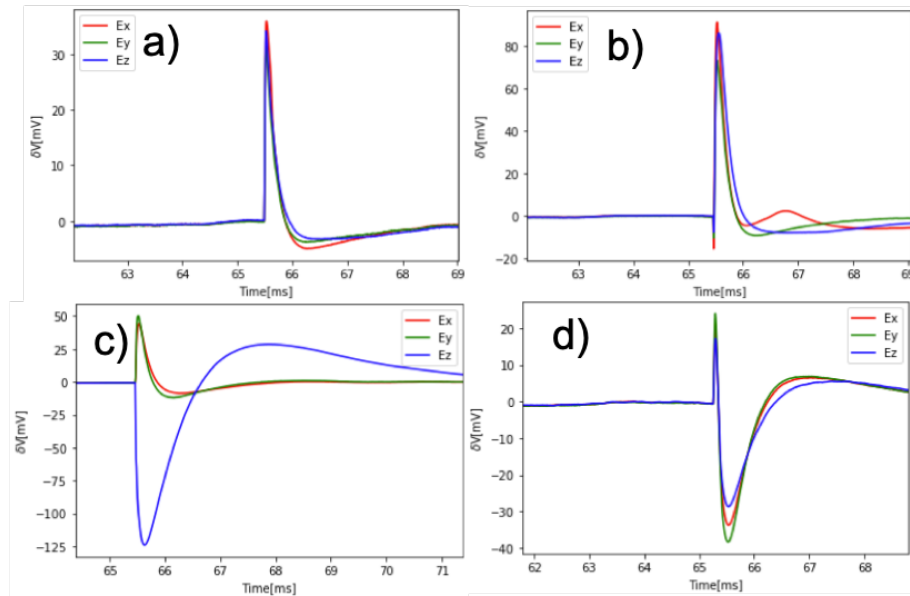
Figure 8: Main categories of dust impact signal obtained by S/WAVES/TDS: (a) All three monopoles obtained the same typical signal shape (see Figure 7), (b) **Typical** signal shape with prominent precursor ($\leqslant$ -3 mV), (c) one of the signals is inverted, and (d) all signal are inverted.

be categorized into four main categories. A typical dust waveform looks exactly like those shown in Figure 8 panels a) and b). Observations of these signals indicate that particles from outer space and interstellar space have impacted the spacecraft body (Zaslavsky et al., 2012). 94% of detected events have this shape, according to our statistics. Further analysis does not take into account events represented on panels c) and d) respectively. The signal shapes presented in these panels are quite intriguing, and it would be interesting to understand how they are formed, but for the purpose of validating our model, we will continue with the typical ones.

The resulting database contains 116544 events, 76086 on STEREO A and 40458 on STEREO B. In order to check the validity of the proposed theoretical model presented in the Article A, a statistical analysis based on the events in the database was conducted. Due to the fact that each impact creates a pulse on each of the three monopoles, there
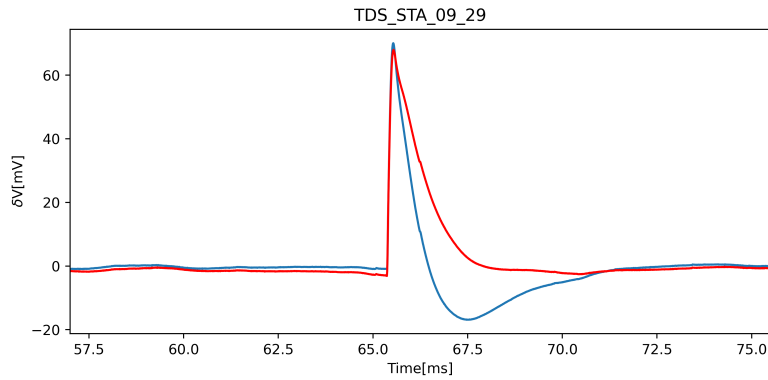
Figure 9: Effect of calibration; the blue line represents raw data and the red line is the signal after calibration.

are 349632 individual pulses.

One more step was needed before we could declare the data base complete and prepared for its final purpose, which would be to validate our model. Based on the typical dust shape shown in Figure 7, the most prominent parts are the pre-shoot, when amplitude drops before the central peak, followed by the main peak, and the overshoot (more or less prominent), when amplitude drops after the central peak. Overshoot amplitude is a subject of debate when it comes to dust signal modeling. The question arises whether it is due to the antenna's role in the charge collecting process or artificially caused by the instrument. It has been known that the electronic response to a sharp pulse can produce an artificial overshoot. In the case of the S/WAVES signal, a low-pass filter is used to prevent aliasing by matching the sampling channel. According to Bougeret et al., 2008, anti-aliasing low-pass filters are set up at the entrance of each sampling channel. Depending on the time resolution of the sample, low-pass filters can be either 108 kHz or 54 kHz (Bougeret et al., 2008). If the implementation of such filters caused this effect, we expected to resolve it by deconvolving the signal with an inverse low-pass filter. The inverse low-pass filter was, naturally, chosen in accordance with the sampling channel currently

being used (Bougeret et al., 2008). Thus, we deconvolved all the data from the data base. The FFT (a fast Fourier transform) values of the filters used to deconvolve were provided by Moustapha Dekkali and Pierre-Luc Astier for the electronic team in LESIA. Some overshoots persist even after the correction, while there are others that disappear completely. Figure 9 shows the pre – and post – deconvolution shape of a signal. As shown in the example, the overshoot disappeared while other prominent amplitudes remained almost unchanged. The example above is ideal, but not always the case. Some overshoots remain even after the correction. It is therefore likely that the remaining overshoots are not artificial, or at least not completely, but rather due to the charges of the monopoles themselves (Zaslavsky, 2015). Still, this effect is difficult to quantify reliably since the correction by the filter can be quite sensitive to the phase calibration of the filters. Nevertheless, in the present study, the variation in the antenna's potential was not taken into account.

3.3 ANALYSIS OF INDIVIDUAL IMPACTS

We developed a simple model that relies on a few parameters and is adapted to the robust fitting of the large amount of data provided by radio instruments such as S/WAVES. In order to test model reliability, we used our STEREO dataset presented above. Finally, we fitted all data from our data base with the Levenberg-Marquardt least-squares minimization method using Eq. 25. As discussed in Section 2 of Article A, we expect that the time required for the spacecraft to return to equilibrium is significantly longer than the ion characteristic time scale (i.e., $\tau_{sc} > \tau_i$). We removed any event that does not meet this condition; consequently, from the initial 349632 events, we kept about 70% of the events. There are several interesting results that we obtained
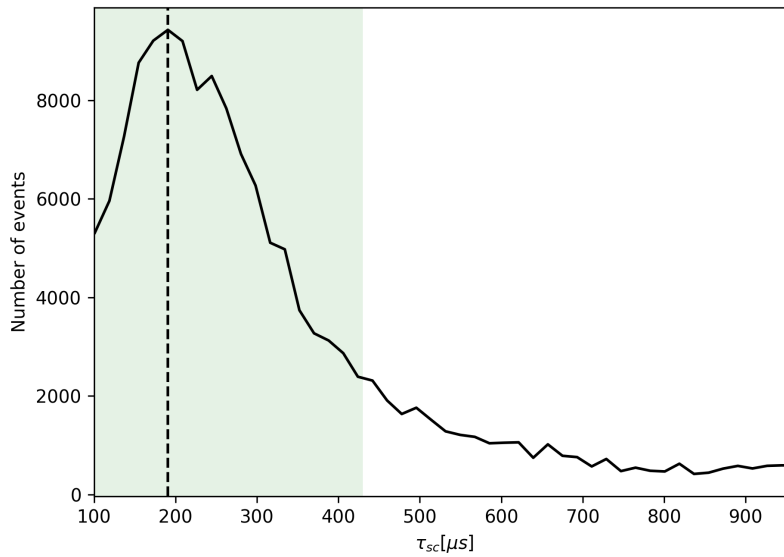
Figure 10: Histogram of the parameter τ_{sc}. The green section on the histogram indicates the extreme values of the parameter calculated from Eq. (19) (see text for details). Around 80% of the obtained values for τ_{sc} are inside the green section. The dashed vertical line represents the most probable obtained value for the parameter, $\tau_{sc} \sim 190$ µs. The median value of the distribution is 270 µs. Image Credit:Rackovic Babic et al., 2022

from this simple model, which was developed to fit typical signals rather than complicated signals. For these particular cases, numerical simulations, including a more complex spacecraft model, would be adapted (e.g. Shen et al., 2021), but these simulations are not suitable for massive fitting. In summary, through the four free fitting parameters S/WAVES signals will be statistically analyzed in the following.

3.3.1 *Linear relaxation timescale*

Figure 10 shows a histogram of the parameter τ_{sc}, which describes the discharge time scale of the spacecraft through the exchange of charges

with the solar wind and the photoelectron emission from the spacecraft. The histogram contains all the values for the τ_{sc} parameter that were obtained for each monopole.

The linear relaxation time of a spacecraft is given by Eq. (19) in Sect. 2.3. One can see that τ_{sc} depends on the geometry of the spacecraft (through its surfaces), as well as on the local plasma and photoelectron parameters. It can be evaluated as follows: STEREO satellites orbit at 1AU, where, typically, $n_e \simeq [1-10]$ cm^{-3} and $T_e \sim 10$ eV (Issautier et al., 2005). Spacecraft parameters are, as an order of magnitude, $C_{sc} \simeq 200$ pF, $S_{sc} \simeq 10$ m^2, and the photoelectron temperature is typically $T_{ph} \simeq 3$ eV. On the basis of these parameters, one can estimate the relaxation time for STEREO, $\tau_{sc} \sim 100-430$ μs. These limits are represented by the green-shaded area in Fig. 10. One can see that the distribution of the observed relaxation times peaks roughly in the middle of the green area and that most of the data ($\sim 80\%$) fall within the expected range. The most probable value and median observed values are 190 μs and 270 μs, respectively. This quite unambiguously shows that, consistent with the standard interpretation, the decay time of the pulses can be identified with the relaxation time of the spacecraft through the exchange of charges with the surrounding plasma after the spacecraft body has collected a certain amount of charge.

3.3.2 *Ion characteristic timescale*

Figure 11 presents a histogram of the ion dynamics timescale parameters, τ_i. The vast majority of the obtained values for parameter τ_i are smaller than 100 μs. As noted in Section 2.2 in Article A, this characteristic ion timescale, τ_i, is the smallest of the quantities λ_{ph}/v and the time for the cloud's ions to collect enough ambient photoelectrons to
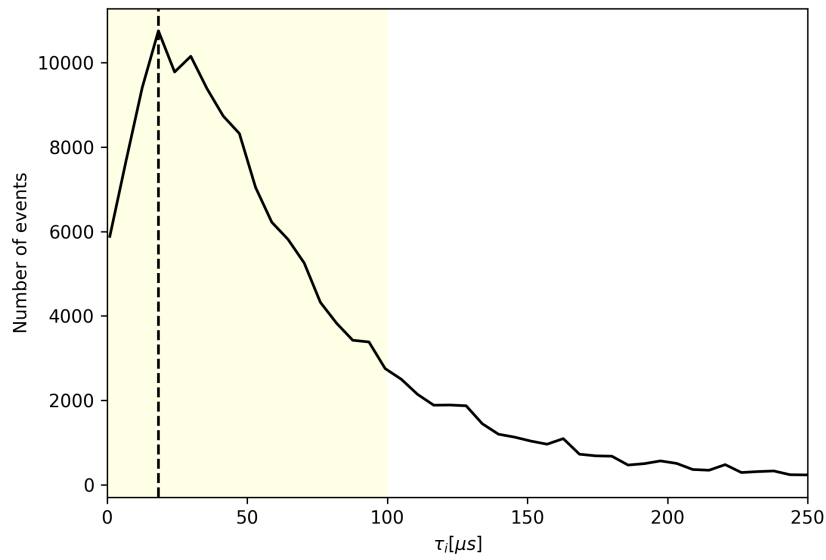
Figure 11: Histogram of the parameter τ_i. The yellow section includes all the obtained values below 100 μs (the threshold for the τ_{sc}). More than 80% of the obtained τ_i is inside the yellow section. The vertical dashed line represents the most probable obtained value for the parameter, $\tau_i \sim 18$ μs.

Image Credit:Rackovic Babic et al., 2022

be shielded by them, as estimated by Meyer-Vernet et al., 2017. Using Eqs. (11) and (4) of that paper, the latter can be simplified into

$$\tau_{ph} \simeq \left(3Q/2\pi I_{ph0}\right)^{1/3}/v^{2/3}, \tag{26}$$

where I_{ph0} is the spacecraft photoelectron current at zero potential. Assuming $I_{ph0} \simeq 20\ \mu A/m^2$ (which yields $\lambda_{ph} \simeq 0.9$ m), we deduce from the most commonly observed value $\tau_i = 18\ \mu s$ (Fig. 11) with the average charge $Q \simeq 40$ pC, the cloud's propagation and expansion speed to be $v \simeq 13$ km.s^{-1}. This result depends weakly on the badly known photoelectron current and is consistent with our estimate that $\tau_i \simeq \tau_{ph}$ since the most commonly observed value of τ_i is much smaller than λ_{ph}/V ($\lambda_{ph}/V \approx 10^2 \mu s$ according to Meyer-Vernet et al., 2017).

These values can be compared with reasonable agreement to measurements from laboratory experiments and numerical simulations. For instance, our results match those of Lee et al., 2012, who measured the ion expansion speed in laboratory experiments and found $v \geqslant 10$ km.s^{-1}. According to their results, plasma detection occurred most often from impacts on positively charged targets (such as STEREO). In contrast, detection rates for negatively charged and unbiased targets varied depending on the material. Based on multi-physics simulations of plasma production from hypervelocity impacts, Fletcher et al., 2015 reported a similar range of values.

3.3.3 *Electron collection*

The value of total charge, Q, is derived from the parameter $A \equiv \Gamma Q/C_{sc}$, which is obtained through the fitting. It should be noted that the value of A obtained on each monopole differs a bit (probably because of the influence effect on the monopoles, which is neglected in
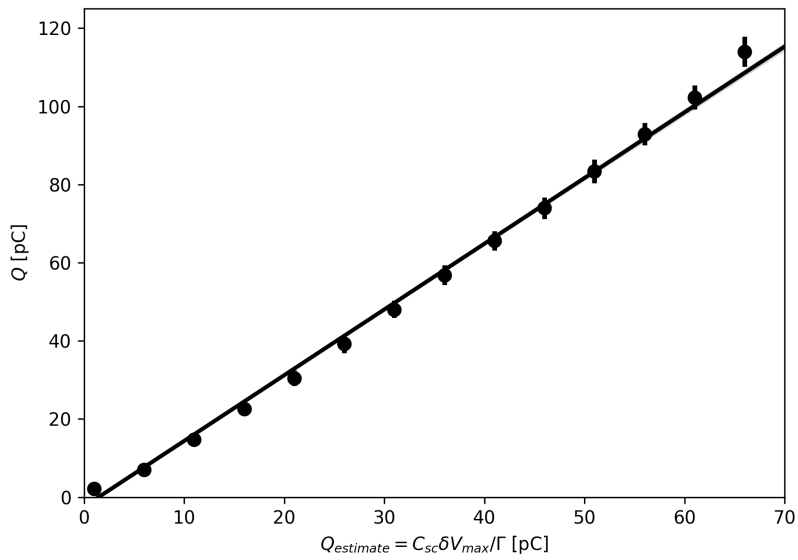
Figure 12: Total charge calculated from $Q_{estimate} = C_{sc}\delta V_{max}/\Gamma$ as a function of the total charge, Q, obtained from fitting parameter A (Eq. 17 from Article A). The binwidth is 5 pC, **and the value of the slope is** 1.63 ± 0.01. The error bars show the standard deviation of the distribution of Q in each bin.

Image Credit:Rackovic Babic et al., 2022

this thesis). However, since the total amount of charge released during an impact must be the same for all monopoles, we defined the total charge as the mean of the values obtained by fitting each monopole separately. For both STEREO spacecraft we used values for the spacecraft capacitance of $C_{sc} = 200$ pF, and for the antenna-spacecraft coupling $\Gamma \simeq 0.5$ (Bale et al., 2008). As can be seen in the Figure 12, values of Q lie within the range 8 - 120 pC.

The link between the total charge generated Q, and both the mass, m, and velocity, V, of the impacting dust particles with respect to the spacecraft was studied recently using hypervelocity impact experiments on materials relevant to STEREO satellites (Collette et al., 2014). In the case of impacts on the thermal coating that covers most of the spacecraft, the result obtained is $Q_{[C]} \simeq 1.7 \times 10^{-3} \, m_{[kg]} V^{4.7}_{[km.s^{-1}]}$. Based on this relationship, we can, by assuming a typical velocity for the impacts, translate the charge scale into a mass scale. For particles orbiting at Keplerian speeds, we can assume a typical impact velocity of 30 km.s^{-1}; the obtained mass range is then $20 - 340 \times 10^{-17}$ kg, which corresponds to the size interval $2 - 5$ μm (we assume a mass density $\rho = 2.5$ g.cm^{-3}). On the other hand, it has appeared that the fluxes observed on several spacecraft, including STEREO (Zaslavsky et al., 2012), but also Parker Solar Probe (Pusack et al., 2021) and Solar Orbiter (Zaslavsky et al., 2021), are dominated by impacts from a population of dust particles produced close to the Sun and pushed away along hyperbolic orbits by the radiation pressure, the β meteoroids. The velocity of these particles at 1 AU depends quite importantly on their origin and composition, through the value of the β parameter equal to the ratio of the radiation pressure force to the gravitational force on the dust grain. For dust of asteroidal origins, an order of magnitude of the velocity at 1 AU is 80 km.s^{-1} (Wilck and Mann, 1996). Using this value we obtain masses and sizes ranging from 0.4 to 6 $\times 10^{-17}$kg, and from 0.07 to 0.17 μm, respectively, which is compara-

ble to the masses and sizes of grains detected on the cited missions.

Figure 12 shows the total charge, Q, obtained through the fitting procedure, as a function of the charge $Q_{estimate}$ estimated with the approximation $Q_{estimate} = C_{sc} \delta V_{max} / \Gamma$ – the formula that has been used for several space missions (e.g., Zaslavsky et al., 2012) when waveform data are not available for each event. Figure 12 shows that this rough estimate is very well correlated with the total charge, Q, deduced from fitting the waveform. The slope is 1.63 ± 0.01, with 0.8 the factor of correlation. This high correlation justifies the use of the formula $A \equiv \Gamma Q / C_{sc}$ when no precise waveform data are available. However, this study shows that this formula underestimates the charge by around 30% (at 1 AU).

This underestimation has had some consequences on the estimation of particle size, in previous studies (e.g., Zaslavsky et al., 2012). Since we have seen that size is linked to Q by $s \propto Q^{1/3}$, we can estimate that the size, s, must be underestimated by around 10% – which is quite small given all the other sources of uncertainties.

3.3.4 *Electron escape*

We finally turn our attention to the electron escape current. Figure 13 shows value of the amount of charge escaping the spacecraft, ϵQ, as a function of the estimated total cloud charge, Q. The standard deviation shown as error bars gives an estimate of the width of the distribution of escaped charge in each bin. For this figure we choose only events exhibiting a voltage precursor larger than 5 mV. Our database contains about 20% of such events. Figure 14 shows the percentage of events with precursor amplitude larger than the threshold concerning
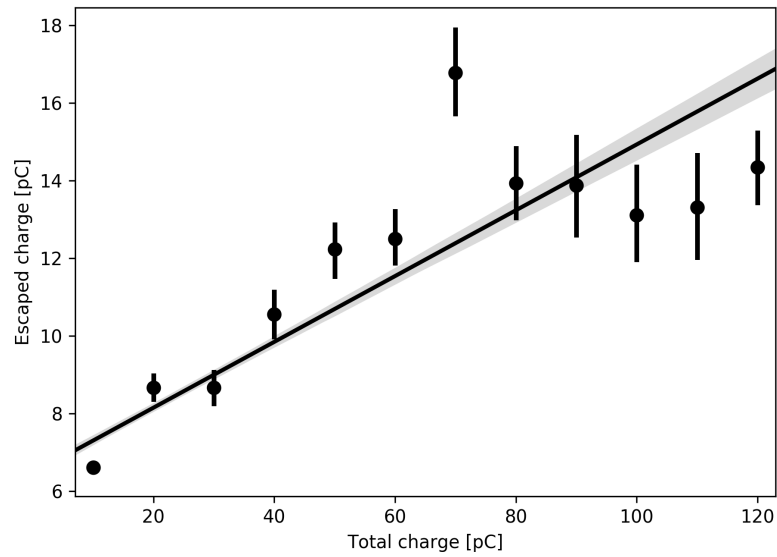
Figure 13: Escaping charge, ϵQ, as a function of the total charge released in the cloud, Q. The points show the average of the values of ϵQ per bins of values of Q. The binwidth is 10 pC. The error bars show the standard deviation of the distribution of ϵQ in each bin.
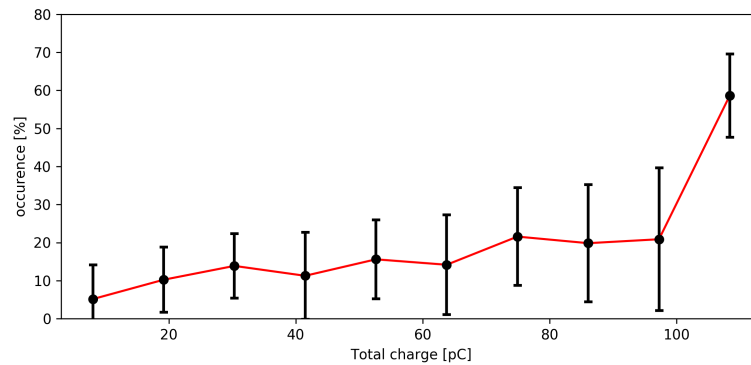Image Credit:Rackovic Babic et al., 2022

Figure 14: Histogram of the occurrence of events with precursor amplitude larger than 5mV with respect to the total charge amount. The error bars show the standard deviation of the distribution. The binwidth is 12 pC.
Image Credit:Rackovic Babic et al., 2022

the total charge amount Q.

Figure 13 shows that both are almost linearly correlated (at least up to 70pC), implying that the fraction of escaping charge, ϵ , is almost a constant. The slope of the curve, obtained by linear regression, provides a value of $\epsilon = 0.085 \pm 0.004$, where the uncertainty correspond to a 95% confidence interval on the value of the slope.

To our knowledge, this is a novel result. It shows that, on average and pretty much independently of the total amount of charge in the cloud, around 8% of this charge escapes the spacecraft. Naturally, this is a case when some charge escapes at all (Figure 14 shows that there is no precursor in the majority of the cases). This offers, for instance, a way to evaluate at least an order of magnitude of the amount of charge released during an impact that saturates the instrument if a precursor is associated with this event.

This result has a further interesting consequence. It enables us to estimate the temperature of the impact-produced electrons as follows. Roughly half of such electrons are expected to move toward the spacecraft initially and recollected, provided the spacecraft potential is positive. Among the other half (those initially moving outward), only those with an energy (in eV) exceeding the spacecraft potential, φ_{sc}, will escape. Assuming a Maxwellian distribution of temperature T (in eV), this yields

$$\epsilon = 0.5 e^{-\varphi_{sc}/T}. \tag{27}$$

With $\epsilon \simeq 0.08$ and $\varphi_{sc} = 5$ V, we obtain T $= 2.7$ eV. This result is close to the value T $= 2.5$ eV found by Fletcher et al., 2015 and to all the previous estimates, which indicated that the impact electron temperature is a few eV.

Recently, impulsive magnetic signals have been detected by search coils associated with very large amplitude (saturating) signals on the monopoles of Parker Solar Probe and Solar Orbiter (T. Dudok de Wit, M. Kretzschmar, private communication). Such signals are likely produced by the current generated by electrons escaping from the spacecraft. In this context, our measurement takes on a supplementary interest since it helps us to evaluate the escaping current from the amplitude of the pre-shoot. Indeed, one must have $I_{escape} \sim \epsilon Q / \tau_e$, where τ_e is the timescale associated with the electron dynamics. As discussed previously, this time scale has been neglected ($\tau_e \sim 0$) in the present study. This was justified by the fact that in nearly every case the rise time of the voltage precursor is not time-resolved by the TDS instrument, even when it is functioning at it highest time resolution of 4 μs. Therefore, this time resolution can be safely considered as a higher limit on τ_e, and one can evaluate

$$I_{\text{escape}} \geqslant \frac{\epsilon Q}{4 \times 10^{-6}}. \tag{28}$$

The amplitude of the magnetic pulses must be on the order of $\delta B \sim \mu_0 I_{escape} / 2\pi R$, with R the average distance between the outflowing electrons and the magnetic probe. We can then expect the amplitude of the magnetic pulse to be linearly related to the amplitude of the voltage precursor. Checking the linearity of this relation on a statistically relevant set of observed magnetic pulses would provide an interesting test for the hypothesis that the magnetic pulses are indeed produced by the current of escaping electrons.

Moreover, one can use the value of the parameter ϵ derived from our observations to estimate the size of the dust that produce magnetic pulses. For instance, an escaping current that produces a magnetic pulse of amplitude $B_{obs} \sim 0.5$ nT, taking for R a value typical of the spacecraft size, ~ 1 m, should be $I_{escape} \sim 2\pi R_{sc} B_{obs} / \mu_0 \sim 3$ mA. Now assuming that the value of ϵ stays constant ~ 0.08 even for large

values of Q, this current would correspond to a total impact charge of $Q \sim I_{escape} \tau_e / \epsilon \sim 100$ nC. For impact speeds of $50 - 100$ km.s^{-1} (relevant for Solar Orbiter and Parker Solar Probe; cf. Page et al., 2020), this would give masses of $m \sim 10^{-14}$ kg or sizes of a few microns. This is an interesting test for the hypothesis that the magnetic pulses are indeed produced by the current of escaping electrons.

<div style="text-align: right; font-size: 4em;">4</div>

VARIATION OF INTERSTELLAR DUST FLUX NEAR 1 AU

Two primary populations of dust are known to exist at 1 AU, interplanetary dust and interstellar dust. Using S/WAVES, fluxes from both populations close to 1 AU were measured (Meyer-Vernet et al., 2009; Zaslavsky et al., 2012; Belheouane et al., 2012). Similar results were obtained from the Wind/WAVES instrument (Malaspina et al., 2014). Considering those outcomes, we expected to find similar results when we analyzed the first measurements from the Solar Orbiter Radio and Plasma Wave instrument (Article B). Our analyses indicates a flux of $F_\beta \simeq 1 - 6 \times 10^{-5} m^{-2} s^{-1}$ at 1 AU for the β - meteoroid, which is similar (though slightly higher) to the one derived using S/WAVES by Zaslavsky et al., 2012; Belheouane et al., 2012. However, interestingly, one can note that if the presented data can be described well with a flux of β -meteoroids, it is found to be lacking, in comparison to the observations from STEREO (Zaslavsky et al., 2012) or Wind (Malaspina et al., 2014), an observed flux of interstellar dust (ISD). This lack of an interstellar dust component in SO/RPW data, prompted us to investigate further analysis.

Many authors (see e.g., Morfill and Grün, 1979, Grun et al., 1993, Gustafson and Lederer, 1996, Mann et al., 2010) claim that the Lorentz-force acts to repel or focus interstellar grains, depending upon the magnetic field configuration of the solar wind, and thus on the phase of the solar cycle. In order to investigate this effect, a large time-scale monitoring of ISD flux would be necessary. This kind of monitoring can be done with missions such as STEREO and Wind, which are both

capable of detecting ISD flux. For STEREO, the studies of Zaslavsky et al., 2012; Belheouane et al., 2012, covered the period 2007–2010, whereas for Wind Malaspina et al., 2014, studied the period 2006–2009. The purpose of this chapter is to examine the long–term variations of the ISD flux over two solar cycles (23 and 24).

4.1 INTERSTELLAR DUST

Dust grains originating from the local interstellar medium and which penetrate the heliosphere with a slight deviation thanks to the large speed difference between the Sun and the interstellar cloud, are called interstellar dust (Mann et al., 2010). A brief introduction of interstellar dust is mentioned in Section 2.1. We will now discuss ISD in more detail.

In the 1970's, data from dust instruments carried by some satellites suggested that ISD grains could cross the heliospheric boundary and penetrate deeply into the heliosphere (Bertaux and Blamont, 1976). In 1993, this was clearly demonstrated by the dust detector on the Ulysses spacecraft. The Ulysses dust detector, which measures mass, speed, and approach direction of the impacting grains, identified ISD grains with a radius above 0.1 μm sweeping through the heliosphere (Grun et al., 1993). Based on the Ulysses in-situ dust measurements, ISD grain motion in the solar system corresponds to the flow of neutral interstellar hydrogen and helium gas. Many studies demonstrated that gas and dust travel at speeds of 26 kms^{-1} (Gruen et al., 1994; Baguhl et al., 1995; Witte, 2004). In addition, the upstream direction of the dust flow lies at 259º ecliptic longitude and 8º latitude (Landgraf and Grün, 1998). The interstellar dust persists at high ecliptic latitudes above and below the ecliptic plane and even over the poles of the Sun, compared to the strongly depleted interplanetary dust at high latitudes (Grün

et al., 1997). Grains with diameters ranging from 0.05 μm to above 1 μm were identified by the Ulysses mission.

4.2 IN SITU DUST IMPACT DETECTION

In this part of our work, we use data from two missions orbiting at 1AU. We examine data from the WAVES electric field instrument aboard the Wind spacecraft launched in 1994 and from the WAVES instrument aboard the two twin STEREO satellites, A and B, launched in 2006. Our goal is to use the advantage of the long–term variations to monitor the ISD flux at 1 AU over different periods of the solar activity.

4.2.1 *Wind/WAVES Observations*

Wind is a spin-stabilized cylindrical satellite with a diameter of 2.4 m and a height of 1.8 m launched in 1994. The electric field detectors of the Wind/WAVES instrument are composed of three orthogonal electric field dipole antennas, two in the spin plane (spin plane differs from the ecliptic plane by $< 1^0$) of the spacecraft and one along the spin axis. The longer of the two spin plane antennas, defined as E_x, is approximately 100 meters tip-to-tip, while the shorter, defined as E_y, is $\sim$ 15 meters. Spin axis dipole, referred to as E_z, is roughly 12 meters in length. Note that the length of the E_x antenna was reduced to 27 m after the first cut on August 3, 2000 and to 25 m after the second cut on September 24, 2002. Dust impact is believed to have caused the cutting of the antennas. The complete WAVES suite of instruments includes five total receivers, in the present work we use data from Time Domain Sampler (TDS), which samples electric field data at 120 kHz, producing waveform capture of 2048 points (Bougeret et al.,

1995). High-amplitude signals from the longer antenna trigger an on board algorithm that should telemeter signals from E_x and E_y dipole to Earth.

Our study examines TDS events recorded from 1996 to 2020. As expected, the data set contains snapshots of various phenomena. Therefore, we had to find a way to identify only very sharp and impulsive events, recognized as dust events, between all those other types of occurrences. In order to clearly identify dust shapes, we set the threshold to an amplitude $|V_{max}| > 6$ mV. To determine only sharp spike events, we included only events satisfying $|V_{max}|/RMS(V) > 6$ (where RMS is the root mean square). In parallel with dust events, we also detected Langmuir waves with a corresponding amplitude. We removed Langmuir waves from the data by counting the number of intersections with one-third the height of the maximum amplitude and excluding all events with more than two intersections. An algorithm that met the above criteria was first tested using six months of observations in which several dozen dust impacts were detected. The results showed that the algorithm was effective in detecting dust-related events. It was then applied to the entire Wind TDS data set. To create a single database, we gathered all dust events measured by Wind from 1996-2020. Our derived database matches well with that of Wilson, 2020.

Figure 15 shows the modulation of the impact rates with time. The presence of the ISD manifests itself in a 1-year modulation of the flux, clearly visible from 2006 to 2012. However, we observed significant annual variations in the impact rate over different phases of the solar cycles (colours in the Figure 15). These modulations motivate our work. In the following sections, we will discuss these modulations and connect them to the relation between ISD and solar cycle.
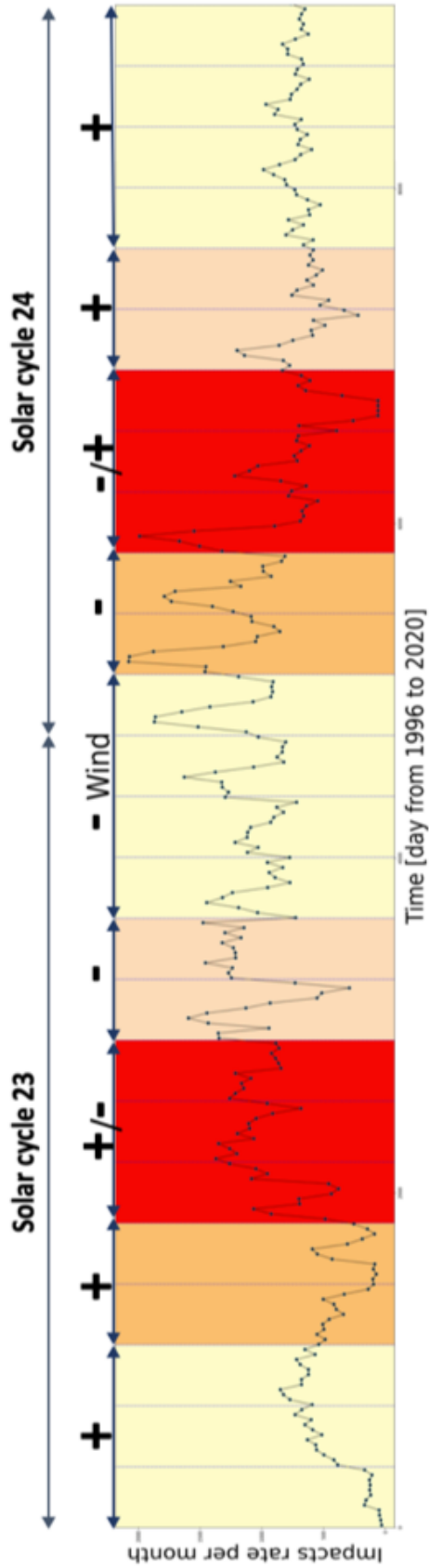
Figure 15: Impact rate as a function of time since 1996 measured by Wind. Each point corresponds to a 30-day time interval. Horizontal lines correspond to time period of each year. Solar cycle phases are indicated by colors (see Section 4.3). Positive (negative) solar polarity minima are indicated by +, − signs.

4.2.2   *STEREO/WAVES Observations*

The STEREO mission was introduced in Section 3.2. The STEREO mission consisted of two satellites, both equipped with a radio receiver. The Time Domain Sampler (TDS), a subsystem of the STEREO/WAVES instrument, generates high-cadence time series of voltage pulses for each monopole. Two TDS data sets are available: the TDSmax data gives the maximum amplitude of a peak signal detected on the antennas every minute, while the TDS Events data set provides complete voltage time series captured by the instrument with a sampling rate of a few µs (Zaslavsky et al., 2012). Since event telemetering back to Earth is dictated by the waveform amplitude, TDS events are mostly recorded during the periods of highest values of the TDSmax. As part of the current study, we use the TDSmax data set. It is sufficient to record one signal per minute, since it is very unlikely that two strong signals occur in the same minute.

In this study, we examined data for STEREO A from 2007 to 2021 and STEREO B from 2007 to 2015. We identify the positive signals between 15 mV and 170 mV. Due to the inability to verify the shape of dust spikes from TDSmax data, we set the lower limit at 15 mV, as we did in Section 3.2.1. The upper level of 170 mV is used to avoid considering signals exceeding the saturation level of the instrument. We also wanted the amplitudes to be roughly the same on all three antennas. We proceed in a similar manner as described in Section 3.2.1 for the TDS Events dataset. We define a cone that will only involve simultaneously occurring. Based on six months of observation data, we developed an algorithm that meet the above criteria, and was effective in detecting dust events. The algorithm was then applied to the entire TDSmax data set.
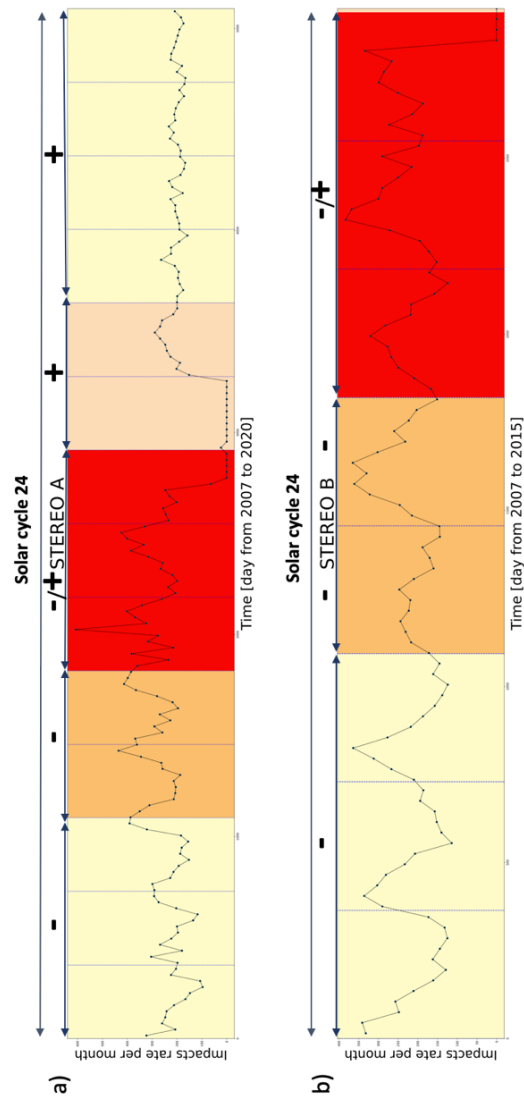
Figure 16: In panel a) one can see the dust impact rate as a function of time for STEREO A from 2007 to 2020. Panel b) depicts the dust impact rate as a function of time for STEREO B from 2007 to beginning 2015, when the connection to the spacraft was lost. Each point corresponds to a 30-day time interval. Horizontal lines correspond to time period of each year. Colors indicate phases of the solar cycle (see Section 4.3). Positive (negative) solar polarity minima are indicated by +, − signs.

Figure 16 shows the evolution of impact rates over time for both STEREO satellites. Impact rates as a function of time show a modulation on an annual basis and across the entire data set. Both satellites exhibit this modulation. Note that the data from STEREO only cover solar cycle 24.

4.3   SOLAR ACTIVITY AND INTERSTELLAR DUST

Even before 1993, when the Ulysses discovered an ISD signature, it was predicted that the trajectories of ISD grains, once they enter the solar system, are affected by gravitational forces, solar radiation pressure, and Lorentz forces (see Section 2.2). The density of ISDs in the solar system is predicted to be affected by both their location as well as their time, which corresponds to the solar cycle. Simulations of ISD grain trajectories in the solar system provided useful results. Morfill and Grün, 1979 first modeled the trajectories of ISD particles, and concluded that there are phases during the solar cycle where ISD are focused towards the solar equatorial plane and phases where the ISD are defocused from the solar equatorial plane. Since then, several models have been proposed (Landgraf, 2000; Sterken et al., 2012) that include three main forces : solar gravity, solar radiation pressure force, and the Lorentz force, which affect the relative motion of charged particles as they traverse the interplanetary magnetic field (IMF). Ions and electrons from the solar wind plasma are captured by ISD particles moving through the heliosphere. The UV radiation from the Sun also causes the grains to emit electrons due to photo-ionization. Therefore, the dust particles must be charged. Electron fluxes are much higher than ion fluxes, and the amount of electrons emitted through the photo-ionization is more than electron collection through the solar wind plasma; thus, ISD particles will get positive charge. Both the intensity of the solar UV radiation and solar wind plasma density

decrease with increasing distance from the Sun as $1/r^2$, so that this charge remains largely constant (Horanyi, 1996).

The gravitational and radiational forces are equally dependent on the heliocentric distance. The solar gravitation and solar radiation pressure forces are combined into one "effective gravitation" term (Landgraf, 1998), where β stands for the ratio of the radiation pressure force to forces gravitational force. So the β-ratio (Eq. 8) is independent of r and is a function of grain parameters (the grain chemical composition, the grain material density, the grain radius, and the grain shape). The Lorentz force results from the interaction of the charged dust particles with the interplanetary magnetic field. The IMF is modeled following the Parker model (Parker, 1958), and the polarity of the solar magnetic field is approximated by the dipole field of the Sun, which switches polarity twice every 22 years. At the heliocentric distance r and latitude θ, where B_o is the magnetic field at the source's location r_o, the IMF components are:

$$B_r = B_o \times (r_o/r)^{-2}, B_\Phi = -B_o \times \omega \cos(\Theta) \times r_o^2 r^{-1} V_w^{-1}, B_\Theta = 0, \quad (29)$$

which correspond to, the radial, azimuthal, and the normal component, respectively. Here, B_o is the magnetic field at the source's location r_o, ω represents the angular rotational speed of the Sun and is equal to 2.7×10^{-6} radian/s, and V_w the solar wind speed. Due to the time-varying polarity of the IMF, depending on the solar activity, the resulting Lorentz force is equivalent to a time-varying electric field perpendicular to the equatorial plane of the Sun. Figure 17 display the ratio of the Lorentz force to the "effective gravitation" as function of particle size a and distance to the Sun r (Landgraf, 1998). Considering the size range expected for ISD (Belheouane et al., 2012; Zaslavsky et al., 2012), of approximately 0.17 µm and 0.35 µm (based on a mass density of 2.5 gcm^{-3}), the ratio of gravity and radiation pressure force is
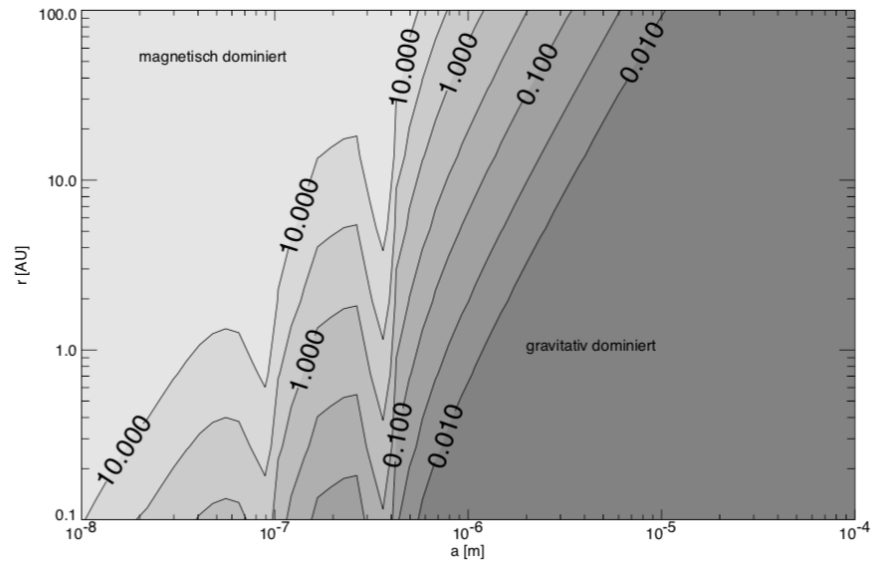
Figure 17: For several particle sizes and different distances from the Sun, the Lorentz force is compared with "effective gravitation".
Image Credit: Landgraf, 1998

~ 1 (Fig. 17). The Lorentz force takes over when gravity and radiation pressure cancel each other. Therefore, solar activity plays a significant role in the trajectory of ISD particles.

The magnetic field configuration of the Sun evolves with the 22 years cycle. Near the maximum phase of the solar activity, the magnetic field pattern becomes so complex that the field structure is rearranged with a reversed magnetic field-orientation, every 11 years. The solar cycle consists of four phases: minimum, ascending, maximum, and declining phases, respectively. Figure 18 illustrates the four phases of solar cycles 21-24. Using sunspot numbers determined by the National Geophysical Data Center (`ftp://ftp.ngdc.noaa.gov`), solar cycle phases are established (see Getachew et al., 2017 for details). Considering that Wind was launched in 1994, this study will focuses on solar cycles 23 and 24, more than 20 years. STEREO covers the solar cycle 24. Each phase is assigned a different color (Fig. 15 and Fig. 16).
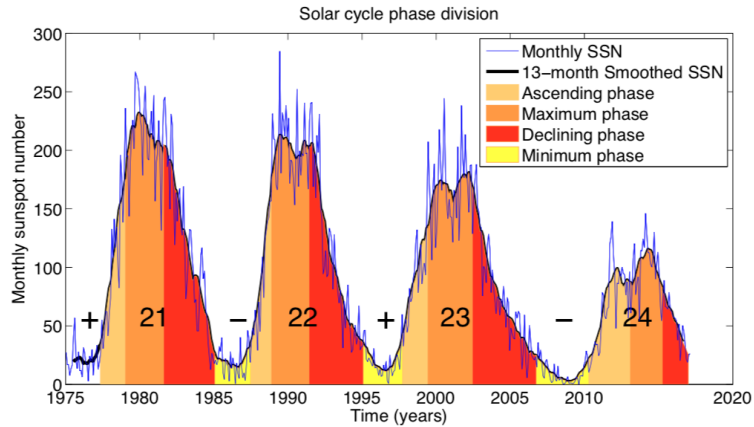
Figure 18: Phases of solar cycles $21 - 24$ denoted by color. Monthly and $13 -$ month running mean sunspot numbers are denoted by thin blue and solid black lines. The $+$ or $-$ sign indicates the positive (negative) solar polarity minima.

Image Credit: Getachew et al., 2017

The solar cycle 23 begins with a defocusing magnetic field phase. The maximum phase is between 2000-2003, and the magnetic field flipped in ~ 2003. As a result, we have a focusing magnetic structure. Solar cycle 24 begins with a focusing phase that lasts until 2014, the end of the maximum phase (2012-2014), when the magnetic field flips. After that, the Sun's magnetic field is in the defocusing phase.

We are interested in the variations of the ISD flux during each of these phases. It is possible to obtain the ISD flux features not just during focusing and defocusing magnetic field phases, but rather during different phases of the solar activity. We will discuss these results in this chapter.

4.4   VOLTAGE PULSES

Let us briefly recall the mechanism through which voltage pulses are thought to be produced. A dust grain collides with the spacecraft body and expels from it some material, a portion of which is ionized. The amount of free electric charge Q in the cloud of expelled material strongly depends on the mass and relative velocity of the impacting dust grain. The dependence has empirically been found to follow the relation Eq. 9, where m is expressed in kg and V in the kms^{-1}. Regarding the fitting parameters α, β, and γ; it is often found that $\beta \approx 1$, so a simplifying linear relation between Q and m is often assumed (Auer, 2001), the value of γ is in the range of 2–4, with $\gamma = 3.5$ commonly used, and $\alpha \approx 1$ as suggested by McBride and McDonnell, 1999.

In Chapter 3, we described and developed the model based on the assumption that electric antennas operating in monopole mode can quite reliably deduce the amount of charge (Q), released during an impact due to the different dynamics of the electrons and the heavier positive charges in the expelled cloud of ionized matter. As electrons are rapidly collected by (or repelled away from) the probe surface, depending on the spacecraft's charge, positive charges remain unscreened in the vicinity of the spacecraft. The recollection of particles of the total charge Q by the spacecraft surface of capacitance, C_{sc}, is expected to produce a pulse with a maximum amplitude of $\delta V_{sc} \sim Q/C_{sc}$. In monopole mode, the signal recorded is $V(t) = \Gamma(\varphi_{ant}(t) - \varphi_{sc}(t))$, where φ_{ant} is the monopole antenna potential, φ_{sc} spacecraft potential, and Γ the gain factor of the antennas due to their capacitive coupling with the base. Based on the assumption that φ_{ant} is roughly constant on the $\sim ms$ time scale of the impact, one can directly relate charge Q to the peak of the voltage pulse in the monopole mode by:

$$Q(m, V) \simeq \frac{C_{sc} V_{peak}}{\Gamma}. \tag{30}$$

Moreover, Figure 12 shows the total charge, Q, obtained by the fitting procedure (presented in the Chapter 3), as a function of the charge $Q_{estimate}$ estimated with the approximation from the Eq. 30. According to the figure, this rough estimate correlates well with the total charge, Q, derived from fitting the waveform, with a correlation factor of 0.8.

For STEREO, we use the capacitance of a perfectly conducting rectangular cuboid of dimensions 2.3m × 1.2m × 1.3m, which is about 200pF (Zaslavsky et al., 2012), with factor $\Gamma \sim 0.5$ as indicated by Bale et al., 2008. Note that we only considered charges between 15mV and 170mV detected simultaneously by all three monopoles. It is apparent from Eq. 10 that the mass scanned depends on the velocity of the dust population considered, which we cannot determine independently. Such events, detected simultaneously by all three monopoles, are mainly caused by two groups of particles: the β–meteoroids, with radial velocities of the order of $50 - 80$ kms^{-1}, and interstellar dust particles, with velocities of the order of ~ 26 kms^{-1}. For β–particles signal correspond to grains in the mass range $8 \times 10^{-18} - 3 \times 10^{-17}$kg, or equivalently to radius sizes 90nm × 0.14μm. For interstellar dust particles, the mass range is $5 \times 10^{-17} - 5 \times 10^{-16}$kg, or for radius $0.17 - 0.36$μm. It should be noted that the mass of the detected ISD grains correlates with the ecliptic longitude of the spacecraft, so that smaller grains are detected when the orbital velocity of the satellite is antiparallel to the ISD velocity, i.e., larger grains are detected when the orbital velocities are parallel. A fraction of the simultaneously produced pulses is generated by particles orbiting at 1AU at Keplerian velocities (Zaslavsky et al., 2012). The average velocity of such particles is ~ 20 kms^{-1}, meaning that they have a mass of $5 \times 10^{-16} - 5 \times 10^{-15}$kg. As the cumulative mass flux decreases with mass, this component should be smaller than the one associated to β-meteoroids and can be easily separated from the interstellar one using longitudi-

nal modulation (see Section 4.5).

As can be seen, when operating in monopole mode, it is quite simple to link the charge, Q, produced by impact ionization to the measured peak of the voltage pulse. The main change induced by the impact occurs in the spacecraft's surface potential, while antenna potential stays roughly constant. Dipole measurements, such as those from Wind, which measure the variation of an antenna's potential relative to another antenna, are therefore quite insensitive to this process. Thus, in order for a signal to be observed in dipole mode, it must produce a pulse of substantially larger amplitude on a particular antenna than on the other arm of the dipole. In the case of Wind, Meyer-Vernet et al., 2014 suggested that pulses are produced by the electrostatic voltage induced on the antennas by the impact produced positive ions after the spacecraft has recollected the electrons. This mechanism agrees with the voltage sign observed on Wind for interstellar grain impacts since the antenna arm closer to the impact site will then measure a larger positive voltage. Since the amplitude of the voltage pulse is dependent not only on Q but also on the position of the impact relative to the antennas, dipole measurements are more challenging to interpret. For instance, an impact occurring at equidistance from two arms of the dipole would produce a very small signal in dipole mode, even for an important release of charge. Alternatively, an impact cloud expanding near a particular dipole arm could produce a quite strong signal despite a much lower charge release. An order of magnitude of such a signal is (Meyer-Vernet et al., 2014) $V_{peak} \sim \Gamma Q / (4 \pi \epsilon_0 L_{ant})$, assuming only one arm of the dipole sees the whole unscreened charge Q, on an antenna arm of physical length L_{ant} in m. Therefore, in dipole mode, the charge in the cloud can be linked to the peak voltage as follows:

$$Q(m, V) \simeq \frac{4 \pi \epsilon_0 L_{ant} V_{peak-dipole}}{\Gamma}, \tag{31}$$

where $L_{ant} \simeq 7.5m$ and $\Gamma \simeq 0.4$ for the Wind E_y dipole (Meyer-Vernet et al., 2014). It is expected that a reduction in the length of E_x antenna significantly affects the produced signal, since antenna length plays a significant role in dipole mode.

4.5 FLUX OF INTERSTELLAR DUST, ANALYSIS OF WIND AND STEREO DATA

The number of dust hits per second on the spacecraft is roughly

$$N_s \simeq S \times F(m_{min}, m_{max}), \tag{32}$$

where S is the cross-sectional surface of the spacecraft, and $F(m_{min}, m_{max})$ the flux density of particles having a mass between m_{min} and m_{max}. In this case, mass intervals are defined by the voltage intervals (as mentioned in Section 4.4), and the flux in the $m^{-2}s^{-1}$ is

$$F(m_{min}, m_{max}) \simeq N_{day}/(24 \times 3600 \times S), \tag{33}$$

where N_{day} is the number of dust detections per day. Figures 15 and 16 show the dust impact rate as a function of time for Wind and STEREO A and B, respectively. These figures show that, in addition to the more-or-less constant flux, there is an additional flux component varying throughout the year. As we are aware that those modulations are associated with ISDs, let's learn more about them.

Due to the fact that the measured flux depends on impact velocity, it can be expressed as $F = N \times V_{impact}$ where N is the dust number density and V_{impact} the relative velocity of the spacecraft with respect to the dust. The impact speed is $V_{impact} = V_{ISD} - V_{sc}$, where V_{sc} is the speed of the probe ($\sim$ 30kms^{-1}), and V_{ISD} is the speed of the grain. For impacts caused by β-meteorites (with quasi-radial velocity),

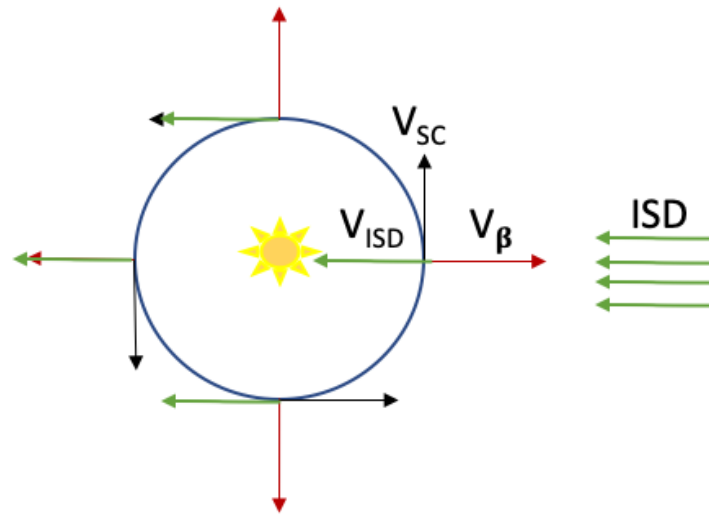Figure 19: An illustration of the velocities of the interstellar dust V_{ISD}, β -
meteorites V_β, and spacecraft V_{sc}. The spacecraft is assumed to
be in a perfectly circular orbit. The observed ISD flux is expected
to be greatest when the probe's orbital velocity about the Sun is an-
tiparallel to the ISD velocity, creating the highest relative velocity
between the probe and the ISD flow. Conversely, when the probe
orbital velocity is parallel to the ISD velocity, the relative velocity
is lowest, and the flux of measurable ISD should decrease.

the impact velocity is approximately $\sqrt{V_{sc}^2 + V_\beta^2}$ regardless of the po-
sitions of the probes in their orbits. Additionally, for interstellar dust,
this expression is only valid at the positions of the probes where their
longitudes are equal to the arrival longitude of the dust grain (see Fig-
ure 19).

Based on the composition of velocities (Figure 19), the total flux of
dust grains measured by spacecraft at a given longitude, represents
the sum of the flux of β-meteorites and that of interstellar dust (Za-
slavsky et al., 2012). Hence, expected impact rate is equal to:

$$R = F_\beta S \sqrt{1 + (\frac{V_{SC}}{V_\beta})^2 +}$$
$$F_{ISD} S \sqrt{1 + (\frac{V_{SC}}{V_{ISD}})^2 - 2\frac{V_{SC}}{V_{ISD}} \sin{(\theta - \theta_{ISD})}}, \quad (34)$$

where θ_{ISD} is the ISD upstream direction. In this expression, the first term comes from the composition of the β - meteoroid radial velocity and the spacecraft velocity. The second term refers to the composition of the ISD velocity and the spacecraft velocity, taking into consideration both the ecliptic longitude of the spacecraft, θ, and the ISD arrival ecliptic longitude, θ_{ISD}. This equation was used to fit flux from both STEREO probes and produced satisfactory results (see Belheouane et al., 2012; Zaslavsky et al., 2012).

Since ISD flows from the same direction as interstellar neutral gas, one can determine the longitude and latitude of the ISD flow. Ecliptic longitude is $\theta_{ISD} \simeq 259 \pm 20°$, and latitude is $\varphi_{ISD} \simeq 8 \pm 10°$, with a velocity of $\sim 26 km s^{-1}$ (Grun et al., 1993). With latitude φ_{ISD} taken into account, Eq.34 becomes:

$$R = F_\beta S \sqrt{1 + (\frac{V_{SC}}{V_\beta})^2 +}$$
$$F_{ISD} S \sqrt{1 + (\frac{V_{SC}}{V_{ISD}})^2 - 2\frac{V_{SC}}{V_{ISD}} \cos{\varphi_{ISD}} \sin{(\theta - \theta_{ISD})}}. \quad (35)$$

Fitting the fluxes from both missions (Wind and STEREO) was performed using equation 35. We obtained the best fit by using the following values for the fixed parameters: $V_\beta = 80 km s^{-1}$ for the radial velocity of the β - meteoroids population, $V_{ISD} = 30 km s^{-1}$ for the interstellar dust velocity, and $\varphi_{ISD} = 8°$ for the ecliptic latitude of the ISD flow. The cross-sectional surface, S, for the Wind probe is 4.3 m^2, and for STEREO satellites is $2\sqrt{2}$ m^2.
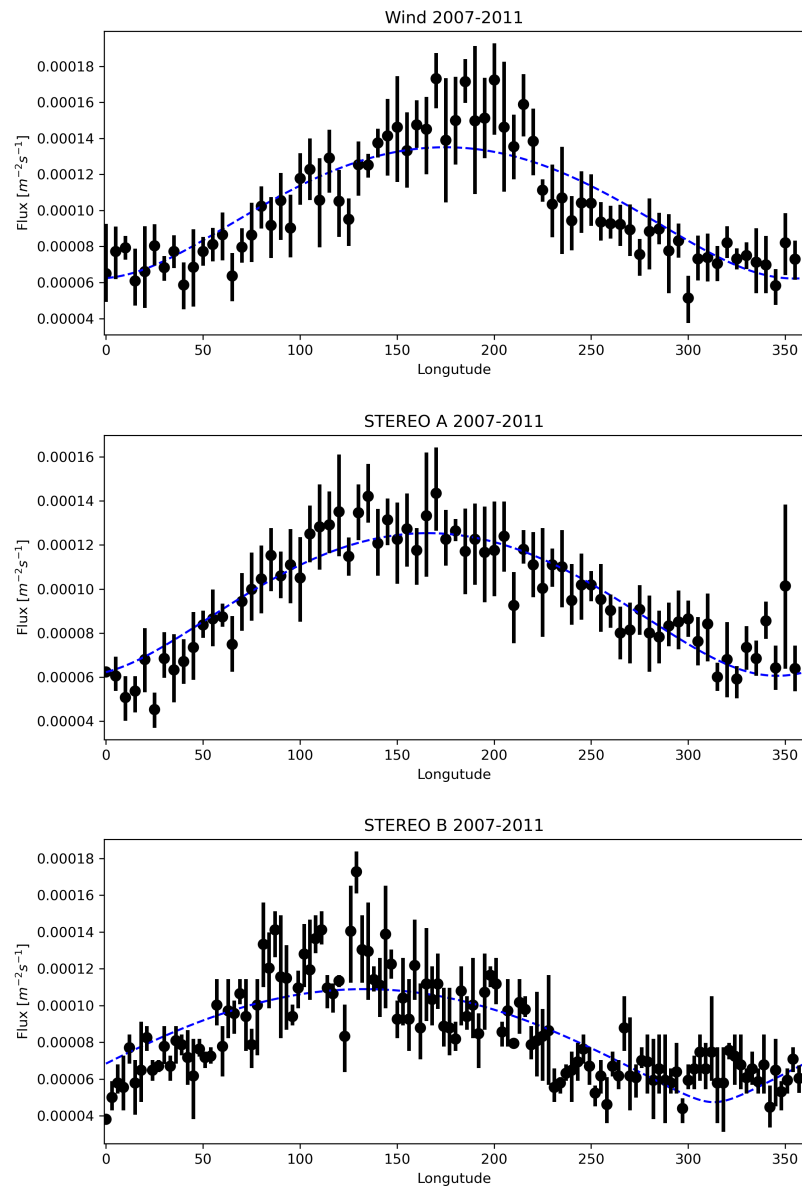
Figure 20: The averaged flux measured over five years (2007-2011) on the WIND, STEREO A, and STEREO B (top to bottom) and the corresponding error bars as a function of the probes' ecliptic longitude. The averaging is performed on 5 degrees bins and the error bars show the standard deviation of the distribution. The blue curve is the result of the fitting model as described in the text.

Satellite	F_β	F_{ISD}	θ_{ISD}
Wind	3.87×10^{-5} $m^{-2}s^{-1}$	4.07×10^{-5} $m^{-2}s^{-1}$	254 deg
STEREO A	4.23×10^{-5} $m^{-2}s^{-1}$	6.48×10^{-5} $m^{-2}s^{-1}$	255 deg
STEREO B	2.42×10^{-5} $m^{-2}s^{-1}$	3.42×10^{-5} $m^{-2}s^{-1}$	259 deg

Table 2: Obtained values for β - meteoroids flux, ISD flux, and ecliptic longitude of ISD flow, for period 2007-2011 on all three probes.

Since we assume that the phase of the solar magnetic field is related to the ISD flux, we used dust data from all three spacecraft from 2007-2011 in the first step. During this period, the solar cycle reaches its minimum, and the solar dipole is directed southward. We fitted the flux averaged over five years using equation 35 and the above mentioned parameters. Figure 20 shows the average measured flux during this period (each panel corresponds to one spacecraft), and the blue line corresponds to the fitting model results. Table 2 summarizes the values obtained for each spacecraft.

These measurements are in a good agreement with results obtained by Zaslavsky et al., 2012 and Belheouane et al., 2012 for both STEREO satellites. Within a similar timeframe, 2007-2010, Zaslavsky et al., 2012 obtained $F_\beta \simeq 6 \times 10^{-5}$ $m^{-2}s^{-1}$, $F_{ISD} \simeq 8 \times 10^{-5}$ $m^{-2}s^{-1}$, $\theta_{ISD} \simeq$ 258 deg; and in the same period Belheouane et al., 2012 estimated $F_\beta \simeq 4.3 \times 10^{-5}$ $m^{-2}s^{-1}$, $F_{ISD} \simeq 6.5 \times 10^{-5}$ $m^{-2}s^{-1}$, $\theta_{ISD} \simeq 260$ deg. In terms of Wind, Malaspina et al., 2014 estimated flux of $(2.7 \pm 1.4) \times 10^{-5}$ $m^{-2}s^{-1}$ between 2006 and 2009. Furthermore, these measurements are in good agreement with those obtained by the Ulysses spacecraft (Krüger et al., 2007) and by the Cassini spacecraft between 0.7 and 1.2 AU (Altobelli et al., 2003). Due to the fact that the fitting model contains a number of approximations, the estimated values for
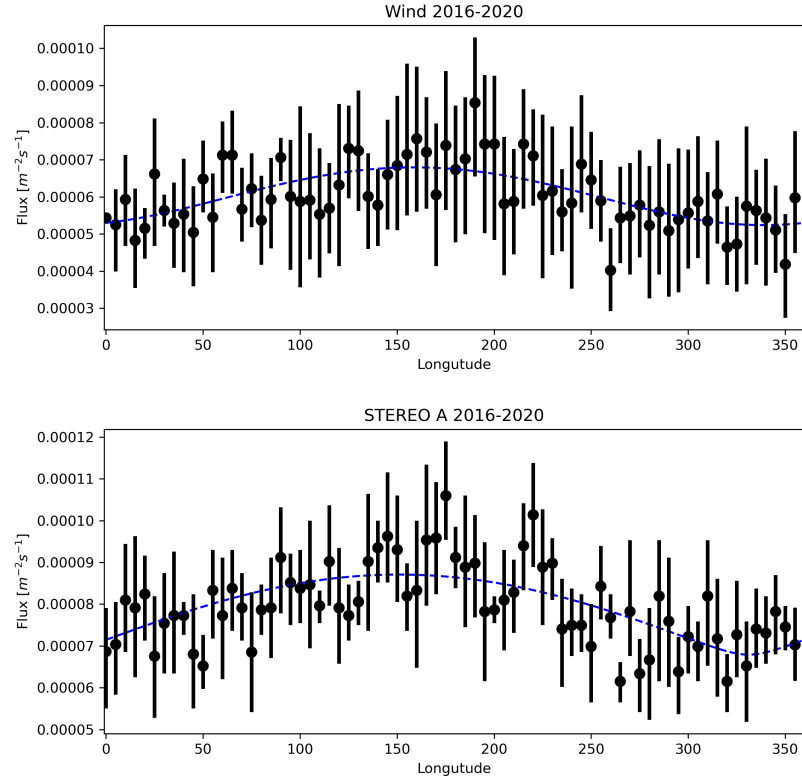
Figure 21: The averaged flux measured over five years (2016-2020) on the WIND (top) and STEREO A (bottom), respectively and the corresponding error bars as a function of the probes' ecliptic longitude. The averaging is performed on 5 degrees bins and the error bars show the standard deviation of the distribution. The blue curve is the result of the fitting model as described in the text.

θ_{ISD} should be interpreted with caution. Even though the results obtained are consistent with those previously published using a similar technique (Zaslavsky et al., 2012; Belheouane et al., 2012), the geometry of the spacecraft and the dynamics of the particles should be taken into account to obtain more accurate results.

During the period 2016 - 2020 which also overlaps solar minimum, the solar dipole, in contrast, points northward. Unfortunately, for this period, only two probes have collected data (since 2015, no data have

Satellite	F_β	F_{ISD}	θ_{ISD}
Wind	4.18×10^{-5} $m^{-2}s^{-1}$	8×10^{-6} $m^{-2}s^{-1}$	263 deg
STEREO A	3.38×10^{-5} $m^{-2}s^{-1}$	9.7×10^{-6} $m^{-2}s^{-1}$	244 deg

Table 3: Obtained values for β - meteoroids flux, ISD flux, and ecliptic longitude of ISD flow, for period 2016-2020 on all three probes.

been available from STEREO B). Figure 21 shows the average measured flux during this period; The upper panel represents the Wind satellite, and the lower panel represents STEREO B. The blue line corresponds to the fitting model results. Table 3 summarizes the values obtained with the fitting model for both spacecraft during this period. Note that period from 1996 to 2000 had similar solar conditions (solar minimum and defocusing phase), for which Wind data are also available. We found the following results using the same method: $F_\beta \simeq 5.23 \times 10^{-5} \ m^{-2}s^{-1}$, $F_{ISD} \simeq 1.9 \times 10^{-5} \ m^{-2}s^{-1}$.

Comparison of the obtained values for F_{ISD} from Table 2 and Table 3 and F_{ISD} obtained from Wind data for the period 1996-2000 shows a clear difference. ISD flux component is obviously higher during the solar minimum when the solar dipole points southward. The same fitting procedure can be used for the estimation of ISD flux for each year. The Figure 22 shows the annual values of the obtained F_{ISD}, with each panel representing a different spacecraft. With the values presented this way, we can visualize the flux variations in each phase of the solar cycle. The expectance of the highest flux value occur during the solar minimum in the period 2007-2011, when solar magnetic field is in the focusing phase, has been met. This is evident from the Wind and STEREO A panels. Unfortunately, all the STEREO B available data covers not much more than the above mentioned period, so
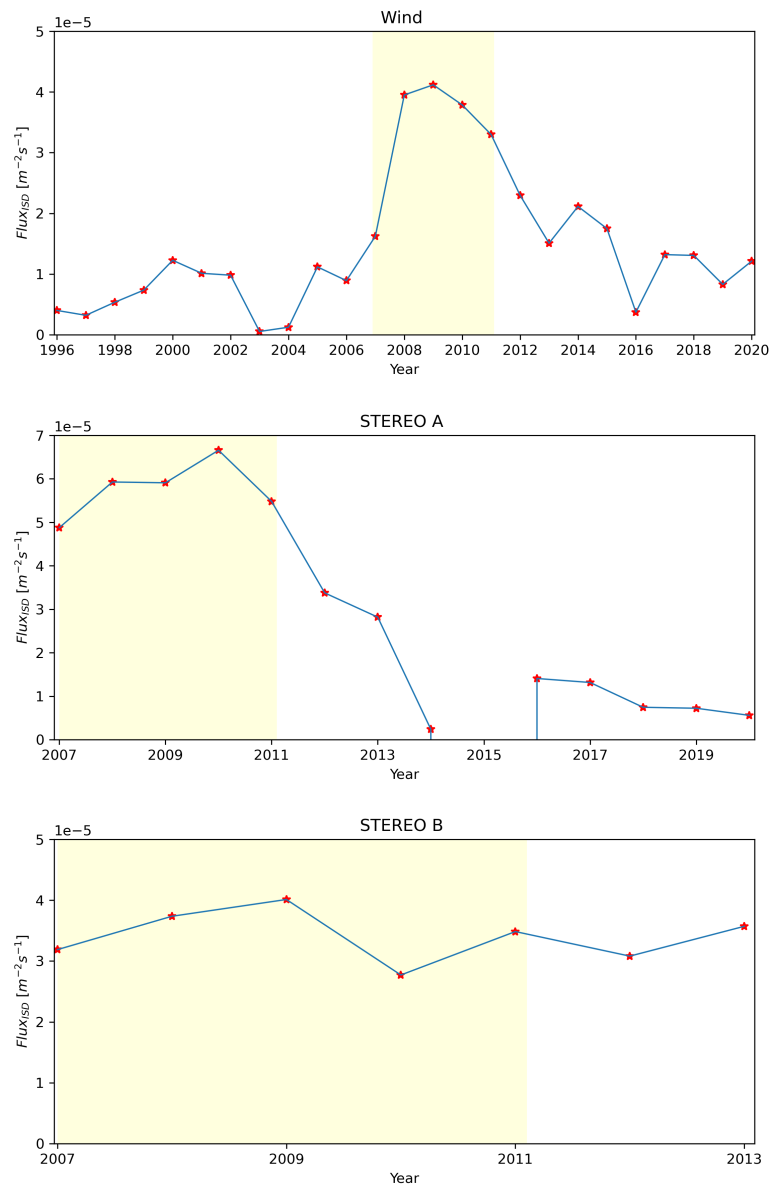
Figure 22: The annual values of the obtained F_{ISD} for the WIND, STEREO A, and STEREO B (top to bottom). Red stars represent ISD flux values for corresponding years. STEREO A data for 2015 are not available. The yellow areas correspond to the time period when the solar cycle reaches its minimum, and the solar dipole is directed southward.

we cannot draw any further conclusions for this probe. For the year 2015, there is no STEREO A data available, so the flux value was not displayed.

Even though equation 35 neglect some effects, such as the velocity dispersion of the dust particles, as well as the fact that the mass range scanned varies with the relative velocity of the impact, and thus, for the ISD, with the spacecraft longitude, the obtained values reveal interesting conclusions. This study allowed for the first time a continuous measurement of the ISD flux over two solar cycles. Although correlation does not always imply causation, the drop in the ISD flux makes sense when compared to solar magnetic conditions. Focusing conditions, which allow dust grains to gain traction in their upward path towards the Sun, thus remaining relatively close to both the ecliptic and solar-equatorial planes. Indeed, between 2007 – 2011 at solar minimum with a solar dipole pointing southward, all three spacecraft recorded a significant amount of ISD flux. In contrast, defocusing conditions, tend to drive interstellar grains away from the ecliptic and solar-equatorial planes, resulting in less accessibility and likely lower fluxes at 1 AU. Both observed defocusing solar minima phases, in 1996–2000 and in 2016–2020, show a low ISD flux. We cannot rule out the possibility that ISD disappears completely, but certainly the smallest ISD grains will not be able to reach 1 AU during defocusing phase. This will need further investigation using a dynamics ISD model.

Considering that the previous magnetic flip from defocusing to focusing phase occurred in 2003, and that a significant increase in ISD component was seen in 2006, a similar situation could be predicted in the current solar cycle 25. Based on the assumption that the magnetic flip will occur in 2025, it is natural to expect a change in ISD flux not before 2028.

CONCLUSIONS

Using a radio instrument to detect dust grains provide a much larger detection area than conventional dust detectors. In order to relate the observed electrical signals to the properties of the dust, it is essential to develop models of how signals are generated in this method of dust detection. Developing such a model is an important part of the presented work. The work presented here supports previously published studies on dust particles observed at 1 AU.

In the first part of this thesis we present a theoretical model for the generation of voltage pulses by the collision of dust grains onto a spacecraft. Continuing previous studies (Zaslavsky, 2015; Meyer-Vernet et al., 2017), our work provides for the first time an analytical formula describing the voltage pulse as a consequence of the combined effects of charge collection by the spacecraft and electrostatic influence from charges in its vicinity.

We validate our model using data from the S/WAVES instrument at 1 AU. In order to validate the developed model, the first step was to design a proper database.An auto-detection algorithm was created for data from STEREO/ WAVES TDS instrument. The algorithm aims to detect the dust signal, among other signal shapes, in the vast data sets. Machine learning can be useful for such tasks. On the example of Solar Orbiter - Radio and Plasma Waves Instrument, Kvammen et al., 2022 presented an novel approach to this problem (see Article C). This technique can also be applied to data from other missions, as well as STEREO, with high detection accuracy likely to be achieved. Perhaps

it would be interesting to apply the machine learning classification to the same dataset, and compare the obtained database with the one used in model testing.

We used data from the S/WAVES TDS instrument to determine the four independent free parameters appearing in our model (total ion charge, Q, fraction of escaping charge, ϵ, rise timescale, τ_i, and relaxation timescale, τ_{sc}) by fitting our model to the waveform data using a least-square Levenberg-Marquardt technique. As a result, we were able to obtain the first in situ measurements of parameters such as the electron escape current and a estimation of the temperature of the electrons in the impact cloud (T ~ 2.5 eV).

Further, our study is consistent with the idea that the pulse's rise time largely exceeds the spacecraft's short timescale of electron recollection. When the electrons are recollected, the positive ions are still very close to the spacecraft since $m_i \gg m_e$. Hence, they produce a voltage of the opposite sign to that produced by the electron recollection. Therefore, the rise time of the signal is determined by the voltage induced on the spacecraft by the cloud's positive ions (Meyer-Vernet et al., 2017). Moreover, obtained values for the rise time give us insight into the propagation speed of the ion cloud. This is an exciting result given that, as far as we know, this is the first time that information about the velocity of ion clouds was calculated from data. We compared the results with the values obtained in numerical simulations and laboratory experiments. Calculations based on numerical simulations (Fletcher et al., 2015) and laboratory experiments (Lee et al., 2012) match our results.

We also found that the amount of charge escaping the spacecraft is almost linearly related to the estimated total cloud charge. Recently detected impulsive magnetic signals associated with saturating signals on the monopoles of Parker Solar Probe and Solar Orbiter are likely

related to the electrons escaping from the spacecraft. In this context, our model takes on a supplementary interest since it helps us evaluate the escaping current from the amplitude of the precursor. The effect of the potential induced by the cloud's ions on the antennas, expected to be small on STEREO, could explain the minor differences between the voltages measured on the three monopole antennas. However, on other missions where the antennas are located on different sides of the spacecraft, for example WIND, Parker Solar Probe, and Solar Orbiter, this effect should produce very different voltages on different antennas and therefore enable dust detection in dipole mode, as first suggested by Meyer-Vernet et al., 2014.

The second part of the thesis work focuses on interstellar dust. Specifically, this study aims to examine the long-term variation in ISD flux over two solar cycles (23 and 24). Lorentz force has long been thought to repel or focus interstellar grains based on the magnetic field configuration of the solar wind, and therefore on the phase of the solar cycle (Morfill and Grün, 1979, Grun et al., 1993). In order to analyze something for which we need long-term observation, we should have chosen a long-term mission. Since both Wind and STEREO are long-term missions and have been proven reliable for dust detection, we chose to use data from both missions to examine ISD flow. First continuous measurement of ISD flux over two solar cycles was achieved in this study. Even though we used a simple equation for fitting obtained flux, which neglects some effects, such as velocity dispersion of dust particles, as well as the fact that the mass range scanned varies with the relative velocity of the impact, the obtained values provide interesting insight into the ISD. Between 2007 − 2011 at solar minimum with a solar dipole pointing southward, all three spacecraft recorded a significant amount of ISD flux. On the other hand, both observed defocusing solar minimum phases, in 1996–2000 and in 2016–2020, ISD flux is significantly reduced. In our opinion, ISD dust impact will not

completely cease during deffocusing phase, but certainly the smallest ISD grains will not be able to reach 1 AU during this phase. A dynamic ISD model will be needed to investigate this further.

Considering that the previous magnetic flip from defocusing to focusing phase occurred in 2003, and that a significant increase in ISD component was seen in 2006, a similar situation could be predicted in the current solar cycle 25. Based on the assumption that the magnetic flip will occur near 2025, it is natural to expect a change of the ISD flux around 2028.

Part I

PUBLICATIONS

AN ANALYTICAL MODEL FOR DUST IMPACT VOLTAGE SIGNALS AND ITS APPLICATION TO STEREO/WAVES DATA

Astronomy
&
Astrophysics

An analytical model for dust impact voltage signals and its application to STEREO/WAVES data

K. Rackovic Babic[1,2] , A. Zaslavsky[1] , K. Issautier[1] , N. Meyer-Vernet[1], and D. Onic[2]

[1] LESIA, Observatoire de Paris, Université PSL, CNRS, Sorbonne Université, Université de Paris, Paris, France
e-mail: kristina.rackovic@obspm.fr
[2] Department of Astronomy, Faculty of Mathematics, University of Belgrade, Belgrade, Serbia

ABSTRACT

Context. Dust impacts have been observed using radio and wave instruments onboard spacecraft since the 1980s. Voltage waveforms show typical impulsive signals generated by dust grains.
Aims. We aim at developing models of how signals are generated to be able to link observed electric signals to the physical properties of the impacting dust. To validate the model, we use the Time Domain Sampler (TDS) subsystem of the STEREO/WAVES instrument which generates high-cadence time series of voltage pulses for each monopole.
Methods. We propose a new model that takes impact-ionization-charge collection and electrostatic-influence effects into account. It is an analytical expression for the pulse and allows us to measure the of amount of the total ion charge, Q, the fraction of escaping charge, ϵ, the rise timescale, τ_i, and the relaxation timescale, τ_{sc}. The model is simple and convenient for massive data fitting. To check our model's accuracy, we collected all the dust events detected by STEREO/WAVES/TDS simultaneously on all three monopoles at 1AU since the beginning of the STEREO mission in 2007.
Results. Our study confirms that the rise time largely exceeds the spacecraft's short timescale of electron collection. Our estimated rise time value allows us to determine the propagation speed of the ion cloud, which is the first time that this information has been derived from space data. Our model also makes it possible to determine properties associated with the electron dynamics, in particular the order of magnitude of the electron escape current. The obtained value gives us an estimate of the cloud's electron temperature – a result that, as far as we know, has never been obtained before except in laboratory experiments. Furthermore, a strong correlation between the total cloud charge and the escaping charge allows us to estimate the escaping current from the amplitude of the precursor, a result that could be interesting for the study of the pulses recently observed in the magnetic waveforms of Solar Orbiter or Parker Solar Probe, for which the electric waveform is saturated.

Key words. solar wind – Sun: heliosphere – methods: analytical – methods: data analysis – meteorites, meteors, meteoroids – interplanetary medium

1. Introduction

Dust grains are a common constituent of the Solar System. The origin of dust has been attributed to comets, asteroids, the interstellar medium, etc. (Mann et al. 2014; Grün & Dikarev 2009). Through in situ detection we can gain insight into individual properties such as the mass, charge, and composition of the dust particles. In addition to dust detectors on some spacecraft (Srama et al. 2004; Gruen et al. 1992), plasma wave and radio wave instruments are often used to detect dust. Hence the importance of developing models of how signals are generated to be able to link the electric signals observed to the physical properties of the dust impact.

With the Voyager mission, it became apparent that dust impacts on spacecraft produce measurable electrical signals, which may be used to detect dust in situ. Voltage pulses of the same type were detected in multiple missions and identified as dust impacts (Gurnett et al. 1983, 1997; Meyer-Vernet et al. 1986; Oberc et al. 1990; Tsurutani et al. 2003; Kurth et al. 2006; Vaverka et al. 2019; Ye et al. 2019). From the 1980s until the present day, several physical mechanisms have been proposed to explain how dust particles produce electrical signals. The first proposed models (Aubier et al. 1983; Oberc 1996) relate to charging mechanisms that can lead to voltage signals, charging

an antenna or charging a spacecraft. The models illustrate the importance of the system geometry, the impact cloud geometry, and whether the measurements are in monopole or dipole mode. According to these and subsequent proposed models, voltage pulses can be explained by free electric charges resulting from impact ionization after hypervelocity dust particles hit a spacecraft. Impact ionization produces a plasma cloud made of dust and spacecraft cover material ejected from the impacted surface. In the solar wind, spacecraft are usually positively charged due to the strong photoelectron current they emit because of their exposition to the Sun's UV radiation. Thus, it is likely that the spacecraft attracts electrons from the impact-produced cloud while repelling positive ions. The recollection of particles of total charge Q by the spacecraft surface of capacitance, C_{sc}, is expected to produce a pulse with a maximum amplitude of $\delta V_{sc} \sim Q/C_{sc}$.

Recent advances in the performance of radio detectors have allowed us to gain an improved understanding of the mechanisms that generate voltage pulses. Missions such as Wind (Bougeret et al. 1995), Cassini (Gurnett et al. 2004), or STEREO (Bougeret et al. 2008) have provided us with access to a large number of electric waveforms that are characteristic for dust impacts. As a result of the large amount of available data, more sophisticated physical mechanisms have been

suggested. Zaslavsky (2015) proposed a description of the response of a spacecraft to the collection of electric charges generated after the hypervelocity impact of a dust grain. He attributed voltage signals to electron collection, but was unable to explain the observed rise time of signals. Meyer-Vernet et al. (2017) demonstrated that the influence of positive ions in the vicinity of the spacecraft needs to be considered and that the positive charge timescale controls the pulse rise time. An analysis of spacecraft charging processes in various plasma environments and an application to dust impacts on MMS is presented by Lhotka et al. (2020). A few models have been developed on the basis of the antenna signal generation processes in the laboratory. Collette et al. (2015) identified three mechanisms for signal generation: induced charging, antenna charging, and spacecraft charging. According to the O'Shea et al. (2017) numerical analysis, the antennas can only collect charge from impacts that occur in close proximity to the antenna base. Recently, Shen et al. (2021) developed a detailed electrostatic model for a generation of antenna signals, applicable to waveforms measured in the laboratory using a dust accelerator, but neglected the plasma effect.

This article focuses on analyzing the charge collection and induction mechanism, examining it from a theoretical perspective, and applying it to the radio STEREO/WAVES (S/WAVES hereafter) database. In Sect. 2 we present a theoretical model for analyzing the radio instrument response to floating potential perturbations induced by impact-produced electron collection, taking the voltage induced on the spacecraft by the neighboring cloud's ions into account. Section 3 presents results obtained using radio S/WAVES data on the STEREO spacecraft to validate the model and deduce properties of the impact plasma. A summary and discussion of the results are presented in Sect. 4.

2. Modeling of the voltage pulse

2.1. General discussion

In this section we present the theoretical model on which we base our derivation of the dust physical parameters – more precisely of the impact cloud's properties – through statistical analysis of the STEREO data in the next section. This model is an extension of the work of Zaslavsky (2015), which proposed a description, in the linear approximation, of the response of a spacecraft (or an antenna) to the collection of electric charges generated after the hypervelocity impact of a dust grain. This work proved its capability to reproduce most of STEREO's dust impacts shapes, confirming electron collection as the main mechanism through which voltage signals are produced. However, it was unable to explain the observed rise time of the signals – of the order of some tens of microseconds despite a quick analysis of the electron dynamics showing that the collection time should be much smaller. This point, which was left as a question mark in Zaslavsky (2015), was explained by Meyer-Vernet et al. (2017), who showed that the effect of electrostatic influence from the positive ions in the vicinity of the spacecraft needs to be taken into account. Indeed, the negative change in the spacecraft's potential due to the collection of charges, $-Q$, from an initially neutral cloud is almost exactly compensated for by the electrostatic influence from the charges, $+Q$, left unscreened in the close vicinity of the spacecraft. Therefore, Meyer-Vernet et al. (2017) showed that the rise time of the pulse is not controlled by the electron dynamics timescale but by the positive charge timescale, that is, the time needed for the positive charges to

be screened by the photoelectrons or the ambient plasma or to move far enough from the spacecraft for the influence effect to become negligible and for the drop in the potential due to electron collection to become apparent. Another consequence of the influence effect, which was noted in the same paper, is the possible occurrence, on very short timescales, of a precursor in the voltage pulse associated with the electron dynamics. Indeed, a fraction of the electrons escaping away from the spacecraft will leave some ion charge unscreened, inducing a positive change in the spacecraft potential that is not compensated by the collection of negative charges – resulting in the observation of a short voltage pulse, on a timescale typical of the electron dynamics.

These processes were summarized by Mann et al. (2019), although not quantitatively, on the basis of a description through "escaping currents". This description was implicitly based on the description of the variation in the charge, Q_S, in a control volume bounded by a surface, S, enclosing the spacecraft,

$$\frac{\mathrm{d}Q_S}{\mathrm{d}t} = -\oiint_S \vec{j} \cdot \mathrm{d}\vec{S} = -I_{\mathrm{out}} + I_{\mathrm{in}}. \tag{1}$$

One assumes that the control surface is close enough to the spacecraft surface, such that the spacecraft potential is to a good approximation proportional to the charge Q_S. The variation in the spacecraft potential can then be associated with the action of different currents, I_{in} and I_{out}, through the surface, S. Now one also assumes the control surface to be large enough for all the charge generated by impact ionization just after the dust hit to be initially enclosed by it: then, there is no variation in the charge inside the surface and therefore no variation in potential in the first moments after the impact. At that point, some electrons may escape out of the control surface: associated with this escape will be a negative outward current and then a positive voltage pulse (the "electron precursor") in the spacecraft potential times series. In a second time, ions crossing the control surface will then produce a positive outward current and, therefore, a negative drop in the spacecraft potential. Finally, on the longest timescale, currents from the solar wind and photoelectron emission from the spacecraft will lead to the relaxation of the voltage pulse. These correspond to the three stages of the voltage pulse as described by Mann et al. (2019) (T2, T3 and T4 in that paper). This approach is mathematically relevant, and has the advantage of simplicity and pragmatism. On the other hand, it is not fully satisfactory since it leaves the processes occurring inside the control surface undescribed. For instance, it is clear that it is not the crossing of a mathematically abstract – and loosely defined – control surface by electrons or ions that is responsible for the spacecraft potential changes. The changes are physically produced by the collection of, and by the influence from, charges inside the control surface. Another drawback of this approach is that the currents associated with the cloud dynamics appear as ad hoc functions, which are difficult to link to the specific spacecraft geometrical properties.

This motivates our study. In the following, we focus on the case of the positively charged STEREO spacecraft, although the model can of course easily be extended to all spacecraft's charging states and processes. We provide a model that accounts for the collection of negative charges and the exchange of charges with the surrounding solar wind plasma, as was done in Zaslavsky (2015). Here we add to the picture the effect of the electrostatic influence from the positive ion cloud and therefore recover the "slow rise time" and voltage precursor effects, that were absent from that work.

2.2. Electrostatic influence from a point charge

The electrostatic potentials of a system of conductors insulated from one another is a problem that, although not explicitly solvable for arbitrary geometries, has the advantage that the charge carried by each of the conductive elements is linear. Considering our system to be composed of only the dust plasma cloud, of charge Q_{cloud} and potential φ_{cloud}, and the spacecraft (indices sc), the linearity of the problem translates into the existence of a matrix Λ such that

$$\begin{pmatrix} \varphi_{cloud} \\ \varphi_{sc} \end{pmatrix} = \begin{pmatrix} \Lambda_{cloud} & \Lambda_{cloud,sc} \\ \Lambda_{sc,cloud} & \Lambda_{sc} \end{pmatrix} \begin{pmatrix} Q_{cloud} \\ Q_{sc} \end{pmatrix}. \tag{2}$$

Here, Λ is here the inverse of the capacitance matrix, also known as the elastance matrix, of the conductors system. Of course, additional lines and columns can be added in order to account for the electrostatic effects of the dust on other systems (antennas, solar panels, booms, etc.) and of these elements on each other, but in this paper we focus only on the simplest case of the interaction of a dust impact cloud and the spacecraft, neglecting all other capacitive couplings and therefore limiting ourselves to a 2×2 matrix. This choice is made here for simplicity, but a model that includes the coupling to the antennas should be the purpose of a forthcoming study. This would be of particular importance in providing a model for the signals observed in dipole mode on Wind and other spacecraft (Solar Orbiter, Parker Solar Probe), which are known to be produced by electrostatic influence on a particular arm of a dipole (Meyer-Vernet et al. 2014).

Since the size of the spacecraft is very large with respect to the size of the dust impact cloud that influences it (so its self-capacitance is much larger), we can neglect the change in self-capacitance of the spacecraft due to the presence of the cloud in its vicinity and write that

$$\Lambda_{sc} \simeq C_{sc}^{-1} \sim \frac{1}{4\pi\epsilon_0 R_{sc}}, \tag{3}$$

where C_{sc} is the spacecraft capacitance in a vacuum and R_{sc} its size. This parameter is then a good approximation independent of the position of the dust cloud with respect to the spacecraft.

In order to roughly evaluate $\Lambda_{sc,cloud}$, one could assume the dust cloud to be a point charge and the spacecraft to be a conducting sphere of radius R_{sc}, both separated by a distance r. The electrostatic calculation in a vacuum (see e.g., Jackson 1962), as noted by Meyer-Vernet et al. (2017), then gives

$$\Lambda_{sc,cloud}(r) \simeq \frac{1}{4\pi\epsilon_0 R_{sc}} \frac{R_{sc}}{R_{sc} + r}. \tag{4}$$

This evaluation neglects lots of effects, especially the fact that the dust-spacecraft interaction does not occur in a vacuum, and that the interaction potential is screened by the photoelectron sheath. Therefore, we chose to model the mutual elastance, $\Lambda_{sc,cloud}$, by

$$\Lambda_{sc,cloud}(r) = \frac{1}{C_{sc}} F(r), \tag{5}$$

where $F(r)$ is a decreasing function (with a typical length scale, λ_{ph}, the screening length of the photoelectron sheath), with limiting values of 1 for $r \to 0$ and 0 for $r \to \infty$. Naturally, one may choose

$$F(r) = \exp(-r/\lambda_{ph}), \tag{6}$$

but other empirical choices are possible – for instance, $F(r) \propto \exp(-r/\lambda_{ph})/(r + R_{sc})$, to recover the vacuum expression given

by Eq. (4) for small values of r. The function F has to be chosen empirically anyway since it depends on many indeterminate factors, including the geometry of the spacecraft, the geometry of the dust impact cloud, and the structure of the photoelectron sheath.

2.3. Equations for the potential perturbation

Now that we have our model for the electrostatic influence, we can study the effect on the spacecraft potential of a transient as a dust impact. For this we use Eq. (2) to write the derivative of the spacecraft potential,

$$\frac{d\varphi_{sc}}{dt} = \Lambda_{sc} \frac{dQ_{sc}}{dt} + \frac{d}{dt}\left(\Lambda_{sc,cloud} Q_{cloud}\right). \tag{7}$$

The first term of the right-hand side accounts for the time variation of the spacecraft charge. This variation is due to various currents coming from the dust impact cloud, the solar wind plasma and the spacecraft itself through the photoelectric effect (or, very marginally in the case of STEREO, secondary emission). It corresponds to the variation in charges in a control volume that is precisely enclosed by the spacecraft's surface. It reads (neglecting secondary emission)

$$\frac{dQ_{sc}}{dt} = I_{ph}(\varphi_{sc}) + I_{sw}(\varphi_{sc}) + I_{collected}(t), \tag{8}$$

where I_{ph} is the photoelectron current and I_{sw} is the solar wind electron current on the spacecraft surface, which can both be expressed explicitly as a function of φ_{sc} (and of the local plasma parameters) within the orbit-limited approximation (Laframboise & Parker 1973). The $I_{collected}(t)$ is the current due to collected charges from the impact cloud. This equation (that is, Eq. (7) with only the first term of the right-hand side) corresponds exactly to what was solved in the paper by Zaslavsky (2015). It captures the effects related to the changes in the charge carried by the spacecraft: its charging through collection of charges from the impact cloud and its relaxation to equilibrium through charge exchanges with the solar wind. The second term of the right-hand side of Eq. (7) was omitted from that paper, but it is very important: it contains the description of the effects of electrostatic influence.

The solution of Eq. (7) can be obtained by linearizing the expression for the currents around the equilibrium value, $\varphi_{sc,eq}$, of the potential, as was done in Zaslavsky (2015). The potential perturbation, $\delta\varphi_{sc} = \varphi_{sc} - \varphi_{sc,eq}$, is then found to evolve according to the first-order linear differential equation

$$\frac{d}{dt}\delta\varphi_{sc} + \frac{1}{\tau_{sc}}\delta\varphi_{sc} = \frac{1}{C_{sc}}\left(I_{collected} + \frac{d}{dt}\left[F(r(t))Q_{cloud}(t)\right]\right), \tag{9}$$

where τ_{sc} is the linear relaxation time of the spacecraft potential

$$\tau_{sc} = \frac{C_{sc} T_{ph}}{e n_e v_e S_{sc}}, \tag{10}$$

with T_{ph} the photoelectron sheath temperature expressed in electronvolts, n_e the local plasma electron density, $v_e = \sqrt{kT_e/2\pi m_e}$ the electron mean velocity divided by 4, T_e the local plasma electron temperature and S_{sc} the spacecraft conductive surface in contact with the surrounding plasma. The k, e and m_e are Boltzmann's constant, the electron charge, and the electron mass,

respectively. The solution of Eq. (9), assuming the spacecraft is in equilibrium with the surrounding plasma when $t \to -\infty$, is

$$\delta\varphi_{\text{sc}}(t) = \frac{1}{C_{\text{sc}}} e^{-t/\tau_{\text{sc}}} \int_{-\infty}^{t} \left(I_{\text{collected}}(t') + \frac{d}{dt'} \left[F(r(t'))Q_{\text{cloud}}(t') \right] \right) e^{t'/\tau_{\text{sc}}} dt'. \tag{11}$$

This expression can be used in a quite general manner to model the shape of the pulse – as long as the linear assumption is fulfilled, which is the case for the very large majority of the impacts recorded. One can see that the time profile of the voltage perturbation is linked to the time profile of the collected current, $I_{\text{collected}}$, but also to the trajectory, $r(t)$, of the dust cloud around the spacecraft, to the shape of the function F, describing the spacecraft and sheath properties, and to the time profile $Q_{\text{cloud}}(t)$, which is related to the electron dynamics in the cloud and in the sheath.

2.4. A simple model: Streaming ions and massless electrons

In order to obtain a simple model, that relies on a few parameters and is adapted to robust fitting of the large amount of data provided by radio instruments such as S/WAVES, one needs models to be as simple as possible for the source terms in the right-hand side of Eq. (11). We derive in this section the potential perturbation time profile under the simple assumption that the ions are streaming out of the spacecraft surface with a constant velocity, v, and that the motion of the electrons occurs fast enough that it can be considered as instantaneous. This assumption is relevant if the electron dynamical timescale is smaller than the sampling time of the instrument, which is the case, as will be seen in the data analysis section, for the waveforms recorded by S/WAVES. We also consider the possibility that the photoelectrons in the sheath neutralize the ion cloud, since this effect was shown to be important by Meyer-Vernet et al. (2017).

For the function F – which is proportional to the mutual elastance of the cloud-spacecraft system, we use the exponential model Eq. (6) with a cutoff length λ_{ph} on the order of the photoelectron sheath Debye length. Since we consider ions streaming freely out of the spacecraft, the spacecraft-ion cloud distance is given by $r(t) = vt$, with v a constant.

Therefore, the term accounting for electrostatic influence reads

$$\frac{d}{dt} \left(F(r(t))Q_{\text{cloud}}(t) \right) = \left(\frac{dQ_{\text{cloud}}}{dt} + \frac{1}{\tau_{\text{d}}} Q_{\text{cloud}} \right) e^{-t/\tau_{\text{d}}}, \tag{12}$$

where $\tau_{\text{d}} = \lambda_{\text{ph}}/v$ is the ion cloud dynamics timescale, characteristic of its transit time (or expansion time) in the photoelectron sheath. Now one must model the effects related to the motion of the cloud's electrons. For this, we use the following equation, which expresses the change in the cloud's charge due to currents of electrons from it and the neutralization of the cloud by the photoelectrons on a typical timescale τ_{ph}:

$$\frac{d}{dt} Q_{\text{cloud}} + \frac{1}{\tau_{\text{ph}}} Q_{\text{cloud}} = -I_{\text{collected}}(t) - I_{\text{escaped}}(t), \tag{13}$$

where I_{escaped} is the current of charges escaping away from the spacecraft.

The assumption that the escape and collection of the electrons is instantaneous (the "massless electron assumption") translates into the following expressions for the currents

$$I_{\text{collected}}(t) = -(1 - \epsilon)Q\delta(t), \qquad I_{\text{escaped}}(t) = -\epsilon Q\delta(t), \tag{14}$$
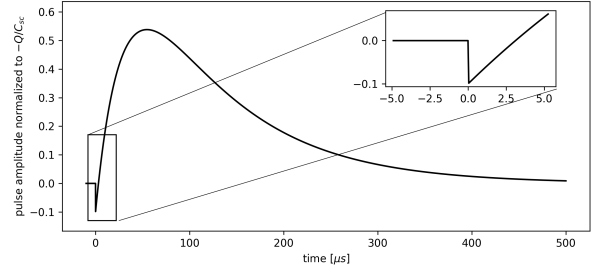
Fig. 1. Simulation of the signal shape through proposed models for the effect on the spacecraft potential of a transient dust impact. The curve is obtained from the simple model, assuming the electron collect (escape) to be instantaneous, $\tau_{\text{e}} \approx 0$ (Eq. (16)). The ratio between escaped charge and total charge is $\epsilon = 0.1$, and timescales parameters are $\tau_{\text{sc}} = 100\,\mu s$ and $\tau_{\text{ion}} = 30\,\mu s$. The zoomed-in portion of the plot (top right) provides an insight into the pre-shoot signal shape.

where $Q > 0$ is the total amount of free charges released in the impact ionization process, ϵ is the fraction of electrons escaping away from the spacecraft, and $\delta(t)$ is Dirac's delta function. It is then clear that one must have, from the Eq. (13),

$$Q_{\text{cloud}}(t) = e^{-t/\tau_{\text{ph}}} \int_{-\infty}^{t} \left(-I_{\text{collected}}(t') - I_{\text{escaped}}(t') \right) e^{t'/\tau_{\text{ph}}} dt'$$
$$= Q e^{-t/\tau_{\text{ph}}} H(t), \tag{15}$$

where $H(t)$ is Heaviside's step function.

All the source terms appearing in the right-hand side of Eq. (11) have now been given by an explicit expression, and it is straightforward to compute the integral. The potential perturbation obtained is

$$\delta\varphi_{\text{sc}}(t) = \left[\frac{\epsilon Q}{C_{\text{sc}}} e^{-t/\tau_{\text{sc}}} - \frac{Q}{C_{\text{sc}}} \frac{1}{1 - \tau_i/\tau_{\text{sc}}} \left(e^{-t/\tau_{\text{sc}}} - e^{-t/\tau_i} \right) \right] H(t). \tag{16}$$

where $\tau_i = \tau_{\text{d}}\tau_{\text{ph}}/(\tau_{\text{d}} + \tau_{\text{ph}})$ is the characteristic rise time of the pulse. It is on the order of the smaller of the ion characteristic timescale, τ_{d}, and the time for the cloud to collect enough ambient photoelectrons to be able to shield its charge, Q (Meyer-Vernet et al. 2017).

The shape of this time profile is illustrated in Fig. 1. In the case where the ion timescale, τ_i, is small compared to the relaxation time, τ_{sc}, this can easily be simplified again, but we keep the effect of the finite value of τ_i/τ_{sc}, since, as we shall see, in the data this ratio is on the order of $\sim 1/3$.

2.5. More complicated model: Taking additional effects into account

The previous section presents a simple model, which, as will be seen in the next section, is sufficient for modeling and understanding the broad majority of the events recorded by S/WAVES. But the expression (11) for $\delta\varphi_{\text{sc}}(t)$ also makes it possible to account for a variety of other effects, by introducing more refined functions for the collection (escape) currents, the mutual elastance, or the ion cloud trajectory. In this section we briefly explore some possible refinements.

First, one could account for the finite dynamic time, τ_{e}, of the electrons. This can be done by using for $I_{\text{collected}}$ and I_{escaped} functions that introduce a characteristic timescale. The most natural choice is probably a Gaussian function with variance τ_{e}^2. In general, it will then be necessary to perform a numerical integration of the Eqs. (11) and (15). If it is necessary to reach an even finer

level of modeling for the electron dynamics, one could also take different timescales for the collection and escape of the electrons into account. Of course, such a fine modeling given the time resolution of the electric waveform sampler on board spacecraft, would probably not make much sense in the context of space measurements.

Another refinement could also be obtained by accounting for more complex trajectories, $r(t)$, of the ion cloud. Here again, the computation for an arbitrary trajectory requires numerical integration. In any case, and as will be seen in the next section, since the screening timescale, τ_{ph}, is smaller than the dynamics timescale, τ_i, the precise dynamics of the ion cloud should not strongly affect the shape of the pulse.

Finally, a finer description of the pulses could also be reached through a better modeling of the spacecraft coupling to the cloud. Such a model should include a precise electrostatic description of the spacecraft through a carefully computed elastance matrix that includes all the conductive elements and in particular the antennas, the potential of which was considered as constant in our simplified study. The computation of such an elastance matrix was recently performed by Shen et al. (2021) and compared to the results of laboratory experiments of dust impacts on a model spacecraft.

A full model may also include a description of the cloud internal dynamics and expansion and of the trajectory vector, $r(t)$, of the cloud center of mass in the vicinity of the spacecraft. Solving for such a complicated model would require complex numerical simulations. But as we shall see in the next section, the present model enables us to reproduce most of the observed voltage pulses and provides a support for interpreting the more complex ones.

3. S/WAVES Time Domain Sampler data

In the present study, we analyze dust grain impacts from the two STEREO satellites, A and B, which were launched in 2006 and are orbiting at 1 AU. The S/WAVES radio instrument is constituted by three orthogonal 6 m long antennas connected to a sensitive radio receiver. The instrument can perform observations in the frequency range 2.5 kHz to 17 MHz (Bale et al. 2008; Bougeret et al. 2008). The Time Domain Sampler (TDS) is a subsystem of the S/WAVES instrument that generates high-cadence time series of voltage pulses for each monopole. Bougeret et al. (2008) provided comprehensive information on TDS and how signals are collected, filtered, and digitized. In this article, we use the data provided by TDS to study the voltage variations occurring when a dust grain impacts the spacecraft.

3.1. Presentation of S/WAVES TDS data

Two TDS data sets are available: (1) the TDSmax data give the maximum amplitude or peak signal detected on the antennas each minute; and (2) the TDS Events data set provides complete voltage time series captured by the instrument with a sampling rate of a few µs (Zaslavsky et al. 2012). We used the TDS Events data set. Measurements can be conducted in several modes with different time resolution and total event duration. For this study snapshots with a time resolution of 4 or 8 ms (which constitute the vast majority of the signals) are used. They correspond to snapshot durations of 65 ms and 130 ms. Signals with a high amplitude are automatically selected for telemetry out of a continuously recorded waveform. A low-pass filter is used with the S/WAVES signal to prevent aliasing by matching the sam-
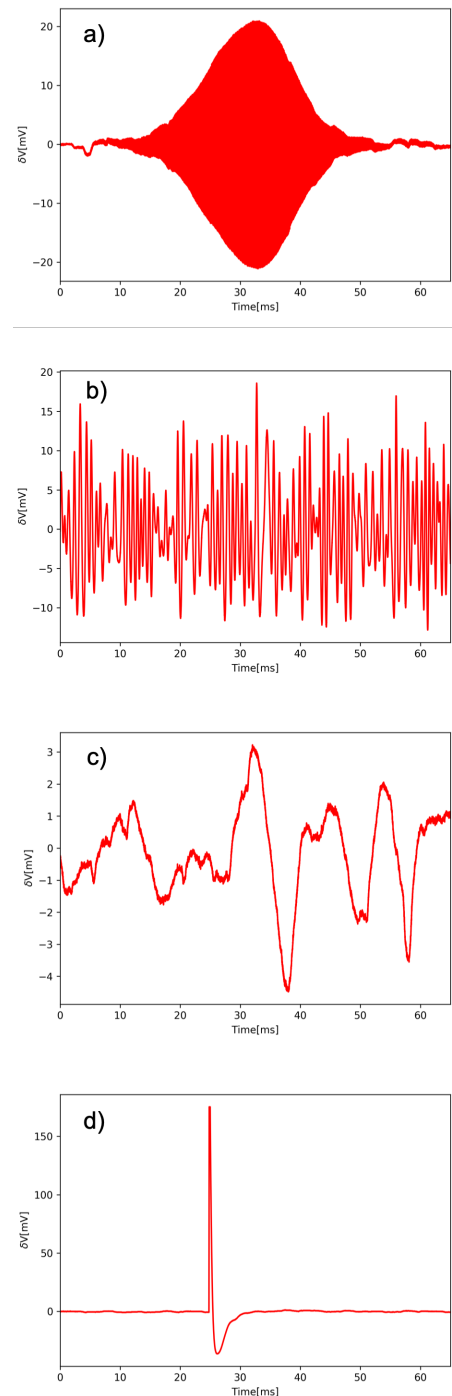

Fig. 2. Different examples of electrical signals obtained by S/WAVES/TDS: (*a*) Langmuir waves, (*b*) plasma wave around the local cyclotron frequency, (*c*) low-frequency density fluctuation, and (*d*) dust event.

pling channel. Depending on the time resolution of the sample, low-pass filters can be either 108 kHz or 54 kHz (Bougeret et al. 2008).

An analysis of the electrical waveforms of the TDS Events reveals that they contain a variety of signals with distinctly different shapes. The observed signals include variations in electric potential due to inhomogeneities of local plasma density. Panels a–c of Fig. 2 illustrate the types of waves present in the data: plasma waves oscillating at the local plasma frequency (Langmuir waves), plasma waves around the local cyclotron
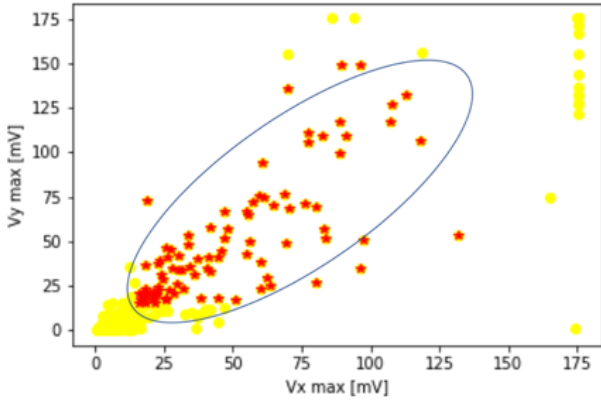
Fig. 3. Maximum signal amplitude recorded on X and Y monopoles in the period from 2008 October 1 to 2008 December 31. Red stars represent only the dust signal.

frequency, and low-frequency density fluctuation. The impact of energetic particles such as protons and electrons from the Solar System or coming from galactic origin can also produce an electric field signal. All these signals are well known and have been the subject of many works (e.g., Kellogg et al. 1996; Bale et al. 1998; Henri et al. 2011; Malaspina et al. 2011). Panel d of Fig. 2 shows a signal of characteristic shape recognized as a dust impact signal (Zaslavsky et al. 2012). This signal is characterized by an abrupt increase in voltage followed by a rapid relaxation to equilibrium potential. There are two distinct types of these signals: a strong peak detected by one monopole or a similarly shaped signal appearing simultaneously on all three antennas. Our study is focused on signals almost simultaneously generated on all three antennas.

3.2. Survey of TDS dust data

The TDS waveform sampler on-board both STEREO satellites has observed a large number of voltage pulses interpreted as dust impact signatures since the launch of the mission. Our study examines TDS events recorded from 2007 to 2018 for STEREO A and from 2007 to 2015 for STEREO B.

As illustrated by Fig. 2, the data set contains snapshots of a wide variety of phenomena. Therefore, we need to find a way to automatically identify only very sharp and impulsive events, recognized as dust events, in between all those other varieties of occurrences. To do so, we set the threshold at an amplitude greater than 15 mV to identify shapes clearly and lower than 175 mV to eliminate events that saturate the receiver. Also, since we wanted the amplitude to be roughly the same on all three antennas, our third criterion is defining a cone that will only involve simultaneously occurring. Figure 3 shows the distribution of the observed maximum amplitudes over three months on the monopole pair X and Y (the distribution is the same for the other monopole pairs). Accordingly, if we consider measurements of each of the three monopoles, dust events would likely be concentrated within the cone of a particular aperture. In parallel with dust events, we have also detected Langmuir waves with a corresponding amplitude. Insofar as we limit the signal to just two points at an intersection of one-third of the height of the maximum amplitude, we eliminate all Langmuir waves from our obtained dust database. An auto-detection algorithm that meets all the above criteria was tested using three months of observations over which several dozen measurements of dust impacts

were made; it was found to be effective in detecting dust-related events. Then we applied it to the entire TDS Events data set.

We have gathered all dust events measured on all three monopoles simultaneously with maximum amplitudes between 15 and 175 mV from the TDS Events data set in 2007–2018 to create a single database. The resulting database contains 116544 events, 76086 on STEREO A and 40458 on STEREO B. In order to check the validity of the simple theoretical model presented in Sect. 2, a statistical analysis based on the events in the database was conducted. Due to the fact that each impact creates a pulse on each of the three monopoles, there are 349632 individual pulses.

3.3. Analysis of individual impacts

Using the simple model from Sect. 2, we fitted each electric pulse observed by the S/WAVES instrument on board STEREO A and B, selected as discussed in Sect. 3.2. Several parameters that characterize the response of the spacecraft and the collection dynamics of particles are derived and discussed. To fit the signal detected at each monopole, we used the function

$$\phi(t) = A(1/(1 - T_1/T_2))(e^{(-t/T_2)} - e^{(t/T_1)}) - Be^{(-t/T_2)}, \quad (17)$$

with a Levenberg-Marquardt least-squares minimization method. This function is the same as the theoretical Eq. (16), with the free parameters of our fitting routine being: $T_2 \equiv \tau_{sc}$ is the spacecraft relaxation timescale, which is the time it takes for the spacecraft to return to equilibrium; $T_1 \equiv \tau_i$ is the ion characteristic timescale, $A \equiv \Gamma Q/C_{sc}$ is the total charge, and $B \equiv \epsilon\Gamma Q/C_{sc}$ represents the escaped charge. Figure 4 shows voltage pulses recorded by TDS as well as the Levenberg-Marquardt fit to TDS data with the function $\delta V(t) = -\Gamma\delta\varphi_{sc}$ from Eq. (17), with $\Gamma \sim 0.5$ the antennas' gain due to capacitive coupling with the base (Bale et al. 2008). These examples demonstrate a good match between the data and the model, except for the negative voltage overshoot occurring after the main pulse.

As discussed in the previous subsection, anti-aliasing low-pass filters are set up at the entrance of each sampling channel. It is known that the effect of such filters on a sharp impulsive signal will produce an artificial distortion of the signal, such as these overshoots. In order to correct this effect, we deconvolved the signal using the inverse low-pass filter. The inverse low-pass filter was chosen in accordance with the sampling channel currently being used, which is typically 108 kHz or 54 kHz in the case of S/WAVES (Bougeret et al. 2008). Some overshoots remain even after the correction, while others completely disappear. It is therefore likely that the remaining overshoots are not artificial, but rather due to the charges of the monopoles themselves (Zaslavsky 2015). Still, this effect is difficult to reliably quantify since the correction by the filter can be quite sensitive to the phase calibration of the filters. In this study, we chose not to take the variation in the antenna's potential into account.

As a summary, we fitted all data from our data base with the Levenberg-Marquardt least-squares minimization method using Eq. (17). As discussed in Sect. 2, we expect that the time required for the spacecraft to return to equilibrium is significantly longer than the ion characteristic timescale (i.e., $\tau_{sc} > \tau_i$). We removed any event that does not meet this condition; consequently, from the initial 349632 events, we kept about 70% of the events.
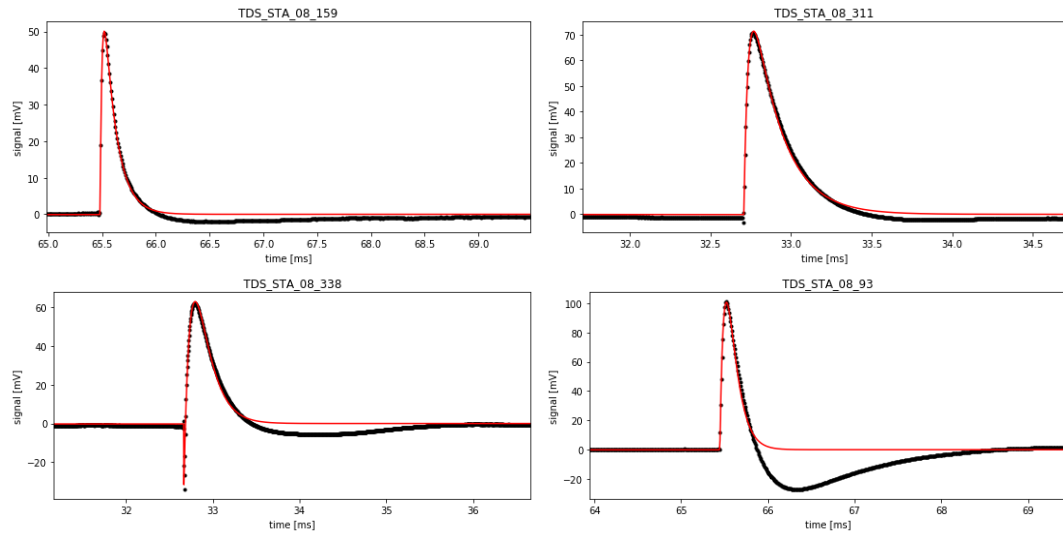
Fig. 4. Signals of dust impact recorded by STEREO A in 2008. Black dots represent TDS data. The red line represents the fitting results made with a Levenberg-Marquardt method from Eq. (17) and function $\delta V(t) = -\Gamma \delta \varphi_{\rm sc}$.
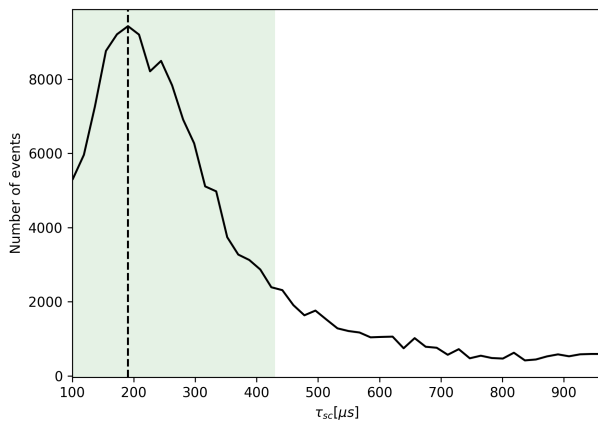

Fig. 5. Histogram of the parameter $\tau_{\rm sc}$. The green section on the histogram indicates the extreme values of the parameter calculated from Eq. (10) (see text for details). Around 80% of the obtained values for $\tau_{\rm sc}$ are inside the green section. The dashed vertical line represents the most probable obtained value for the parameter, $\tau_{\rm sc} \sim 190\,\mu$s. The median value of the distribution is 270 μs.
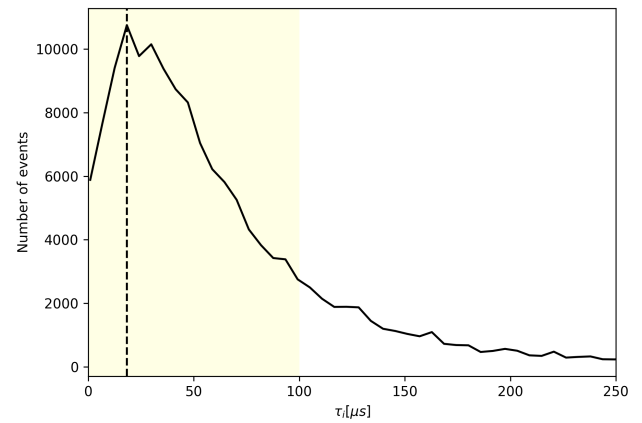
Fig. 6. Histogram of the parameter τ_i. The yellow section includes all the obtained values below 100 μs (the threshold for the $\tau_{\rm sc}$). More than 80% of the obtained τ_i is inside the yellow section. The vertical dashed line represents the most probable obtained value for the parameter, $\tau_i \sim 18\,\mu$s.

3.4. Statistical analysis of S/WAVES signals, presentation and discussion

3.4.1. Linear relaxation timescale

Figure 5 shows a histogram of the parameter $\tau_{\rm sc}$, which describes the discharge timescale of the spacecraft through exchange of charges with the solar wind and the photoelectron emission from the spacecraft. The histogram contains all the values for the $\tau_{\rm sc}$ parameter that were obtained for each monopole.

The linear relaxation time of a spacecraft is given by Eq. (10) in Sect. 2.3. One can see that $\tau_{\rm sc}$ depends on the geometry of the spacecraft (through its surfaces), as well as on the local plasma and photoelectron parameters. It can be evaluated as follows: STEREO satellites orbit at 1 AU, where, typically, $n_e \simeq [1-10]\,{\rm cm}^{-3}$ and $T_{\rm e} \sim 10\,{\rm eV}$ (Issautier et al. 2005). Spacecraft parameters are, as an order of magnitude, $C_{\rm sc} \simeq 200$ pF, $S_{\rm sc} \simeq 10$ m^2, and the photoelectron temperature is typically $T_{\rm ph} \simeq 3\,{\rm eV}$. On the basis of these parameters, one can estimate the relaxation

time for STEREO, $\tau_{\rm sc} \sim 100-430\,\mu$s. These limits are represented by the green-shaded area in Fig. 5. One can see that the distribution of the observed relaxation times peaks roughly in the middle of the green area and that most of the data (∼80%) fall within the expected range. The most probable value and median observed values are 190 μs and 270 μs, respectively. This quite unambiguously shows that, consistent with the standard interpretation, the decay time of the pulses can be identified with the relaxation time of the spacecraft through the exchange of charges with the surrounding plasma after the spacecraft body has collected a certain amount of charge.

3.4.2. Ion characteristic timescale

Figure 6 presents a histogram of the ion dynamics timescale parameters, τ_i. The vast majority of the obtained values for parameter τ_i are smaller than 100 μs. As noted in Sect. 2.2, this characteristic ion timescale, τ_i, is the smallest of the quantities $\lambda_{\rm ph}/v$ and the time for the cloud's ions to collect enough
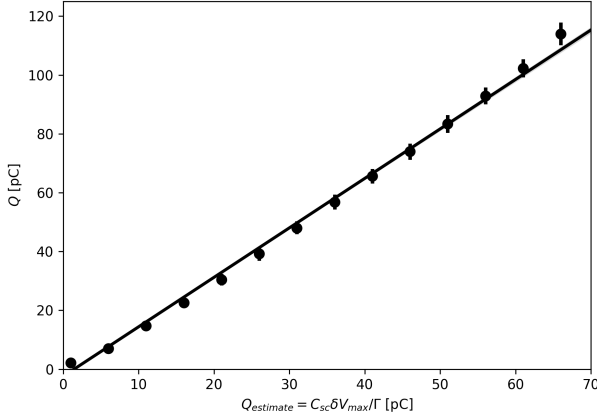
Fig. 7. Total charge calculated from $Q_{\text{estimate}} = C_{\text{sc}}\delta V_{\text{max}}/\Gamma$ as a function of the total charge, Q, obtained from fitting parameter A (Eq. (17)). The binwidth is 5 pC. The error bars show the standard deviation of the distribution of Q in each bin.

ambient photoelectrons to be shielded by them, as estimated by Meyer-Vernet et al. (2017). Using Eqs. (11) and (4) of that paper, the latter can be simplified into

$$\tau_{\text{ph}} \simeq \left(3Q/2\pi I_{\text{ph0}}\right)^{1/3} /v^{2/3}, \tag{18}$$

where I_{ph0} is the spacecraft photoelectron current at zero potential. Assuming $I_{\text{ph0}} \simeq 20 \, \mu\text{A/m}^2$ (which yields $\lambda_{\text{ph}} \simeq 0.9$ m), we deduce from the most commonly observed value $\tau_i = 18 \, \mu\text{s}$ (Fig. 6) with the average charge $Q \simeq 40$ pC, the cloud's propagation and expansion speed to be $v \simeq 13 \, \text{km s}^{-1}$. This result depends weakly on the badly known photoelectron current and is consistent with our estimate that $\tau_i \simeq \tau_{\text{ph}}$ since the most commonly observed value of τ_i is much smaller than λ_{ph}/v.

These values can be compared with reasonable agreement to measurements from laboratory experiments and numerical simulations. For instance, our results match those of Lee et al. (2012), who measured the ion expansion speed in laboratory experiments and found $v \geq 10 \, \text{km s}^{-1}$. According to their results, plasma detection occurred most often from impacts on positively charged targets (such as STEREO). In contrast, detection rates for negatively charged and unbiased targets varied depending on the material. Based on multi-physics simulations of plasma production from hypervelocity impacts, Fletcher et al. (2015) reported a similar range of values.

3.4.3. Electron collection

The value of total charge, Q, is derived from the parameter $A \equiv \Gamma Q/C_{\text{sc}}$, which is obtained through the fitting. It should be noted that the value of A obtained on each monopole differs a bit (probably because of the influence effect on the monopoles, which is neglected in this work). However, since the total amount of charge released during an impact must be the same for all monopoles, we defined the total charge as the mean of the values obtained by fitting each monopole separately. For both STEREO spacecraft we used values for the spacecraft capacitance of $C_{\text{sc}} = 200$ pF, and for the antenna-spacecraft coupling $\Gamma \simeq 0.5$ (Bale et al. 2008). As can be seen in the figure, values of Q lie within the range 8–120 pC.

The link between the total charge generated Q, and both the mass, m, and velocity, V, of the impacting dust particles with respect to the spacecraft was studied recently using hypervelocity impact experiments on materials relevant to STEREO satellites (Collette et al. 2014). In the case of impacts on the thermal coating that covers most of the spacecraft, the result obtained is $Q_{[C]} \simeq 1.7 \times 10^{-3} \, m_{[\text{kg}]} V_{[\text{km.s}^{-1}]}^{4.7}$. Based on this relationship, we can, by assuming a typical velocity for the impacts, translate the charge scale into a mass scale. For particles orbiting at Keplerian speeds, we can assume a typical impact velocity of $30 \, \text{km.s}^{-1}$; the obtained mass range is then $20 - 340 \times 10^{-17}$ kg, which corresponds to the size interval $2 - 5 \, \mu\text{m}$ (we assume a mass density $\rho = 2.5 \, \text{g.cm}^{-3}$). On the other hand, it has appeared that the fluxes observed on several spacecraft, including STEREO (Zaslavsky et al. 2012), but also Parker Solar Probe (Pusack et al. 2021) and Solar Orbiter (Zaslavsky et al. 2021), are dominated by impacts from a population of dust particles produced close to the Sun and pushed away along hyperbolic orbits by the radiation pressure, the β meteoroids. The velocity of these particles at 1 AU depends quite importantly on their origin and composition, through the value of the β parameter equal to the ratio of the radiation pressure force to the gravitational force on the dust grain. For dust of asteroidal origins, an order of magnitude of the velocity at 1 AU is $80 \, \text{km.s}^{-1}$ (Wilck & Mann 1996). Using this value we obtain masses and sizes ranging from 0.4 to 6×10^{-17} kg, and from 0.07 to 0.17 μm, respectively, which is comparable to the masses and sizes of grains detected on the cited missions.

Figure 7 shows the total charge, Q, obtained through the fitting procedure, as a function of the charge Q_{estimate} estimated with the approximation $Q_{\text{estimate}} = C_{\text{sc}}\delta V_{\text{max}}/\Gamma$ – the formula that has been used for several space missions (e.g., Zaslavsky et al. 2012) when waveform data are not available for each event. Figure 7 shows that this rough estimate is very well correlated with the total charge, Q, deduced from fitting the waveform. The slope is 1.63 ± 0.01, with 0.8 the factor of correlation. This high correlation justifies the use of the formula $A \equiv \Gamma Q/C_{\text{sc}}$ when no precise waveform data are available. However, this study shows that this formula underestimates the charge by around 30% (at 1AU).

This underestimation has had some consequences on the estimation of particle size, in previous studies (e.g., Zaslavsky et al. 2012). Since we have seen that size is linked to Q by $s \propto Q^{1/3}$, we can estimate that the size, s, must be underestimated by around 10% – which is quite small given all the other sources of uncertainties.

3.4.4. Electron escape

We finally turn our attention to the electron escape current. Figure 8 shows value of the amount of charge escaping the spacecraft, ϵQ, as a function of the estimated total cloud charge, Q. The standard deviation shown as error bars gives an estimate of the width of the distribution of escaped charge in each bin. For this figure we choose only events exhibiting a voltage precursor larger than 5 mV. Our database contains about 20% of such events. Figure 9 shows the percentage of events with precursor amplitude larger than the threshold concerning the total charge amount Q.

Figure 8 shows that both are almost linearly correlated (at least up to 70 pC), implying that the fraction of escaping charge, ϵ, is almost a constant. The slope of the curve, obtained by linear regression, provides a value of $\epsilon = 0.085 \pm 0.004$, where the uncertainty correspond to a 95% confidence interval on the value of the slope.

To our knowledge, this is a novel result. It shows that, on average and pretty much independently of the total amount of
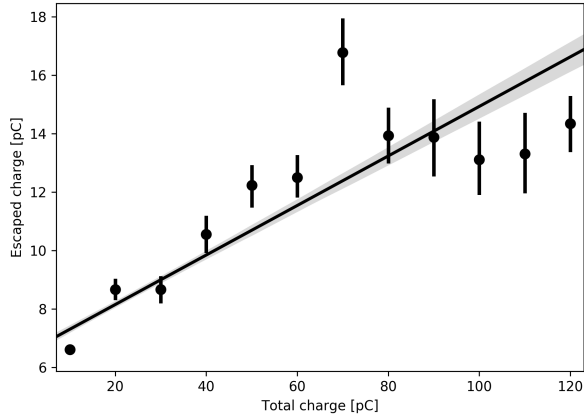
Fig. 8. Escaping charge, ϵQ, as a function of the total charge released in the cloud, Q. The points show the average of the values of ϵQ per bins of values of Q. The binwidth is $10\,\mathrm{pC}$. The error bars show the standard deviation of the distribution of ϵQ in each bin.
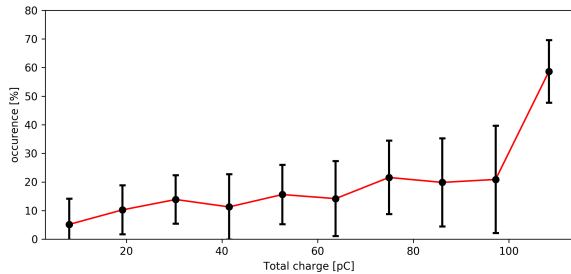

Fig. 9. Histogram of the occurrence of events with precursor amplitude larger than 5 mV with respect to the total charge amount. The error bars show the standard deviation of the distribution. The binwidth is $12\,\mathrm{pC}$.

charge in the cloud, around 8% of this charge escapes the spacecraft. This offers, for instance, a way to evaluate at least an order of magnitude of the amount of charge released during an impact that saturates the instrument if a precursor is associated with this event.

This result has a further interesting consequence. It enables us to estimate the temperature of the impact-produced electrons as follows. Roughly half of such electrons are expected to move toward the spacecraft initially and recollected, provided the spacecraft potential is positive. Among the other half (those initially moving outward), only those with an energy (in eV) exceeding the spacecraft potential, φ_{sc}, will escape. Assuming a Maxwellian distribution of temperature T (in eV), this yields

$$\epsilon = 0.5 e^{-\varphi_{sc}/T}. \tag{19}$$

With $\epsilon \simeq 0.08$ and $\varphi_{sc} = 5\,\mathrm{V}$, we obtain $T = 2.7\,\mathrm{eV}$. This result is close to the value $T = 2.5\,\mathrm{eV}$ found by Fletcher et al. (2015) and to all the previous estimates, which indicated that the impact electron temperature is a few eV.

Recently, impulsive magnetic signals have been detected by search coils associated with very large amplitude (saturating) signals on the monopoles of Parker Solar Probe and Solar Orbiter (T. Dudot de Wit, M. Kretzschmar, priv. comm.). Such signals are likely produced by the current generated by electrons escaping from the spacecraft. In this context, our measurement takes on a supplementary interest since it help us to evaluate the escaping current from the amplitude of the pre-shoot. Indeed, one must have $I_{escape} \sim \epsilon Q/\tau_e$, where τ_e is the timescale associated with the electron dynamics. As discussed previously, this

timescale has been neglected ($\tau_e \sim 0$) in the present study. This was justified by the fact that in nearly every case the rise time of the voltage precursor is not time-resolved by the TDS instrument, even when it is functioning at it highest time resolution of $4\,\mu s$. Therefore, this time resolution can be safely considered as a higher limit on τ_e, and one can evaluate

$$I_{escape} \gtrsim \frac{\epsilon Q}{4 \times 10^{-6}}. \tag{20}$$

The amplitude of the magnetic pulses must be on the order of $\delta B \sim \mu_0 I_{escape}/2\pi R$, with R the average distance between the outflowing electrons and the magnetic probe. We can then expect the amplitude of the magnetic pulse to be linearly related to the amplitude of the voltage precursor. Checking the linearity of this relation on a statistically relevant set of observed magnetic pulses would provide an interesting test for the hypothesis that the magnetic pulses are indeed produced by the current of escaping electrons.

Moreover, one can use the value of the parameter ϵ derived from our observations to estimate the size of the dust that produce magnetic pulses. For instance, an escaping current that produces a magnetic pulse of amplitude $B_{obs} \sim 0.5$ nT, taking for R a value typical of the spacecraft size, ~ 1 m, should be $I_{escape} \sim 2\pi R_{sc} B_{obs}/\mu_0 \sim 3$ mA. Now assuming that the value of ϵ stays constant ~ 0.08 even for large values of Q, this current would correspond to a total impact charge of $Q \sim I_{escape}\tau_e/\epsilon \sim 100$ nC. For impact speeds of $50 - 100\,\mathrm{km.s^{-1}}$ (relevant for Solar Orbiter and Parker Solar Probe; cf. Page et al. 2020), this would give masses of $m \sim 10^{-14}$ kg or sizes of a few microns. This is an interesting test for the hypothesis that the magnetic pulses are indeed produced by the current of escaping electrons.

4. Conclusions

1. In this study we present a theoretical model for the generation of voltage pulses by the collision of dust grains onto a spacecraft. Our work, in the continuation of previous studies (Zaslavsky 2015; Meyer-Vernet et al. 2017), provides for the first time an analytical formula describing the voltage pulse as a consequence of the combined effects of charge collection by the spacecraft and electrostatic influence from charges in its vicinity. We validate our model using data from the S/WAVES instrument at 1 AU.

2. We used the S/WAVES TDS instrument to determine the four independent free parameters appearing in our model (total ion charge, Q, fraction of escaping charge, ϵ, rise timescale, τ_i, and relaxation timescale, τ_{sc}) by fitting our model to the waveform data using a least-square Levenberg-Marquardt technique. This enabled us to obtain the first in situ measurements of parameters such as the electron escape current and the temperature of the electrons in the impact cloud ($T \sim 2.5\,\mathrm{eV}$).

3. Our study is consistent with the idea that the pulse's rise time largely exceeds the spacecraft's short timescale of electron recollection. When the electrons are recollected, the positive ions are still very close to the spacecraft since $m_i \gg m_e$. Hence, they produce a voltage of the opposite sign to that produced by the electron recollection. Therefore, the rise time of the signal is determined by the voltage induced on the spacecraft by the cloud's positive ions (Meyer-Vernet et al. 2017). Moreover, obtained values for the rise time give us insight into the propagation speed of the ion cloud. As far as we know, this is the first time that information about the

velocity of ion clouds was calculated from data, and we compared the results with the values obtained in numerical simulations and laboratory instruments. Calculations based on numerical simulations (Fletcher et al. 2015) and laboratory experiments (Lee et al. 2012) match our results.

4. We found that the amount of charge escaping the spacecraft and the estimated total cloud charge are almost linearly correlated. Recently detected impulsive magnetic signals associated with saturating signals on the monopoles of Parker Solar Probe and Solar Orbiter are likely related to the electrons escaping from the spacecraft. In this context, our model takes on a supplementary interest since it helps us evaluate the escaping current from the amplitude of the precursor.

5. The effect of the potential induced by the cloud's ions on the antennas, expected to be small on STEREO, could explain the minor differences between the voltages measured on the three monopole antennas. However, on other missions where the antennas are located on different sides of the spacecraft, for example WIND, Parker Solar Probe, and Solar Orbiter, this effect should produce very different voltages on different antennas and therefore enable dust detection in dipole mode, as first suggested by Meyer-Vernet et al. (2014).

References

Aubier, M. G., Meyer-Vernet, N., & Pedersen, B. M. 1983, Geophys. Rev. Lett., 10, 5
Bale, S. D., Kellogg, P. J., Larsen, D. E., et al. 1998, Geophys. Rev. Lett., 25, 2929
Bale, S. D., Ullrich, R., Goetz, K., et al. 2008, Space Sci. Rev., 136, 529
Bougeret, J. L., Kaiser, M. L., Kellogg, P. J., et al. 1995, Space Sci. Rev., 71, 231
Bougeret, J. L., Goetz, K., Kaiser, M. L., et al. 2008, Space Sci. Rev., 136, 487
Collette, A., Grün, E., Malaspina, D., & Sternovsky, Z. 2014, J. Geophys. Res. (Space Phys.), 119, 6019
Collette, A., Meyer, G., Malaspina, D., & Sternovsky, Z. 2015, J. Geophys. Res. (Space Phys.), 120, 5298
Fletcher, A., Close, S., & Mathias, D. 2015, Phys. Plasmas, 22, 093504
Gruen, E., Fechtig, H., Kissel, J., et al. 1992, A&AS, 92, 411
Grün, E., & Dikarev, V. 2009, Landolt Börnstein, 4B, 644
Gurnett, D. A., Grun, E., Gallagher, D., Kurth, W. S., & Scarf, F. L. 1983, Icarus, 53, 236
Gurnett, D. A., Ansher, J. A., Kurth, W. S., & Granroth, L. J. 1997, Micron-Sized Dust Particles Detected in the Outer Solar System by the Voyager 1 and 2 Plasma Wave Instruments, National Aeronautics and Space Administration Report
Gurnett, D., Kurth, W., Hospodarsky, G., Persoon, A., & Cuzzi, J. 2004, AGU Fall Meeting Abstracts, 2004, P51C–06
Henri, P., Meyer-Vernet, N., Briand, C., & Donato, S. 2011, Phys. Plasmas, 18, 082308
Issautier, K., Perche, C., Hoang, S., et al. 2005, Adv. Space Res., 35, 2141
Jackson, J. D. 1962, Classical Electrodynamics
Kellogg, P. J., Monson, S. J., Goetz, K., et al. 1996, Geophys. Rev. Lett., 23, 1243
Kurth, W. S., Averkamp, T. F., Gurnett, D. A., & Wang, Z. 2006, Planet Space Sci., 54, 988
Laframboise, J. G., & Parker, L. W. 1973, Phys. Fluids, 16, 629
Lee, N., Close, S., Lauben, D., et al. 2012, Int. J. Impact Eng., 44, 40
Lhotka, C., Rubab, N., Roberts, O. W., et al. 2020, Phys. Plasmas, 27, 103704
Malaspina, D. M., Cairns, I. H., & Ergun, R. E. 2011, Geophys. Rev. Lett., 38, L13101
Mann, I., Meyer-Vernet, N., & Czechowski, A. 2014, Phys. Rep., 536, 1
Mann, I., Nouzák, L., Vaverka, J., et al. 2019, Ann. Geophys., 37, 1121
Meyer-Vernet, N., Aubier, M. G., & Pedersen, B. M. 1986, Geophys. Rev. Lett., 13, 617
Meyer-Vernet, N., Moncuquet, M., Issautier, K., & Lecacheux, A. 2014, Geophys. Rev. Lett., 41, 2716
Meyer-Vernet, N., Moncuquet, M., Issautier, K., & Schippers, P. 2017, J. Geophys. Res. (Space Phys.), 122, 8
Oberc, P. 1996, Adv. Space Res., 17, 105
Oberc, P., Parzydlo, W., & Vaisberg, O. L. 1990, Icarus, 86, 314
O'Shea, E., Sternovsky, Z., & Malaspina, D. M. 2017, J. Geophys. Res. (Space Phys.), 122, 864
Page, B., Bale, S. D., Bonnell, J. W., et al. 2020, ApJS, 246, 51
Pusack, A., Malaspina, D. M., Szalay, J. R., et al. 2021, Planet. Sci. J., 2, 186
Shen, M. M., Sternovsky, Z., Garzelli, A., & Malaspina, D. M. 2021, J. Geophys. Res. (Space Phys.), 126, e29645
Srama, R., Ahrens, T. J., Altobelli, N., et al. 2004, Space Sci. Rev., 114, 465
Tsurutani, B. T., Clay, D. R., Zhang, L. D., et al. 2003, Geophys. Rev. Lett., 30, 2134
Vaverka, J., Pavlů, J., Nouzák, L., et al. 2019, J. Geophys. Res. (Space Phys.), 124, 8179
Wilck, M., & Mann, I. 1996, Planet Space Sci., 44, 493
Ye, S. Y., Vaverka, J., Nouzak, L., et al. 2019, Geophys. Rev. Lett., 46, 941
Zaslavsky, A. 2015, J. Geophys. Res. (Space Phys.), 120, 855
Zaslavsky, A., Meyer-Vernet, N., Mann, I., et al. 2012, J. Geophys. Res. (Space Phys.), 117, A05102
Zaslavsky, A., Mann, I., Soucek, J., et al. 2021, A&A, 656, L18

B

FIRST DUST MEASUREMENTS WITH THE SOLAR ORBITER RADIO AND PLASMA WAVE INSTRUMENT

Astronomy & Astrophysics

Special issue

First dust measurements with the Solar Orbiter Radio and Plasma Wave instrument

A. Zaslavsky[1], I. Mann[2], J. Soucek[3], A. Czechowski[4], D. Píša[3], J. Vaverka[5], N. Meyer-Vernet[1], M. Maksimovic[1], E. Lorfèvre[6], K. Issautier[1], K. Rackovic Babic[1,7], S. D. Bale[8,9], M. Morooka[10], A. Vecchio[11,1], T. Chust[12], Y. Khotyaintsev[10], V. Krasnoselskikh[8,13], M. Kretzschmar[13,14], D. Plettemeier[15], M. Steller[16], Š. Štverák[3,17], P. Trávníček[8,17], and A. Vaivads[18]

[1] LESIA, Observatoire de Paris, Université PSL, CNRS, Sorbonne Université, Université de Paris, Paris, France
e-mail: arnaud.zaslavsky@obspm.fr
[2] Institute of Physics and Technology, Arctic University of Norway, Tromsø, Norway
[3] Institute of Atmospheric Physics of the Czech Academy of Sciences, Prague, Czech Republic
[4] Space Research Center, Polish Academy of Sciences, Warsaw, Poland
[5] Faculty of Mathematics and Physics, Charles University, Prague, Czech Republic
[6] CNES, 18 Avenue Edouard Belin, 31400 Toulouse, France
[7] Department of astronomy, Faculty of Mathematics, University of Belgrade, Serbia
[8] Space Sciences Laboratory, University of California, Berkeley, CA, USA
[9] Physics Department, University of California, Berkeley, CA, USA
[10] Swedish Institute of Space Physics, Uppsala, Sweden
[11] Radboud Radio Lab, Department of Astrophysics, Radboud University, Nijmegen, The Netherlands
[12] LPP, CNRS, Ecole Polytechnique, Sorbonne Université, Observatoire de Paris, Université Paris-Saclay, Palaiseau, Paris, France
[13] LPC2E, CNRS, 3A avenue de la Recherche Scientifique, Orléans, France
[14] Université d'Orléans, Orléans, France
[15] Technische Universität Dresden, Würzburger Str. 35, 01187 Dresden, Germany
[16] Space Research Institute, Austrian Academy of Sciences, Graz, Austria
[17] Astronomical Institute of the Czech Academy of Sciences, Prague, Czech Republic
[18] Space and Plasma Physics, School of Electrical Engineering and Computer Science, Royal Institute of Technology, Stockholm, Sweden

ABSTRACT

Context. Impacts of dust grains on spacecraft are known to produce typical impulsive signals in the voltage waveform recorded at the terminals of electric antennas. Such signals (as may be expected) are routinely detected by the Time Domain Sampler (TDS) system of the Radio and Plasma Waves (RPW) instrument on board Solar Orbiter.
Aims. We investigate the capabilities of RPW in terms of interplanetary dust studies and present the first analysis of dust impacts recorded by this instrument. Our purpose is to characterize the dust population observed in terms of size, flux, and velocity.
Methods. We briefly discuss previously developed models of voltage pulse generation after a dust impact onto a spacecraft and present the relevant technical parameters for Solar Orbiter RPW as a dust detector. Then we present the statistical analysis of the dust impacts recorded by RPW/TDS from April 20, 2020 to February 27, 2021 between 0.5 AU and 1 AU.
Results. The study of the dust impact rate along Solar Orbiter's orbit shows that the dust population studied presents a radial velocity component directed outward from the Sun. Its order of magnitude can be roughly estimated as $v_{r,\text{dust}} \simeq 50\,\text{km\,s}^{-1}$, which is consistent with the flux of impactors being dominated by β-meteoroids. We estimate the cumulative flux of these grains at 1 AU to be roughly $F_\beta \simeq 8 \times 10^{-5}\,\text{m}^{-2}\,\text{s}^{-1}$ for particles of a radius $r \gtrsim 100\,\text{nm}$. The power law index δ of the cumulative mass flux of the impactors is evaluated by two differents methods, namely: direct observations of voltage pulses and indirect effect on the impact rate dependency on the impact speed. Both methods give the following result: $\delta \simeq 0.3$–0.4.
Conclusions. Solar Orbiter RPW proves to be a suitable instrument for interplanetary dust studies, and the dust detection algorithm implemented in the TDS subsystem an efficient tool for fluxes estimation. These first results are promising for the continuation of the mission, in particular, for the in situ study of the inner Solar System dust cloud outside of the ecliptic plane, which Solar Orbiter will be the first spacecraft to explore.

Key words. instrumentation: detectors – methods: data analysis – meteorites, meteors, meteoroids – interplanetary medium

1. Introduction

In recent decades, radio and plasma wave instruments have demonstrated the ability to probe dust in different space environments. Voyager's plasma wave instrument (Gurnett et al. 1983) and planetary radio astronomy experiment (Aubier et al. 1983) both observed broadband signals that were interpreted as having been produced by dust impacts during the crossing of Saturn's E ring by Voyager 1 and G ring by Voyager 2. The plasma wave instrument, operating in dipole mode with a roughly

symmetrical configuration, observed smaller amplitude signals that the radio experiment, operated in monopole mode. The technique was used again along Voyager 2 orbit, with dust measurements at Uranus (Meyer-Vernet et al. 1986; Gurnett et al. 1987) and Neptune (Gurnett et al. 1991; Pedersen et al. 1991). Voyager measurements at the outer planets of the Solar System were followed up by others in space environments with an expected high dust flux, such as cometary trails with, for instance, VEGA 2's plasma wave instrument at Halley's comet (Oberc 1990).

From around the start of the year 2000, radio analyzers on board missions such as Wind (Bougeret et al. 1995), Cassini (Gurnett et al. 2004), or STEREO (Bougeret et al. 2008) recorded a large number of electric waveforms characteristic of dust impacts. The improvement in the technical performance of these radio detectors compared to the previous generation (the higher sampling frequency of the waveform analyzers in particular), along with the large number of examples available for study, has led to a better understanding of the mechanisms involved in the voltage pulse generation after a dust impact. Several recent studies have detailed the work of modeling and made comparisons to available data, such as works by Zaslavsky (2015) on STEREO, Meyer-Vernet et al. (2017), or Ye et al. (2019) on Cassini and Vaverka et al. (2019) on MMS. The paper by Mann et al. (2019) provides a complete summary of the works performed on various spacecraft, along with a prospect for the Parker Solar Probe and Solar Orbiter missions as well as a review of the voltage pulse mechanism in our present state of understanding. The paper by Lhotka et al. (2020) also presents a detailed analysis of spacecraft charging processes in various plasma environments and an application to dust impacts on MMS.

To summarize these models, voltage pulses result from the production of free electric charges by impact ionization after a grain of solid matter hits the spacecraft. These charges modify the spacecraft potential (and, depending on the impact location, the antennas) by way of two main effects: one being the perturbation of the electric current equilibrium between the spacecraft and the surrounding plasma due to the collection by the spacecraft of some of these free electric charges; the second being the perturbation of the spacecraft or the antenna potential by electrostatic influence from these free charges, that occurs when the impact plasma cloud is not neutral overall (which happens after some of the charges have been collected or have escaped from the vicinity of the spacecraft).

Over the years and thanks to these refinements in pulse modeling, radio analyzers have thus proven capable of providing robust estimates of dust fluxes in various mass ranges, varying from the nanometer to the micron. Examples of the successful use of this technique to derive dust fluxes include the detection of nanometer-sized dust with STEREO/WAVES (Meyer-Vernet et al. 2009b) and Cassini/RPWS (Meyer-Vernet et al. 2009a), measurements of the interstellar dust flux and direction at 1 AU by STEREO/WAVES (Zaslavsky et al. 2012) and Wind/WAVES (Malaspina et al. 2014), or measurements of the micron to ten microns sized dust density in the vicinity of Saturn by Cassini/RPWS (Ye et al. 2014, 2018).

The present paper, continuing on from these works, is devoted to the study of the dust impact data recorded by the Radio and Plasma Waves instrument and to the derivation of the interplanetary dust fluxes along Solar Orbiter's orbit. This is of particular importance since in situ measurements of interplanetary dust in the inner heliosphere, which are necessary to constrain and validate dust production models, are limited. Notably

there are only few data on the dust collision fragments that form in the inner solar system and then are ejected outward. Flux estimates for these dust grains, denoted as β-meteoroids, were made based on Helios observations (Zook & Berg 1975) and based on Ulysses observations (Wehry & Mann 1999). The dust collision evolution inside 1 AU were studied with model calculations having only few observational constrains (Mann et al. 2004).

Recently, the Parker Solar Probe (PSP) has been operating the FIELDS instrument (Bale et al. 2016), which provides observations of dust impacts. The PSP dust observations have been presented in a number of recent works (Page et al. 2020; Szalay et al. 2020; Malaspina et al. 2020). These observations provide a number of interesting results on dust fluxes in the close vicinity of the Sun. In the context of this paper, recent works on the second orbit of PSP with dust measurements between ca. 0.16 and 0.6 AU are of interest. Szalay et al. (2020) showed that the observations during the second solar encounter could be explained through particles that form as collision fragments near the Sun and then are ejected by the radiation pressure force. Mann & Czechowski (2021) showed that the same fluxes could be explained with a model that combines the collisional production of dust particles and their dynamics influenced by gravity, radiation pressure, and Lorentz force; the latter was found to have only a small effect on the particles that were observed with PSP during the second orbit.

In this paper, we first present and discuss the waveform data recorded by the instrument and the specificities of Solar Orbiter as a dust detector in Sect. 2. Then, in Sect. 3, we focus on the statistical study of the time repartition and of the voltage amplitudes of the hits recorded. Finally, in a last section, we build on this statistical study to determine the flux of the dust population observed we and compare our results to those obtained by other missions as well as to the theoretical predictions in the field.

2. Dust measurements with RPW

The RPW instrument on board Solar Orbiter (see a complete description in Maksimovic et al. (2020) is designed to measure and analyze the electric field fluctuations from near-DC to 16 MHz and magnetic fluctuations from several Hz to 0.5 MHz. In this article we are mainly interested by the electric waveforms provided by the time domain sampler (TDS) subsystem of RPW. In particular, TDS provides digitized snapshots of the voltage measured between the terminals of two of the spacecraft electric antennas (dipole mode) or between one the spacecraft electric antennas and the spacecraft ground (monopole mode). The waveforms used in this article were sampled at a rate of 262.1 kHz, after being processed by an analog high-pass filter with a cutoff around 100 Hz.

Figure 1 shows examples of impulsive signals recorded by TDS that we interpret as having been due to dust impacts. The examples shown here were selected from the so-called triggered snapshots that were flagged by the on-board detection algorithm as probable dust impacts (see Sect. 3.1 for the description of the algorithm).

The left column shows events recorded in SE1 mode (for which TDS samples three monopoles: V1, V2, and V3), whereas the right column shows events recorded in XLD1 mode (two channels measure dipole voltages V1–V3 and V2–V1, and the third channel is linked to the monopole V2). Each channel (CH1, CH2, and CH3) represents voltage difference measured between individual antennas (V1, V2, and V3) for dipoles or between one antenna and the spacecraft body (SC) for monopoles. It should be noted that presented data are not corrected for transfer
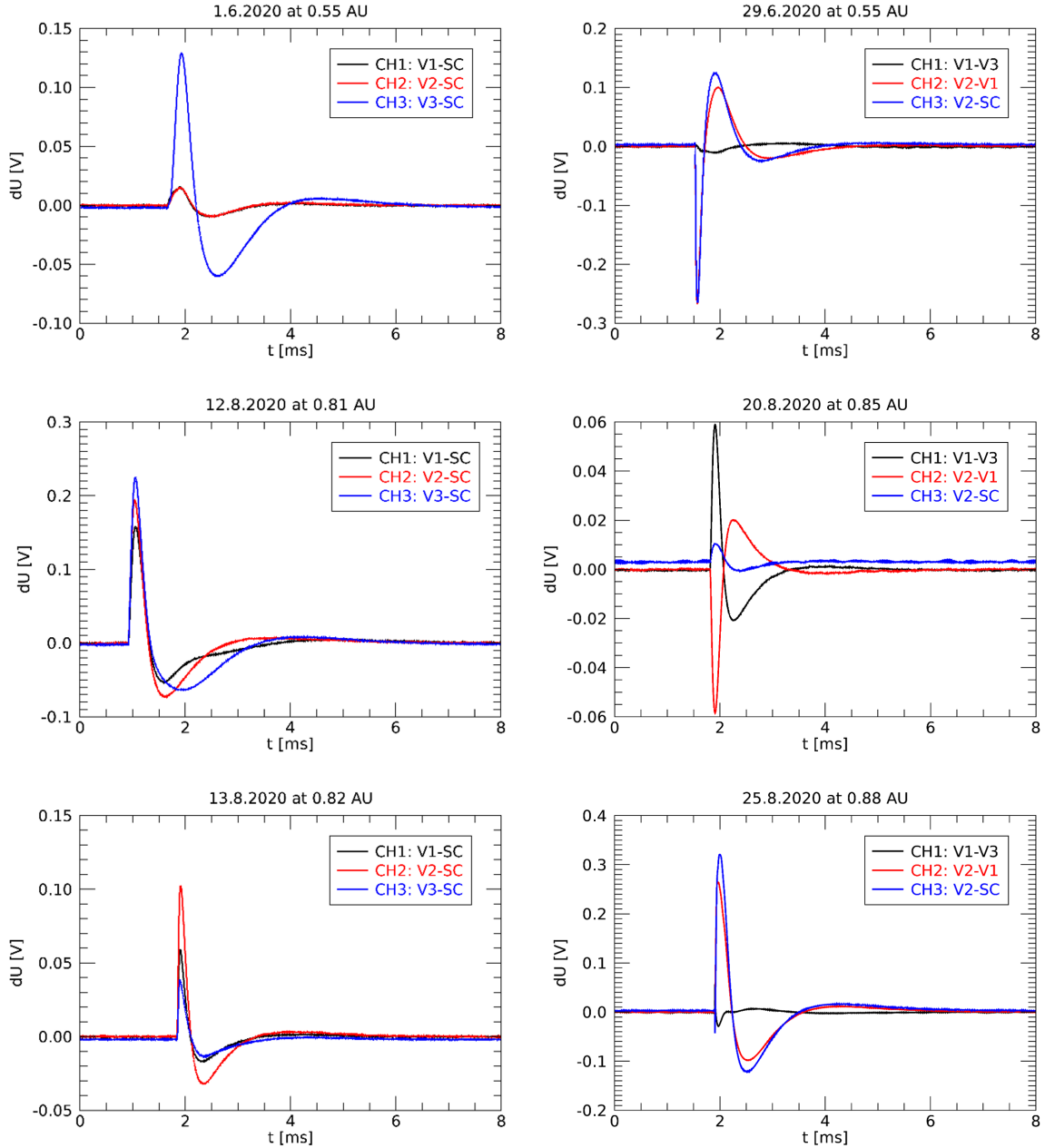
Fig. 1. Six examples of TDS snapshots showing impulsive signals interpreted as due to dust impacts onto the spacecraft. Signals recorded on the three different channels are represented in different colors. The *left column* shows signals recorded in monopole mode (SE1 mode), whereas the *right column* shows signals recorded in dipole in the two first channels and monopole in the third one (XLD1 mode).

function (the existence of "overshoots" in these data is probably artificial). Examples shown on the lower panels of left column are typical of signals detected at the terminal of a monopole antenna by electron collection, similar to the one detected by STEREO/WAVES, for instance.

2.1. Voltage pulses and their link to mass and velocity of impacting dust grains

Before discussing these images, we recall the mechanism through which voltage pulses are thought to be produced. First, a dust grain impacts the spacecraft body and expels from it some material, part of which is ionized. The amount of free electric charge $Q > 0$ in the (overall neutral) cloud of expelled material is a function of the mass m of the impacting grain and of

the relative velocity, v, of the impactor with respect to the target. The measurement of Q after an impact in a dedicated collector, together with an independent measurement of v in order to deduce the mass, m, of the impactor, is the general operating principle of dust impact ionization detectors (Auer 2001). Experiments show that the function $Q(m, v)$ follows the general scaling:

$$Q(m, v) \simeq A m v^{\alpha}, \qquad (1)$$

where m is expressed in kg and v in km s^{-1}. Since the parameters A and α quite strongly depends on the impacted material (Collette et al. 2014), it is of course preferable for the charge yield of the collector material as a function of m and v to be measured on ground. In the absence, for the moment, of such measurements for Solar Orbiter's surface material, we have to

use approximate values for A and α. Dietzel et al. (1973) as well as McBride & McDonnell (1999) suggest the use of $A \sim 1$ and $\alpha \sim 3.5$, which is a rather high charge yield (we discuss this point when evaluating the size of the impactors in the last section of this article).

In the absence of a dedicated and well calibrated collector, but in the presence of electric antennas operated in monopole mode, we can still quite reliably deduce the amount of charge, Q, released during an impact thanks to the different dynamics of the electrons and the heavier positive charges in the expelled cloud of ionized matter. The dynamics of the light electrons quickly decouple from the one of the heavier positively charged matter (Pantellini et al. 2012). The electrons are quickly collected by (or repelled away from) the spacecraft, letting positive charges remain unscreened in the vicinity of the spacecraft. For a positively charged spacecraft, it can be shown that the combination of the effect of quick electron collection and ions getting repelled away from the spacecraft will produce a maximal change in the spacecraft ground potential equal, to a good approximation, to $\delta\varphi_{sc} \simeq -Q/C_{sc}$ (here C_{sc} is the spacecraft's body capacitance).

In monopole mode, the signal recorded is $V(t) = \Gamma(\varphi_{ant}(t) - \varphi_{sc}(t))$, where φ_{ant} is the monopole antenna potential and Γ a transfer function accounting for the (mostly capacitive) coupling between the antenna and the spacecraft body: $\Gamma = C_{ant}/(C_{ant} + C_{stray})$; in this formula, C_{ant} is the antenna's capacitance and C_{stray} accounts for the capacitive coupling through the preamplifier, the mechanical base of antenna, and various wires. If we assumes that φ_{ant} is roughly constant during the process, then the charge, Q, produced by impact ionization is quite simply linked to the peak of the voltage pulse measured in monopole mode by:

$$Q(m, v) \simeq \frac{C_{sc} V_{peak}}{\Gamma}. \tag{2}$$

Therefore, the use of formulas (1) and (2) makes it possible to link the properties of the impacting grain to those of the measured voltage signal.

We can see, in light of these explanations, why monopole measurements are favorable to dust detection. The main change induced by the impact occurs in the spacecraft ground potential, while antennas potentials stay roughly constant. Dipole measurements, which measure the variation of an antenna's potential relative to another antenna, are therefore quite insensitive to this process. Still, signals are quite frequently observed in dipole mode, as can be seen on the right panels of Fig. 1.

For a signal to be observed in dipole mode, it must produce a pulse of substantially larger amplitude on a particular antenna than on the two others. An example of such a signal recorded on monopole mode can be seen on the top left panel of Fig. 1, with a peak amplitude on monopole V3 that is much larger than on V1 and V2. One interpretation for these signals is that the impact location may be close to a particular antenna, the potential of which would in turn undergo a much stronger variation under electrostatic influence from the positively charged cloud than the other monopoles. The derivation of the charge Q from dipole measurements is therefore more complicated, since the amplitude of the voltage pulse not only depends on Q but also on the position of the impact with respect to the monopoles. An order of magnitude of such a signal is (Meyer-Vernet et al. 2014) $V_{peak} \sim \Gamma Q/(4\pi\epsilon_0 L_{ant})$, assuming only one arm of the dipole sees the whole unscreened charge Q, so that the charge in the cloud can be linked to the peak voltage in dipole mode by:

$$Q(m, v) \sim \frac{4\pi\epsilon_0 L_{ant} V_{peak,dipole}}{\Gamma}, \tag{3}$$

where L_{ant} is the length of an antenna. Importantly, it should be noted that unlike the signal observed in monopole mode (for the at least two monopoles showing similar peak voltages), which is quite accurately linked to the released charge Q by Eq. (2) – in Eq. (3), only a rough order of magnitude is provided, since the voltage produced will, in fact, be very dependent on the location of the impact. An impact occurring at equidistance from two arms of the dipole, for instance, would produce a very small signal in dipole mode, even for an important release of charge; whereas an impact cloud expanding in the close vicinity of a particular dipole arm could produce a signal quite stronger than the estimation above.

On the right column of Fig. 1 (XLD1 mode), we show a few examples of events where the signal is mainly registered by a single antenna – hence, not mainly produced by the variation of the spacecraft potential, but rather by electrostatic influence on a particular antenna. The impact must be close to antenna V2 on cases shown on top and bottom right panels (which show identical pulses in channels CH2 and CH3) and to antenna V1 in the middle right panel (inverted pulses in channels CH1 and CH2).

2.2. Parameters for Solar Orbiter as a dust detector

Now that the main principles through which we interpret voltage pulses after a dust impact have been established, we describe in this part their application to the specific case of Solar Orbiter.

Solar Orbiter orbits the Sun along a series of roughly elliptical orbits, with a minimum perihelion of 0.28 AU and a maximum inclination with respect to the ecliptic above 30°. A description of the mission and its science objectives can be found in Müller et al. (2020).

The electric sensors of RPW are three stacer monopoles of a length, $L = 6.5$ m, and radius, $a = 0.015$ m, mounted on 1 m rigid booms to separate them from the spacecraft body, electrically biased in order to reduce variations of their potential with respect to the plasma at low frequencies (Maksimovic et al. 2020). They are in the same plane and make angles of roughly 120° with each other. The disposition of the antennas with respect to the spacecraft body is shown on Fig. 2. We note, in relation to the previous discussion on the generation of electric pulses after a dust impact, that the three monopoles are mounted on opposite sides of the spacecraft quite far away from each other (similarly to the case of spacecraft like WIND, MMS or Parker Solar Probe, but unlike the cases of Voyager, Cassini or STEREO), which implies that the effect of electrostatic influence can be very different from an antenna to the others and explains why signals are frequently observed in dipole mode.

The capacitance associated with each monopole base has been measured on ground, with the values found as follows: $C_b = 76.3 \pm 4$ pF for the monopole V1, $C_b = 78.9 \pm 3$ pF for V2, and $C_b = 76.2 \pm 2.7$ pF for V3. The stray capacitance is to a good approximation the sum of this base capacitance and of the preamplifier capacitance C_{amp}, which, when both preamplifiers are ON, is $C_{amp} = 29$ pF. Since the base capacitances are equal within measurement uncertainties, we shall use for the three monopoles the same value of the stray capacitance, $C_{stray} \simeq 77 + 29 \simeq 108$ pF.

Assuming the monopoles are in a vacuum and considering the spacecraft as an infinite ground plane, we find the capacitance of a monopole $C_{ant} = 2\pi\epsilon_0 L/(\ln L/a - 1) \simeq 71$ pF. The presence of solar wind's plasma, however, at the frequencies we are interested in (i.e., smaller than the local plasma frequency), decrease the capacitance to values $C_{ant} \sim 2\pi\epsilon_0 L/(\ln L_D/a)$,
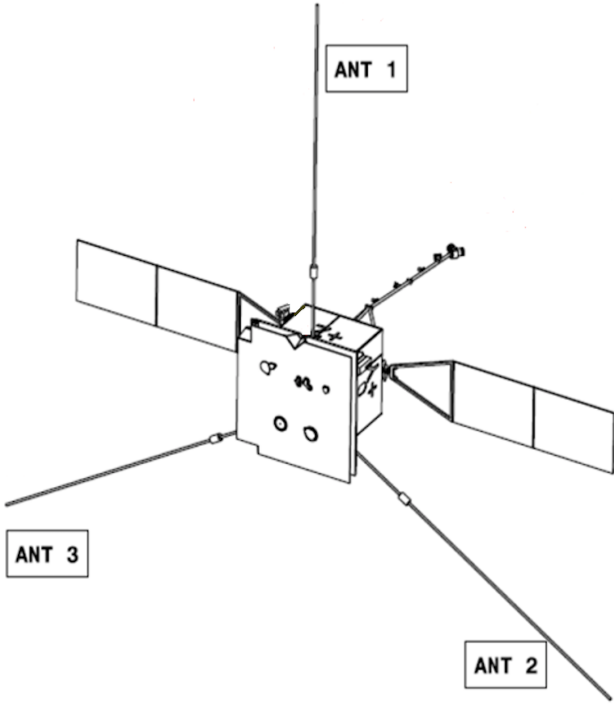
Fig. 2. Geometrical configuration of RPW's electric sensors (labelled ANT1, 2, and 3), heat shield and deployed solar panels with respect to the spacecraft body.

where L_D is the local Debye length (Meyer-Vernet & Perche 1989). With the Debye length varying in a range $\sim 3-10$ m along the spacecraft's orbit, we obtain $C_{ant} \sim 55-70$ pF (the capacitance increasing when going closer to the Sun). Using these values, the attenuation factor can be evaluated as $\Gamma = C_{ant}/(C_{ant} + C_{stray}) \simeq 0.34-0.39$.

The isopotential surface of the spacecraft's body has been evaluated from the Solar Orbiter numerical model. This value can be estimated from 25.11 m^2, taking into account only the surface of the five satellite walls plus the heat shield, up to 31.43 m^2 when we consider the envelope including the overall spacecraft. The backside of the solar panels (6 panels of 2.1 m $\times$ 1.2 m) are isopotential to the spacecraft body (unlike their frontside). The additional surface is then $S_{panels} = 15.12$ m^2 (taking only one side into account). Therefore, we can evaluate the area of the interface between the plasma and the isopotential parts of the spacecraft to be $S_{sc} \simeq S_{body} + S_{panels} \simeq 43.4 \pm 3.2$ m^2. The capacitance of a conductor of such a complex shape is difficult to estimate. An analytical order of magnitude estimation is given by the vacuum capacitance of the sphere of equivalent surface $C_{sc} \sim \epsilon_0 \sqrt{4\pi S_{sc}} \sim 210$ pF. A more refined modeling can be obtained through numerical simulations of the spacecraft charging. Such simulations have been recently performed for Solar Orbiter at ESA, and provided us with a value of the free space capacitance equal to $C_{sc} \simeq 355$ pF (G. Déprez, priv. comm.). This is the value we adopt in this paper, although it is probably a bit of an underestimation since it does not take into account plasma sheath effects.

The surface, S_{sc}, discussed above would approximately correspond to the dust collecting area if the dust population velocity distribution was isotropic in the frame of the spacecraft. As we see in the following, it is probably not the case for the majority of the dust observed by Solar Orbiter, the velocity of which is mostly directed toward the heat shield. Therefore, the

dust-collecting area to consider is strongly reduced compared to S_{sc}, and it is rather of the order of the heat shield's surface $S_{col} \simeq 2.5$ m $\times$ 3.1 m $\simeq 8$ m^2. We do not include the solar panels in the collecting surfaces, since their front side is electrically isolated from the rest of the spacecraft. Of course, an impact to a solar panel can produce a charge that could be collected by other conductive parts of the spacecraft. We neglect this effect in this study and recognize that our estimate of S_{col} is a low estimate of the actual collecting area.

Finally, we briefly discuss the relaxation time of perturbations of Solar Orbiter's floating potential as follows. Linear theory gives $\tau_{sc} \simeq C_{sc} T_{ph}/I_e$, where $I_e = e n_e v_e S_{sc}/4$ is the electron current onto the spacecraft isopotential surface (e is the electron charge, n_e the local electron density and $v_e = \sqrt{8kT_e/(\pi m_e)}$ is the average electron velocity, with T_e the local electron temperature, and m_e the electron mass). $T_{ph} \sim 3$ V is the temperature of the photoelectrons ejected from the spacecraft body expressed in electric potential unit. The assumption underlying this formula is that photoelectron current from the spacecraft is dominating over solar wind's electron current, the spacecraft potential being as a consequence positive (assumption justified pretty much all along Solar Orbiter's trajectory, setting apart short periods in the shadow of Venus). Assuming a typical variation of electron parameters in the solar wind (see e.g., Issautier et al. 1998; Stverak et al. 2015) one obtains for the relaxation time $\tau_{sc} \sim 60$ μs at 1 AU and ~ 15 μs at 0.5 AU. These numbers are significant in that the estimation of the peak amplitude of the pulses observed in monopole mode $V_{peak} \sim -Q/C_{sc}$ is strictly valid only in the case were the rise time of the pulse τ_{rise} (controlled by the positive charges dynamics in the vicinity of the spacecraft) is not large compared to the relaxation time τ_{sc} of spacecraft electric potential perturbations. In the opposite case, where τ_{sc} is small compared to τ_{rise}, the amplitude of the signal is reduced by a factor of the order of $\tau_{sc}/\tau_{rise} \ll 1$ (Zaslavsky 2015). This effect will not be taken into account in this article. A more precise study of the waveforms – which requires a very careful calibration – will be the subject of forthcoming studies and, among other things, will make it possible to quantify this effect.

3. Statistical analysis of dust impacts

3.1. Impact rate and estimation of the impactors radial velocity

In this section, we present the results of the analysis of the impacts voltage pulses recorded along Solar Orbiter's orbit from April 20, 2020 to February 27, 2021. For this purpose, we mainly use the data provided by the on-board analysis of TDS samples through an algorithm that flags a snapshot as being produced by a dust impact if it contains a signal that is sufficiently impulsive. This dust detection algorithm has been working with constant settings from April 20, 2020, hence the date at which we start our analysis.

The detection algorithm, described in detail by Soucek et al. (2021), works as follows: the instrument takes one waveform snapshot of 16384 samples every second. Each snapshot exceeding a minimum amplitude threshold is processed by the TDS on-board software to calculate the maximum and median amplitude and calculate the Fourier spectrum from the snapshot. From this spectrum, the software determines the frequency corresponding to the largest spectral peak and the FWHM (full width at half maximum) bandwidth of this peak. The algorithm then classifies the observed snapshots based on comparing the ratio R between
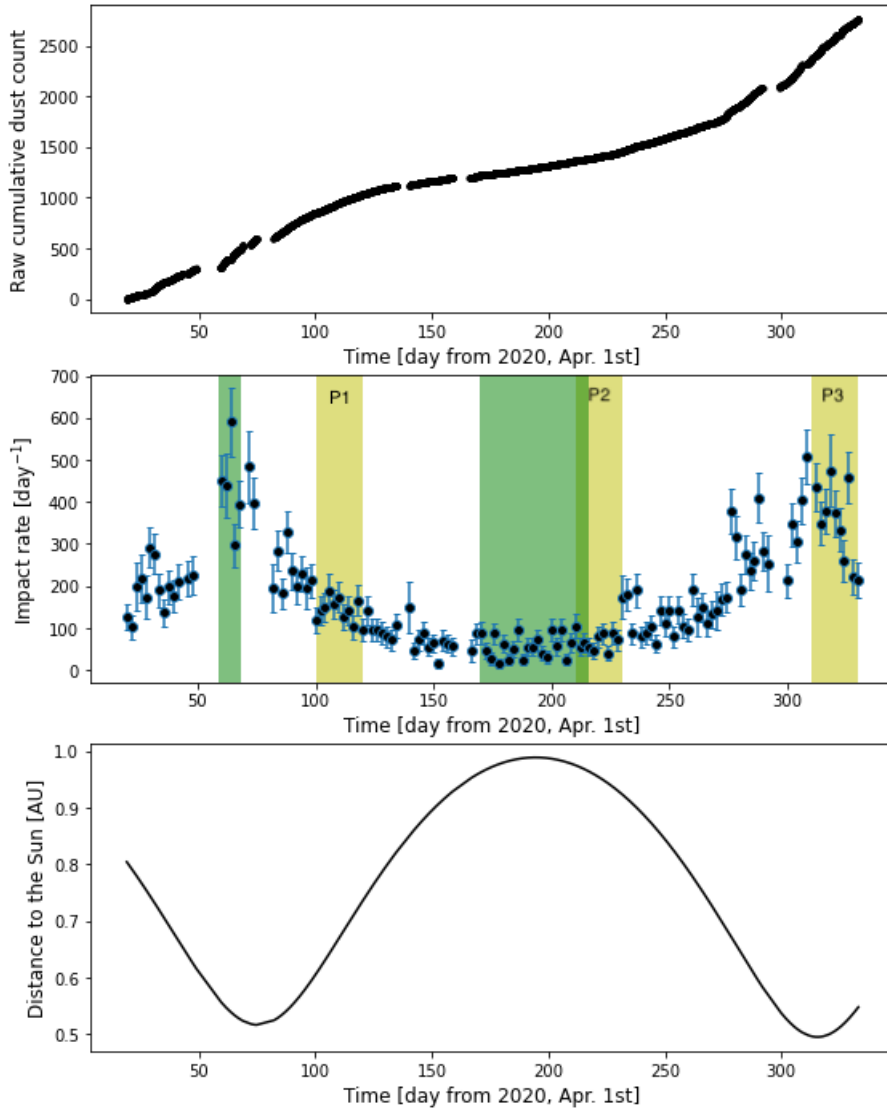
Fig. 3. Impact rates recorded by RPW/TDS. *Upper panel*: raw cumulative dust count as a function of time since April 1, 2020. By raw, it is meant that it is the integer number of impacts provided by the detection algorithm, uncorrected for the instrument's duty cycle. *Middle panel*: impact rate as a function of time since April 1, 2020. Each point corresponds to a two-day time interval. The error bars are computed from $\sqrt{N}/\Delta t$, where Δt is the time covered by TDS measurements on the two days considered, and N the number of impacts during these two days. The yellow areas correspond to time periods P1, P2, and P3 on which the number of occurrence distributions of Fig. 5 have been computed. The green areas correspond to times periods on which the amplitude distributions shown on the right panel of Fig. 6 have been computed. *Lower panel*: distance from the spacecraft to the Sun in astronomical units, as a function of time since April 1, 2020.

the maximum and median absolute value in the snapshot and the spectral bandwidth to predefined thresholds. Specifically, snapshots with large R and large spectral bandwidth are identified as dust impacts. In this way, the algorithm allows us to identify even relatively small amplitude dust spikes.

The outcome of this detection is then used to select the "best" wave and dust snapshots to be transmitted to the ground and also to build statistical data products. The key data product used here is the number of detected dust impacts in a 16 second interval which is transmitted in short statistical data packet every 16 seconds. Due to the fact that the detection algorithm only examines one snapshot of 62 ms every second, the reported dust counts are much lower than the actual number of dust impacts, but the number of detected dust impacts can be considered directly proportional to the actual number of dust impacts.

Since some impulsive signals may be erroneously taken for dust (e.g., solitary waves, Vaverka et al. 2018, and various spacecraft generated effects), the dataset has been cleaned by removing all periods of fast sampling at 524 kHz, all measurements influenced by active sweeps performed by the BIAS subsystem of RPW and several days (in particular during commissioning), where TDS was configured to non-standard operation modes. We also removed the Venus flyby interval on December 27, 2020 when TDS detected numerous solitary waves and counted them as dust impacts.

We considered this TDS dust data product on a timescale of 1h, and computed the impact rate for each hour by dividing the number of snapshots flagged as dust by the total number of snapshots recorded during this hour multiplied by the duration of one snapshot ($\Delta t = 62$ ms): impact rate $R = N_{\text{impact}}/(N_{\text{snapshots}}\Delta t)$.

Figure 3 shows the evolution of the impact rates with time. The upper panel shows the raw (i.e., not corrected for the duty cycle) cumulative impact number, showing that the total number of impacts detected by the algorithm during the period of our study is 2758. We can also notice several small data gaps corresponding to periods during which the instrument is switched off.

The middle panel shows the impact rate as a function of time, showing an increase in the flux with decreasing distance to the Sun, which is a general behavior that is in agreement with remote and in situ measurements from Helios (Leinert et al. 1981) or Parker Solar Probe (Szalay et al. 2020; Page et al. 2020).

Figure 4 illustrates the evolution of the impact rate with distance from the Sun. On the left panel of this figure, the impact rates measured when the spacecraft is going toward the Sun (spacecraft radial velocity $v_{r,\text{sc}} < 0$) are separated from the ones
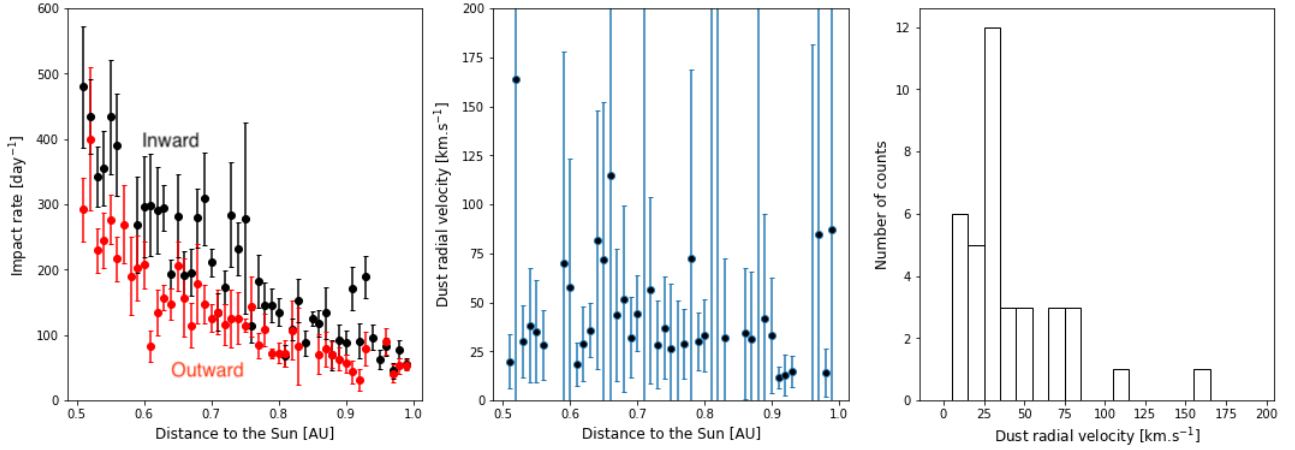
Fig. 4. Estimation of the impactors radial velocity from the impact rates. *Left panel*: impact rate as a function of radial distance. The black points show fluxes recorded when the spacecraft is moving toward the Sun, the red points when moving outward from the Sun. Each point is computed by averaging the impact rate data on 50 distance intervals linearly spaced between 0.5 and 1 AU. Error bars show one standard deviation error on the computation of the mean. *Middle panel*: radial component of the dust velocity, $V_{r,\text{dust}}$, computed from Eq. (4). Error bars are computed by propagating errors on the impact rates shown on the left panel. *Right panel*: histogram of the obtained values of $V_{r,\text{dust}}$.

measured when the spacecraft is going outward ($v_{r,\text{sc}} > 0$). It can be seen that the impact rate is in average slightly larger when $v_{r,\text{sc}} < 0$ than when $v_{r,\text{sc}} > 0$. This is consistent with the dust population measured having a mean velocity directed outward from the Sun.

One can use this difference in the impact rates to obtain a first estimation of the radial velocity $v_{r,\text{dust}}$ of the dust population: assuming that the velocity and fluxes are function of the distance to the Sun only (neglecting all time variability) and neglecting – for an order of magnitude estimation – the effect of tangential velocities, it can easily be shown that

$$v_{r,\text{dust}} \sim \frac{R_{\text{in}} + R_{\text{out}}}{R_{\text{in}} - R_{\text{out}}} \left| v_{r,\text{sc}} \right|, \tag{4}$$

where $v_{r,\text{sc}}$ is the radial velocity of the spacecraft, R_{in} the impact rate when the spacecraft is going toward the Sun, and R_{out} when going outward. The middle panel of Fig. 4 shows the result of applying formula (4) with the impact rates R_{in} and R_{out} shown on the left panel. The error bars are very large but the mean value obtained is reasonably constant with radial distance. The right panel shows a histogram of the values of $v_{r,\text{dust}}$ obtained, with a peak value at $v_{r,\text{dust}} = 30 \, \text{km} \, \text{s}^{-1}$ and an averaged value around $50 \, \text{km} \, \text{s}^{-1}$. The large error bars, the variations of the measured fluxes, and the use of a simple model let us only hope for an order of magnitude estimation of course, but this value is consistent with expectations for small particles on hyperbolic orbits and with the results from the numerical simulations of particles dynamics discussed in the last section of this paper.

Let us note that this estimate of a $50 \, \text{km} \, \text{s}^{-1}$ radial velocity of the impactor – a velocity comparable to the spacecraft orbital speed – implies that the impacts do not actually occur only on the heat shield (as was assumed in the previous section), but also on the sides of the spacecraft. The effective collecting area must then vary along the spacecraft trajectory. This effect, that may produce errors of the order of 10–20% on the fluxes estimations, will not be accounted for in the present paper. We will, as discussed in the previous section, keep in mind that the value of the collecting area $S_{\text{col}} = 8 \, \text{m}^2$ used in this work is somehow underestimated. It should still provide a quite robust order of magnitude.

Figure 5 shows the distribution of the number of impacts recorded during time intervals of 6 hours, for three different values of the impact rate. The three intervals on which these number of occurrence distributions have been computed are highlighted in yellow on Fig. 3. They correspond to distances to the Sun ~0.7 AU (left panel, mean impact rate ~140 day^{-1}), ~1 AU (middle panel, mean impact rate ~50 day^{-1}), and ~0.5 AU (right panel, mean impact rate ~350 day^{-1}). The comparison with Poisson distribution, over-plotted in red, shows a very good agreement consistent with the data being due to independent events at roughly constant rates, as expected for interplanetary dust impacts.

3.2. Peak voltages distribution and power-law index of the impactor's cumulative mass flux

In order to further characterize the population of dust grains impacting Solar Orbiter, we look at the distribution of voltages measured in monopole mode. To this purpose we look at the snapshots dataset, which does not include all of the dust impacts detected by the onboard algorithm on which the results of the previous section are based. We assume that the subset of triggered snapshots is a random sample from the ensemble of all the recorded dust impact signals and, therefore, that both share the same statistical properties – or since this can't be exactly true, we assume that selection bias are small and do not impact importantly the voltage amplitude statistics.

Measurements in monopole mode, as discussed in Sect. 2, are required in order to properly (as unambiguously as possible) link the peak amplitude of the pulse to the charge generated by impact ionization. Unfortunately, they are, for monopoles V1 and V3, only active during a small fraction of the mission time, that is, mainly during two periods: from May 30 to June 8 (185 dust snapshots telemetered) and from July 27 to August 13 (103 dust snapshots). Matters are different for monopole V2, which is quite routinely operated with 934 dust snapshots telemetered from April 1 to November 1 of 2020. Therefore, the particular focus is set on monopole V2 in the following.

Figure 6 shows the normalized distributions of peak voltage associated with dust impacts for different monopoles and different time periods. We can see that the peak voltage distribution has a power-law behavior. The left panel shows distributions computed on the whole period between April 1 - Nov. 31,
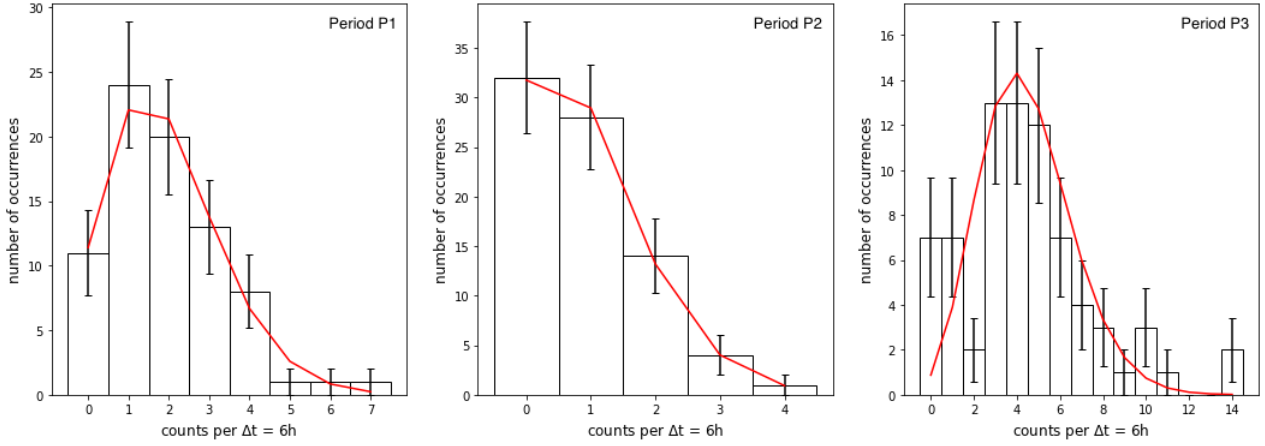
Fig. 5. Distribution of number of impacts per time intervals of 6 hours, for three different periods of time corresponding to different mean impact rates. The red curve shows the Poisson distribution calculated from the mean impact rate observed in each of these periods of time. Errorbars on the histograms values are $\sqrt{N_{\text{bin}}}$, with N_{bin} the number of counts in the histogram bin.

with different colors corresponding to peak voltages at the terminals of different monopoles. We can see that voltage distributions are similar on all monopoles – which is to be expected since in average all monopoles should react in the same manner to dust impacts. The results of least-square fitting these histograms with power laws is presented in Table 1, where it can be seen that power-law exponents are, within the uncertainties, equal from a monopole to another, around −4/3.

The middle panel of Fig. 6 compares the peak amplitude recorded on monopole V2 at different distances from the Sun. The limited number of impacts on which such a comparison can be made imply quite important uncertainties on the slopes of the distribution. The two last lines of Table 1 show the results of linear fitting for these distributions, showing a slope that is a bit steeper at the perihelion than at the aphelion. This difference being within the uncertainties, it is hard to draw a conclusion based on this result and it is sensible to wait for more statistics to see whether this trend is confirmed.

The right panel of Fig. 6 shows the distributions of all impacts recorded on monopole V2 on the whole time of our voltage amplitude analysis, namely, from April 1 to November 31, 2020, along with the corresponding power-law least-square fit, with index −1.34 ± 0.07.

From these observations it seems reasonable to approximate the rate of observation of signals having peak voltages between V_{peak} and $V_{\text{peak}} + dV_{\text{peak}}$ by $dR = g(V_{\text{peak}})dV_{\text{peak}}$, with

$$g(V_{\text{peak}}) = g(V_0) \left(\frac{V_{\text{peak}}}{V_0} \right)^{-a}, \tag{5}$$

where $a \simeq 1.34$ and V_0 an arbitrary voltage in the range where the power-law behavior applies.

An interesting result, of course, would be to deduce from these data information about the mass distribution of the impacting dust particles. We have seen in Sect. 2.1 that the released charge, Q, and, hence, the peak voltage, V_{peak}, is linked to the mass, but also to the velocity of the impacting particle, and we do not have an independent measurement of the latter for each of the impacts. Therefore, we can only make inferences on the mass distribution by assuming the existence of a relationship, $v(m)$, between the mass of the particle and its velocity with respect to the spacecraft. If such a relationship exists, then the function $V_{\text{peak}}(m, v)$ becomes a function of m only and – under the assumption that two different values of m cannot produce a peak

voltage of the same amplitude; that is, the function $V_{\text{peak}}(m)$ is bijective on the observed mass interval – the mass distribution of the impactors $f(m)$ can be directly linked to the measured distribution $g(V_{\text{peak}})$ by:

$$f(m) = g(V_{\text{peak}}) \left| \frac{dV_{\text{peak}}}{dm} \right|. \tag{6}$$

For a first-order estimation, one could assume that the impact velocity is independent of the mass on the given mass range. Then, according to Eqs. (1) and (2):

$$V_{\text{peak}} \simeq \frac{\Gamma}{C_{\text{sc}}} A m v^\alpha \tag{7}$$

is a linear function of m, and the mass distribution trivially has the same power-law shape than the distribution of voltage peaks. The cumulative mass flux of particles of mass larger than m onto the spacecraft (defined as $F(m) = \int_m^{+\infty} f(m')dm'$) would then be given by:

$$F(m) = F(m_0) \left(\frac{m}{m_0} \right)^{-\delta}, \tag{8}$$

where $\delta = a - 1 \simeq 0.34$ and $F(m_0)$ is the cumulative flux of particles of mass larger than m_0 (which may depend on the distance to the Sun).

Let us note that this estimation of the power-law index δ of the cumulative mass flux in the observed mass range must likely be an underestimation, since (if the velocity is an increasing function of m, which is probably the case in the observed mass range, see next section), $f(m)$ will decrease with a steeper slope than $g(V_{\text{peak}})$. This can easily be seen from Eq. (6), taking, for instance, $V_{\text{peak}} \propto m^{1+\varepsilon}$ with $\varepsilon > 0$. We would then obtain for $f(m)$ a power law index $a + (a - 1)\varepsilon$, which is always larger than a (if $a > 1$ which is the case here). Therefore, even without any precise knowledge of the function $v(m)$, but under the assumption that this is an increasing function of m in the observed mass interval, it is possible to derive from these observations of peak voltages a lower bound for the power law index of the cumulative mass flux $\delta \gtrsim 0.34$.

To conclude this section, we note that a more detailed derivation of the mass distribution of the particles could be obtained from these measurements by computing the function $v(m)$ from
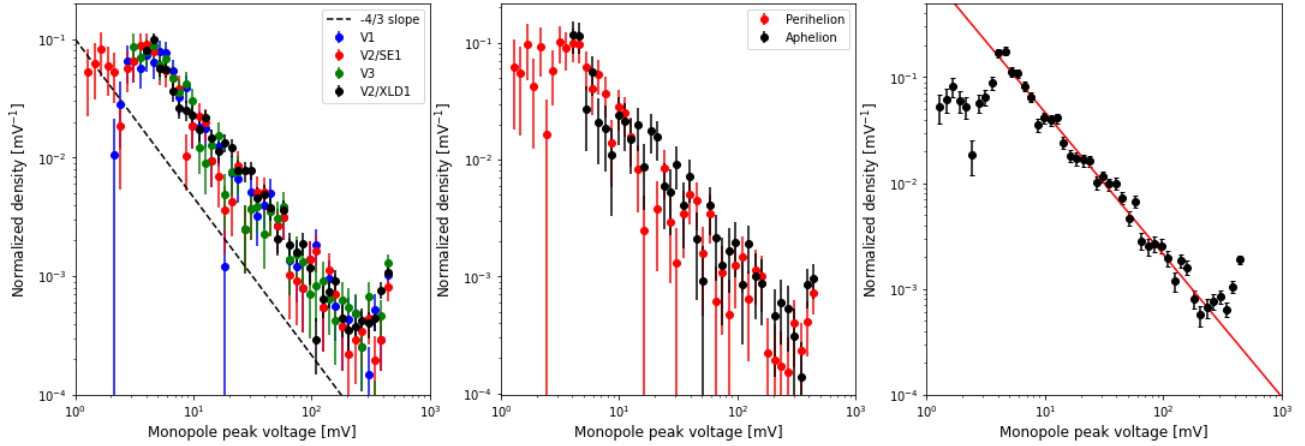
Fig. 6. Normalized density (i.e., number of dust detected per unit voltage interval) of voltage peaks in monopole mode. *Left panel*: distribution of the voltage peaks on all monopoles from April 1 to Nov. 30, 2020. Different colors accounts for different monopoles: V1 (blue), V2/SE1 (red), V3 (green), V2/XLD1 (black). *Middle panel*: distribution of peak amplitudes on monopole V2 during two different periods (highlighted in green in Fig. 3). Red points correspond to the high impact rate period close to the perihelion (May 13 – June 8), black points to the low impact rate period around the aphelion (Sep 17 – Nov 3). *Right panel*: result of the least square fitting of all the data recorded on monopole V2 from April 1 to Nov. 30, 2020. The slope of the red curve is -1.34 ± 0.07. In all these figures, error bars are computed from $\sqrt{N_{\mathrm{bin}}}/(\Delta V_{\mathrm{bin}} N_{\mathrm{tot}})$, where N_{bin} is the number of counts in the bin, ΔV_{bin} the bin width in mV, and N_{tot} the total number of events from which the histogram is computed.

Table 1. Power law indices of the peak voltage distributions.

Monopole	Time interval	Number of events	Power-law index
V1 (SE1 mode)	Apr. 1–Nov. 31	328	-1.34 ± 0.14
V2 (SE1 mode)	Apr. 1–Nov. 31	328	-1.34 ± 0.14
V2 (XLD1 mode)	Apr. 1–Nov. 31	934	-1.37 ± 0.10
V3 (SE1 mode)	Apr. 1–Nov. 31	328	-1.36 ± 0.11
V2 (SE1 mode)	May 30–Jun. 8 (Perihelion)	185	-1.37 ± 0.19
V2 (XLD1 mode)	Sep. 17–Nov. 2 (Aphelion)	161	-1.20 ± 0.17
V2 (SE1 and XLD1 modes)	Apr. 1–Nov. 31	1262	-1.34 ± 0.07

Notes. The uncertainties show 95% confidence interval on the linear regression coefficient.

numerical simulations, with proper assumptions for the initial conditions and dust β parameter. Since this function may depend on the distance from the Sun (which may explain the possible change of the power law index of the voltage distributions from perihelion to aphelion), this study may also require some time to accumulate more statistics and be able to construct not too noisy distributions of voltages at different distances from the Sun. Such a work is beyond the scope of these first results, but it offers an interesting perspective for a future study.

4. Estimation of the β-meteoroids flux and comparison to models and results from other missions

We now compare the observed impact rates to a dust flux model that bases on a number of assumptions. The existence of dust in the inner Solar System can be inferred from the brightness of the Zodiacal light and the F-corona which show that dust in the approximate 1–100 micrometer size range forms a cloud with overall cylindrical symmetry about an axis through the center of the Sun, perpendicular to the ecliptic (cf. Mann et al. 2014). The size distribution at 1 AU is estimated from a number of different in situ observations and described in the interplanetary dust flux model (Gruen et al. 1985). The majority of dust grains form by fragmentation from comets, asteroids and their fragment grains.

The larger grains are in bound orbit about the sun; as a result of the Poynting-Robertson effect, they lose orbital energy and angular momentum and fall into the Sun after time scales of the order of 10^5 years. However, the majority of the Zodiacal dust is within shorter time fragmented by collision with other dust grains, the smaller fragments leave the inner Solar System and collision production from larger grains is needed to replenish the dust cloud (Mann et al. 2004). The dust with sizes that are smaller than roughly a micrometer experiences a larger radiation pressure force which is directed outward. If the radiation pressure to gravity ratio, often denoted as β is sufficiently high, the dust can be ejected outward. Those grains in hyperbolic orbits are often denoted as β-meteoroids, while those in in bound orbits are given as α-meteoroids (Zook & Berg 1975). Assuming that the larger dust grain that is fragmented moves in a circular orbit, its fragment attains a hyperbolic orbit if the radiation pressure to gravity ratio β exceeds 0.5. Based on light scattering models for different assumed dust compositions (Wilck & Mann 1996), this is the case for dust with sizes less than few 100 nm.

4.1. Mass of the impactors

The mass of the impactors can be estimated from the voltage observed, using Eq. (7) and spacecraft parameters from Sect. 2.2. For this, it is necessary to have an estimation of the velocity of the impactors and of the charge yield of the impacted material.
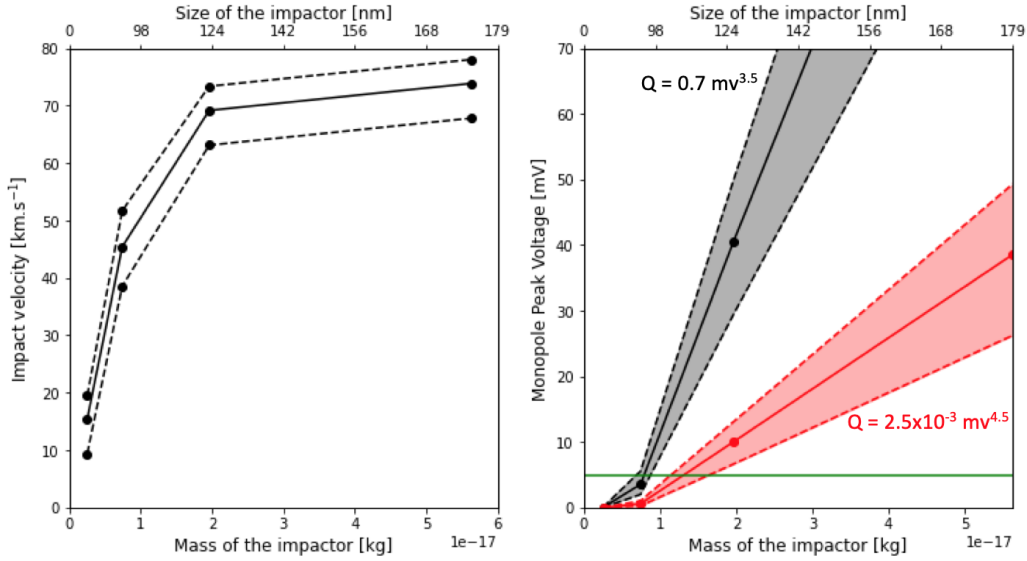
Fig. 7. Model for velocity and voltage peaks as a function of the impactor's mass or size. *Left panel*: relative velocity with respect to Solar Orbiter as a function of particle mass. The solid line shows the average along the spacecraft trajectory, the upper dashed line shows the impact velocity at the perihelion and the lower dashed line the impact velocity at the aphelion. *Right panel*: expected peak voltage as a function of the mass of the impactor, calculated using values of impact velocities shown on the left panel. The solid line shows the peak voltage for the averaged velocity (solid line from left panel) and dashed lines for the perihelion and aphelion impact velocities. The black curves assume a high charge yield and the red curves a lower charge yield. The points show the values of the velocity/peak voltage obtained from four numerical simulations, corresponding to size ranges 40−75 nm, 75−100 nm, 100−140 nm, and 140−200 nm. The points are placed at the middle of the mass interval for each of the four simulated size ranges. The horizontal green line shows the detection threshold ∼5 mV.

For the particle velocity, we could have used the order of magnitude obtained from the observations of impact rates in direction forward and backward with respect to the Sun. However, as pointed out in Sect. 3.1 this is only a rough estimation and is associated with large uncertainties. Therefore, we chose to rely in this section on estimations of dust particles velocities from numerical simulations of dust dynamics in the interplanetary medium. The simulation we use takes into account gravitational and radiation pressure forces, but not the electromagnetic force (which should not be dominant for particles of sizes ≳40 nm). We chose the values of β based on the assumption that the majority of Zodiacal dust originate from comets and asteroids and remain in the interplanetary medium for long time. We used the β value for the asteroidal dust; those for the old cometary dust in the interplanetary medium are almost identical (see Wilck & Mann 1996) and assuming them would not change the results of our calculations.

The charge yield of the impacted material is another unknown of our study, which certainly plays an important role in determining the mass of the impactors. Figure 7 shows the impact velocities from the numerical simulations and the expected peak voltage for two examples of charge yield. The dark area on the right panel shows the region of expected voltage peaks as a function of the mass of the impactor for parameters $A = 0.7$ and $\alpha = 3.5$ from McBride & McDonnell (1999). The red area is obtained for parameters $A = 2.5 \times 10^{-3}$ and $\alpha = 4.5$, a quite lower charge yield, corresponding to materials like germanium-coated Kapton or solar cells and MLI (multilayer thermal insulation) from STEREO's spacecraft, the charge yield of which were measured on the ground and displayed in Table 1 of Collette et al. (2014).

Figure 7 shows that particles in the size range 40−75 nm, regardless of the charge yield parameters used, are too small and not fast enough to produce measurable signals. Grains with sizes 75−100 nm (upper end) are expected to produce signals

above the detection threshold in the high-charge yield case, but not in the low-charge yield one; grains with sizes ≳100 nm, finally, should produce measurable signals regardless of the precise charge yield. An estimation of the mass of the smallest particles detected (we consider a threshold voltage of 5 mV) from this figure gives $m \simeq 0.8 \times 10^{-17}$ kg (high charge yield) and $m \simeq 1.3 \times 10^{-17}$ kg (low charge yield), corresponding to sizes of (assuming, as in the whole of this paper, a mass density $\rho = 2.5$ g.cm^{-3} and grains of spherical shapes for size-mass conversions) $r \simeq 92$ nm and $r \simeq 108$ nm, respectively; we can quite confidently affirm that the smallest grains detected have sizes around 100 nm.

The curves for different charge yields diverge when masses are increased, and for signals of amplitude, such as 30 mV, we have sizes $r \simeq 120$ nm (high yield) and $r \simeq 168$ nm (low yield), indicating a larger mismatch, of course, and showing the necessity of ground measurement if we want to reach a better mass calibration on the whole voltage interval. That said, the power-law decrease in the peak voltage distribution shown in the previous section implies that the fluxes are dominated by impact from small grains, so that the determination of the mass of impactors producing high amplitudes peaks is less critical for our study.

This discussion of particles masses is based on the measurement of the voltage pulses in monopole mode, which, as was discussed previously, are the most reliable when it comes to estimating the charge released by impact ionization, and therefore the dust particles masses. However, the dust detection algorithm from which fluxes are computed works on a TDS channel that is operated in dipole mode most of the time – when the instrument is on XLD1 mode. The discussion above, and the curve presented in Fig. 7, remains relevant to this case as long as the signal produced is proportional to the charge released Q. According to the estimation given by Eq. (3) this should be the case for dipole measurements when considering a large enough number of hits. Assuming $V_{\text{dipole}} = \Gamma Q / 4\pi\epsilon_0 L_{\text{ant}}$, the smallest mass measured in
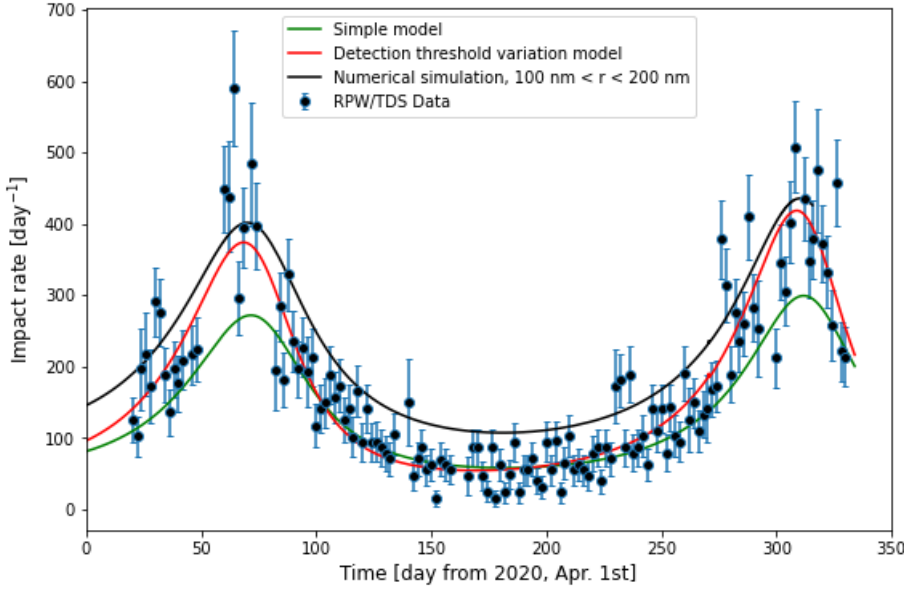
Fig. 8. Dust impact rate onto the spacecraft. Dots show the same data as the one presented in Fig. 3. The green curve shows the expected impact rate for beta meteoroids having a constant outward velocity $v_\beta = 50\,\mathrm{km\,s^{-1}}$, and a flux density $F_{1\,\mathrm{AU}} = 8 \times 10^{-5}\,\mathrm{m^{-2}\,s^{-1}}$ at 1 AU. The red curve shows the flux from Eq. (10) with $F_{1\,\mathrm{AU}} = 8 \times 10^{-5}\,\mathrm{m^{-2}\,s^{-1}}$ and $\alpha\delta = 1.3$. The black curve shows the prediction from numerical simulation based on a model of production of dust by collisional fragmentation. The collecting area is assumed to be equal to the heat shield's surface, $S_{\mathrm{col}} = 8\,\mathrm{m^2}$.

dipole would be a factor $4\pi\epsilon_0 L_{\mathrm{ant}}/C_{\mathrm{sc}} \sim 3$ larger (and therefore the sizes a factor ~ 1.4 larger). But the precise factor is complicated to evaluate, and could be closer to 1, on average, since observations of waveforms shows that differences in peak voltage from a monopole to another is often of the order of magnitude of the peak voltage itself. This provides a clear motivation for developing a quantitative theoretical modeling of the generation of signals generation in dipole mode, at least on a statistical basis.

4.2. Flux of β-meteoroids, comparison to predictions and measurements from other spacecraft

Figure 8 presents the impact rates averaged over two days (already presented on Fig. 3), together with impact rates computed for three models of the beta-meteoroid flux. The green line is the simplest model, with the impact rate given by:

$$R = F_{1\,\mathrm{AU}} S_{\mathrm{col}} \left(\frac{r}{1\,\mathrm{AU}}\right)^{-2} \frac{v_{\mathrm{impact}}}{v_\beta}, \qquad (9)$$

where $S_{\mathrm{col}} = 8\,\mathrm{m^2}$ is the collection area (taken equal to the heat shield surface; cf. Sect. 2.2), $v_{\mathrm{impact}} = \left\|v_\beta - v_{\mathrm{sc}}\right\|$ is the relative speed between the spacecraft and the β-meteoroids, the velocity of which is taken radial and constant, $v_\beta = 50\,\mathrm{km\,s^{-1}}$. Also, $F_{\beta,1\,\mathrm{AU}}$ is the flux of particles in the detection range, which is to a good approximation equal to the cumulative flux of particles larger than $\sim 100\,\mathrm{nm}$. The $1/r^2$ scaling of the β-meteoroids flux is a consequence of mass conservation (and of their production rate by fragmentation of larger particles being negligible at the distances from the Sun at which the spacecraft orbits). A fit of the data with Eq. (9) gives the following value for the cumulative flux: $F_{1\,\mathrm{AU}} \simeq 8 \times 10^{-5}\,\mathrm{m^{-2}\,s^{-1}}$.

This simple model provides, as can be seen on the figure, a fairly good agreement with the data, although it seems to systematically underestimate the high impact rate values around the perihelion. A reason for that can be seen from the left panel of Fig. 7: the mass of an impactor producing a given peak voltage will be smaller at the perihelion than at the aphelion (because the spacecraft's velocity with in the Sun's frame is larger at the perihelion that at the aphelion). Since smaller particles have higher

fluxes, an increase in the rate of measurable signals is expected close to the Sun as compared to the previous simple model.

This effect of decrease in the dust particles mass measured when approaching the Sun can be quantified by assuming a cumulative mass flux varying in power law with an exponent δ, as written in the previous section, in Eq. (8). The impact rate is then found to be:

$$R = F_{1\,\mathrm{AU}} S_{\mathrm{col}} \left(\frac{r}{1\,\mathrm{AU}}\right)^{-2} \frac{v_{\mathrm{impact}}}{v_\beta} \left(\frac{v_{\mathrm{impact}}}{v_{\mathrm{impact}}(1\,\mathrm{AU})}\right)^{\alpha\delta}, \qquad (10)$$

where $F_{1\,\mathrm{AU}}$ is (as previously) the cumulative flux of particles above the detection threshold at 1 AU and the factor $(v_{\mathrm{impact}}/v_{\mathrm{impact}}(1\,\mathrm{AU}))^{\alpha\delta}$ accounts for the variation of the mass of the detected impactors with the impact velocity.

We can fit Eq. (10) to the data in order to obtain the product $\alpha\delta$. The resulting curve is shown in red on Fig. 8. It shows a better agreement with data than the previous model and fits the high impact rates observed at the perihelion quite well. The value obtained is $\alpha\delta = 1.3$, which, considering values of $\alpha = 3.5-4.5$, provides an estimation of the power-law index of the cumulative mass distribution of the impactors $\delta = 0.29-0.37$. This value – obtained from a dataset with no voltage measurements but only impact counts per unit time – is similar to the one derived in the previous section by fitting peak voltage distributions, indicating that the estimation of δ in RPW's detection range seems quite robust. Finally, we note that assuming the measurement of δ from voltage distributions to be reliable enough, we could use this estimation of $\alpha\delta$ to independently estimate the power-law index α of the charge yield for Solar Orbiter material. We would then obtain $\alpha \simeq 1.3/0.34 \simeq 3.9$.

The black curve on Fig. 8, finally, shows the prediction of impacts onto the spacecraft from a model of production of small dust grains by collisional fragmentation. This model assumes that the parent bodies move in Keplerian orbits within the circumsolar dust disk. Their mass distribution is a modified version of the interplanetary dust flux model (Gruen et al. 1985). The size distribution of the collision fragments are described based on models by Tielens et al. (1994) and Jones et al. (1996). It describes the fragmentation and partial vaporization of a target and projectile composed of a certain dust material. The vaporized and fragmented mass of the target are proportional

to the projectile mass and to the velocity – and material-dependent coefficients. The mass distribution of fragments is of the form $m^{-0.76}$, with the largest fragment mass specified as some (collision-velocity dependent) fraction of the target mass. A brief description of the collision model is given in Mann & Czechowski (2005), while the derivation of dust fluxes is described in Mann & Czechowski (2021). They are obtained from the dust trajectories under the influence of gravity and radiation pressure (since the Lorentz force does not have a strong influence for the considered dust sizes). The same trajectories were used to produce Fig. 7 of this article. The black curve shows the prediction from this model of the number of particles comprised between 100 nm and 200 nm impacting a surface $S_{col} = 8\,m^2$ per day. The curve obtained from the model considers a constant minimal size of detected dust at 100 nm all along the trajectory. It does not include the effect of variation of minimal mass detected discussed previously. It fits (without the need to vary any free parameter) the high impact rates at perihelion, but quite overestimates the low fluxes period. This would tend to indicate that the size of the particles detected is closer to 100 nm at the perihelion and probably a bit larger at aphelion.

Some effects that can play a role on the derivation of the particle flux from the observed impact rates have not been taken into account in this first study. They include a better model for the collection surface and its possible variation with distance to the Sun (the direction of the dust velocity in the spacecraft frame varying along the trajectory), although given the mostly cubic shape of the spacecraft, this effect is not expected to be very important. A possible difference in charge yield for an impact on the heat shield surface and one of the other five spacecraft walls could also be of some importance.

The result that we obtained for the β-meteoroid flux is similar to (although slightly higher than) the one derived using STEREO/WAVES by Zaslavsky et al. (2012), of $F_\beta \simeq 1$–$6 \times 10^{-5}\,m^{-2}\,s^{-1}$ at 1 AU; it is also similar to the measurement with Solar Probe Plus FIELD instrument $F_\beta \simeq 3$–$7 \times 10^{-5}\,m^{-2}\,s^{-1}$ interpolated at 1 AU (Szalay et al. 2020) and to the theoretical expectations, as shown in this paper.

In conclusion, we note that if the presented data can be described well with a flux of β-meteoroids, it is found to be lacking, in comparison to the observations from STEREO (Zaslavsky et al. 2012; Belheouane et al. 2012) or Wind (Malaspina et al. 2014), an observed flux of interstellar dust. The latter studies indeed showed a noticeable component of the impact rate modulated along the solar apex direction, which is not observed with Solar Orbiter RPW. This lack of an apparent interstellar dust component in the data is puzzling. It could be explained by a deflection of the interstellar dust grains in the solar magnetic field and the consequent depletion of their flux inside 1 AU, which is expected for grains of small size (Mann 2010). This is a point which deserves further study.

5. Conclusions

The analysis of the first data from Solar Orbiter Radio and Plasma Wave instrument shows this instrument to be a quite reliable dust detector for dust grains in the size range $\gtrsim 100$ nm. The fluxes of particles derived are consistent with previous observations in this size range and with theoretical prediction from models of dust production by collisional fragmentation.

The analysis of the difference in impact rates when the spacecraft's velocity vector is directed sunward or anti-sunward is shown to be capable of providing a direct measurement on the order of magnitude of dust grains radial velocities, $v_{r,dust} \sim$

$50\,km\,s^{-1}$, which is consistent with theoretical predictions in the observed size range.

The analysis of voltage distribution in monopole mode, along with the analysis of the impact rates taking into account a variation of the mass of the smallest grains detected as a function of the impact velocity provide two independent methods for estimating the power law index δ of the cumulative mass flux of particles in our detection range. These two methods consistently provide a result of $\delta \simeq 1/3$.

These first results are very promising overall. Still, a great deal of work remains to be done, in particular: a modeling of the signal generation mechanism in monopole mode that would include the effect of variation of the floating potential relaxation time with the local plasma parameters, as well as models of signal generation in dipole mode. Such works, together with a more precise modeling of grain's velocity and additional statistics, could make it possible to derive more information on the dust cumulative mass flux from the peak voltage distributions.

Solar Orbiter will reach perihelion close to 0.3 AU in spring 2022. The impact rate is expected to be about three times (without taking the mass detection threshold effect) larger at this point than at the perihelion studied in this article. Solar Orbiter's orbit will also reach increasingly higher latitudes in the years to come and will provide the first in situ exploration of the inner Solar System dust cloud out of the ecliptic. These perspectives are very promising and these first results show that RPW will have the capabilities to provide a scientific return from these opportunities.

References

Aubier, M. G., Meyer-Vernet, N., & Pedersen, B. M. 1983, Geophys. Res. Lett., 10, 5
Auer, S. 2001, in Instrumentation, eds. E. Grün, B. S. Gustafson, S. Dermott, & H. Fechtig (Berlin, Heidelberg: Springer, Berlin Heidelberg), 385
Bale, S. D., Goetz, K., Harvey, P. R., et al. 2016, Space Sci. Rev., 204, 49
Belheouane, S., Zaslavsky, A., Meyer-Vernet, N., et al. 2012, Sol. Phys., 281, 501
Bougeret, J. L., Kaiser, M. L., Kellogg, P. J., et al. 1995, Space Sci. Rev., 71, 231
Bougeret, J.-L., Goetz, K., Kaiser, M. L., et al. 2008, Space Sci. Rev., 136, 487
Collette, A., Grün, E., Malaspina, D., & Sternovsky, Z. 2014, J. Geophys. Res.: Space Phys., 119, 6019
Dietzel, H., Eichhorn, G., Fechtig, H., et al. 1973, J. Phys. E: Sci. Instrum., 6, 209
Gruen, E., Zook, H. A., Fechtig, H., & Giese, R. H. 1985, Icarus, 62, 244
Gurnett, D. A., Grün, E., Gallagher, D., Kurth, W. S., & Scarf, F. L. 1983, Icarus, 53, 236
Gurnett, D. A., Kurth, W. S., Scarf, F. L., et al. 1987, J. Geophys. Res.: Space Phys., 92, 14959
Gurnett, D. A., Kurth, W. S., Granroth, L. J., & Poynter, S. C. A. R. L. 1991, J. Geophys. Res., 96, 19,177
Gurnett, D. A., Kurth, W. S., Kirchner, D. L., et al. 2004, Space Sci. Rev., 114, 395
Issautier, K., Meyer-Vernet, N., Moncuquet, M., & Hoang, S. 1998, J. Geophys. Res., 103, 1969
Jones, A. P., Tielens, A. G. G. M., & Hollenbach, D. J. 1996, ApJ, 469, 740
Leinert, C., Richter, I., Pitz, E., & Planck, B. 1981, A&A, 103, 177
Lhotka, C., Rubab, N., Roberts, O. W., et al. 2020, Phys. Plasmas, 27, 103704
Maksimovic, M., Bale, S. D., Chust, T., et al. 2020, A&A, 642, A12
Malaspina, D. M., Horanyi, M., Zaslavsky, A., et al. 2014, Geophys. Res. Lett., 41, 266

Malaspina, D. M., Szalay, J. R., Pokorný, P., et al. 2020, ApJ, 892, 115
Mann, I. 2010, ARA&A, 48, 173
Mann, I., & Czechowski, A. 2005, ApJ, 621, L73
Mann, I., & Czechowski, A. 2021, A&A, 650, A29
Mann, I., Kimura, H., Biesecker, D. A., et al. 2004, Space Sci. Rev., 110, 269
Mann, I., Meyer-Vernet, N., & Czechowski, A. 2014, Phys. Rep., 536, 1
Mann, I., Nouzák, L., Vaverka, J., et al. 2019, Ann. Geophys., 37, 1121
McBride, N., & McDonnell, J. A. M. 1999, Planet. Space Sci., 47, 1005
Meyer-Vernet, N., & Perche, C. 1989, J. Geophys. Res., 94, 2405
Meyer-Vernet, N., Aubier, M. G., & Pedersen, B. M. 1986, Geophys. Res. Lett., 13, 617
Meyer-Vernet, N., Maksimovic, M., Czechowski, A., et al. 2009a, Sol. Phys., 256, 463
Meyer-Vernet, N., Lecacheux, A., Kaiser, M. L., & Gurnett, D. A. 2009b, Geophys. Rev. Lett., 36, L03103
Meyer-Vernet, N., Moncuquet, M., Issautier, K., & Lecacheux, A. 2014, Geophys. Rev. Lett., 41, 2716
Meyer-Vernet, N., Moncuquet, M., Issautier, K., & Schippers, P. 2017, J. Geophys. Res.: Space Phys., 122, 8
Müller, D., St. Cyr, O. C., Zouganelis, I., et al. 2020, A&A, 642, A1
Oberc, P. 1990, Icarus, 86, 314
Page, B., Bale, S. D., Bonnell, J. W., et al. 2020, ApJS, 246, 51
Pantellini, F., Landi, S., Zaslavsky, A., & Meyer-Vernet, N. 2012, Plasma Phys. Controlled Fusion, 54
Pedersen, B. M., Meyer-Vernet, N., Aubier, M. G., & Zarka, P. 1991, J. Geophys. Res.: Space Phys., 96, 19187
Soucek, J., Píša, D., Kolmasova, I., et al. 2021, A&A, 656, A26 (SO Cruise Phase SI)
Stverak, S., Travnicek, P. M., & Hellinger, P. 2015, J. Geophys. Res.: Space Phys., 120, 8177
Szalay, J. R., Pokorný, P., Bale, S. D., et al. 2020, ApJS, 246, 27
Tielens, A. G. G. M., McKee, C. F., Seab, C. G., & Hollenbach, D. J. 1994, ApJ, 431, 321
Vaverka, J., Nakamura, T., Kero, J., et al. 2018, J. Geophys. Res.: Space Phys., 123, 6119
Vaverka, J., Pavlu, J., Nouzák, L., et al. 2019, J. Geophys. Res.: Space Phys., 124, 8179
Wehry, A., & Mann, I. 1999, A&A, 341, 296
Wilck, M., & Mann, I. 1996, Planet. Space Sci., 44, 493
Ye, S.-Y., Gurnett, D. A., Kurth, W. S., et al. 2014, J. Geophys. Res.: Space Phys., 119, 6294
Ye, S.-Y., Kurth, W. S., Hospodarsky, G. B., et al. 2018, Geophys. Res. Lett., 45, 10,101
Ye, S.-Y., Vaverka, J., Nouzak, L., et al. 2019, Geophys. Res. Lett., 46, 10941
Zaslavsky, A. 2015, J. Geophys. Res.: Space Phys., 120, 855
Zaslavsky, A., Meyer-Vernet, N., Mann, I., et al. 2012, J. Geophys. Res., 117, A05102
Zook, H. A., & Berg, O. E. 1975, Planet. Space Sci., 23, 183

C

MACHINE LEARNING DETECTION OF DUST IMPACT SIGNALS OBSERVED BY THE SOLAR ORBITER

Machine Learning Detection of Dust Impact Signals Observed by The Solar Orbiter

Andreas Kvammen[1], Kristoffer Wickstrøm[1], Samuel Kociscak[1], Jakub Vaverka[2], Libor Nouzak[2], Arnaud Zaslavsky[3], Kristina Rackovic[3,4], Amalie Gjelsvik[1], David Pisa[5], Jan Soucek[5], and Ingrid Mann[1]

[1]Department of Physics and Technology, UiT The Arctic University of Norway, 9037, Tromsø, Norway
[2]Department of Surface and Plasma Science, Charles University Prague, 18000, Prague, Czech Republic
[3]LESIA – Observatoire de Paris, Université PSL, CNRS, Sorbonne Université, Université de Paris, 5 place Jules Janssen, 92195, Meudon, France
[4]Department of Astronomy, Faculty of Mathematics, University of Belgrade, Studentski trg 16, 11000, Belgrade, Serbia
[5]Institute of Atmospheric Physics, Czech Academy of Sciences, Bocni II/1401, 141 00 Prague, Czech Republic

Correspondence: Andreas Kvammen (andreas.kvammen@uit.no)

Abstract. This article present results from automatic detection of dust impact signals observed by the Solar Orbiter – Radio and Plasma Waves instrument.

A sharp and characteristic electric field signal is observed by the Radio and Plasma Waves instrument when a dust particle impact the spacecraft at high velocity. In this way, ∼5–20 dust impacts are daily detected as the Solar Orbiter travels through the interstellar medium. The dust distribution in the inner solar system is largely uncharted and statistical studies of the detected dust impacts will enhance our understanding of the role of dust in the solar system.

It is however challenging to automatically detect and separate dust signals from the plural of other signal shapes for two main reasons. Firstly, since the spacecraft charging causes variable shapes of the impact signals and secondly because electromagnetic waves (such as solitary waves) may induce resembling electric field signals.

In this article, we propose a novel machine learning-based framework for detection of dust impacts. We consider two different supervised machine learning approaches: the support vector machine classifier and the convolutional neural network classifier. Furthermore, we compare the performance of the machine learning classifiers to the currently used on-board classification algorithm and analyze one and a half year of Radio and Plasma Waves instrument data.

Overall, we conclude that classification of dust impact signals is a suitable task for supervised machine learning techniques. In particular, the convolutional neural network achieves a 96% ± 1% overall classification accuracy and 94% ± 2% dust detection precision, a significant improvement to the currently used on-board classifier with 85% overall classification accuracy and 75% dust detection precision. In addition, both the support vector machine and the convolutional neural network detects more dust particles (on average) than the on-board classification algorithm, with 14% ± 1% and 16% ± 7% detection enhancement respectively.

The proposed convolutional neural network classifier (or similar tools) should therefore be considered for post-processing of the electric field signals observed by the Solar Orbiter.

1 Introduction

1.1 The Dust Population in the Inner Solar System

The interplanetary dust population in the inner solar system (≤ 1 AU) is formed by collisional fragmentation of asteroids, comets and meteoroids. The meteoroids and the larger dust particles are in bound orbits around the Sun and their lifetime is limited by collisions, while the smaller particles that form through collisional fragmentation are repelled from the Sun by the radiation pressure force. The sources and sinks of the interplanetary dust particles are well-measured at the orbit of Earth, while there are few observations inside 1 AU.

Model calculations show that the number density of dust within 1 AU is diminished by collisional destruction (Ishimoto, 2000). However, there are a number of uncertainties that enter the model calculations since the dust collision rates depend both on the dust number density distribution and on the relative velocities between the dust particles. These parameters are generally unknown inside the orbit of the Earth and the estimated sizes of the fragmented dust particles are currently based on empirical relations, inferred from laboratory measurements of accelerated dust particles (Mann and Czechowski, 2005). Furthermore, there is an additional dust population with interstellar origin that stream through the solar system. The interstellar dust distribution is largely unknown and thus complicates the analysis of the stellar dust population. Remote observations of the zodiacal light and the Fraunhofer corona (F-corona) provide some information of the dust population dust within 1 AU, but mainly of the larger ($> \mu$m) dust particles (Mann et al., 2004). For all these reasons, in-situ measurements are needed in order to better understand the role of dust in the inner solar system.

1.2 Exploration of the Inner Solar System

At present, the inner solar system is explored by the Parker Solar Probe (Szalay et al., 2020), launched August 12, 2018, and the Solar Orbiter (Müller et al., 2020), launched February 10, 2020. While systematic studies of the dust flux near 1 AU are conducted with the Solar Terrestrial Relations Observatory (STEREO) (Zaslavsky et al., 2012) and Wind (Malaspina et al., 2014). The first analyses show that a large fraction of the observed dust particles are repelled from the Sun, i.e. the dust particles are in unbound orbits (Zaslavsky et al., 2021; Szalay et al., 2020; Malaspina et al., 2020). Mann and Czechowski (2021) used model calculations to explain the impact rates observed by the Parker Solar Probe with dust particles in unbound orbits with sizes larger than $\sim$100 nm. Mann and Czechowski (2021) modeled the dust production by collisional fragmentation near the Sun and the dust trajectories were calculated with included radiation pressure and Lorentz force terms. Mann and Czechowski (2021) showed that the observed impacts largely agrees with the model calculations for dust > 100 nm and the differences are possibly due to the influence of smaller particles, of local and temporal variations and of other dust components, such as dust in bound orbits and interstellar dust.

In this work, we analyze data acquired by the Solar Orbiter. The spacecraft orbits the Sun in an elliptic orbit with a period of approximately 6 months. At perihelion, the Solar Orbiter reaches a minimum solar distance of 0.28 AU, just within the

55 perihelion of the Mercury orbit. The expected mission duration is 7 years, with a possible 3 year extension. The Solar Orbiter will thus provide long-term, in-situ observations of the environment in the inner solar system with multiple instruments. One of these instruments is the Radio and Plasma Waves instrument, allowing observations of the cosmic dust flux with typical diameters ranging from ∼100 nm to ∼500 nm (Zaslavsky et al., 2021).

1.3 Radio and Plasma Waves Instruments for Dust Detection

60 Radio and plasma waves instruments (i.e. antennas) have been used for studying dust in the solar system since the Voyager mission (Gurnett et al., 1983; Aubier et al., 1983). A dust impact is observed by the spacecraft antennas as a sharp and characteristic electric field signal, produced by the impact ionization process.

The impact ionization process occur when dust particles hit a target in space with impact speeds on the order of ∼km/s or
65 larger, impact speeds which are typical for space missions in the interplanetary medium. The kinetic energy of the impact is transferred into deformation, shattering, melting and vaporization of the dust projectile– and target material, producing a cloud of free electrons and ions on the spacecraft surface. Laboratory measurements (Collette et al., 2014) and model calculations (Hornung et al., 2000) indicate that the free-charge yield depends on multiple parameters, where the most important are the dust impact velocity, the dust mass and the material of both the dust projectile and the target (the spacecraft surface) (Mann
70 et al., 2019). The forming cloud of charged particles is partly expanding into the ambient solar wind and is partly recollected by the spacecraft. This induces the characteristic electric field signal, hereafter called a dust impact signal/waveform.

Radio and plasma waves instruments allow for the the entire spacecraft body to serve as a dust detector, providing a large collection area in comparison to dedicated dust instruments. Thus, radio and plasma waves instrument can provide dust distri-
75 bution estimates based on thousands of dust impacts each year, statistical products that are difficult to acquire by dedicated dust instruments. Still, the radio and plasma waves instruments have lower sensitivities than dedicated dust detectors (Zaslavsky, 2015) and the shape of the dust impact waveform is highly dependent on the potential difference between the spacecraft and the ambient plasma (Vaverka et al., 2017). This complicates the analysis of the dust distribution in the solar system since statistical studies rely on automatic dust impact detection software with high accuracy.

80 ### 1.4 Machine Learning Classification of Time Series Data

In this article, we present a machine learning-based framework as a novel method for detecting dust impact signals in radio and plasma waves instrument data. Machine learning methods, in particular neural networks in the recent decade, have been extensively used for challenging time series classification problems, such as: speech recognition (Trosten et al., 2019), heart rate monitoring (Wickstrøm et al., 2022) and human activity classification (Villar et al., 2016).

85

A neural network has previously been used for selecting the signals of interest observed by the WAVES instrument on board the Wind spacecraft (Bougeret et al., 1995). While an unsupervised method (self-organizing maps) was used for identifying and

categorizing plasma waves in the magnetic field data observed by the MMS$_1$ spacecraft (Vech and Malaspina, 2021). Still, no machine learning tools have been developed for classifying dust impacts in radio and plasma waves instrument data, although the characteristic signal produced by the impact ionization process is distinctive and could therefore be suitable for machine learning detection.

1.5 Motivation and Article Structure

The main purpose of this work was to develop a dedicated dust detection tool that can be used to automatically process the large amount of data acquired by the Radio and Plasma Waves instrument on board the Solar Orbiter. The aim was to develop a classifier with a high overall classification accuracy on a balanced data set that would make statistical studies more reliable and easier to conduct. For this project, we defined high accuracy to be ($\gtrsim 95\%$) after some initial testing. We considered ($\gtrsim 95\%$) accuracy to be satisfactory for statistical studies and a significant improvement to the currently used classification system. In order to achieve this objective we used supervised machine learning techniques to develop the dust classifiers, trained and tested on a set of 3000 manually labeled observations.

The remaining of this article is structured as follows. Section 2 explains the Solar Orbiter – Radio and Plasma Waves observations and the on-board algorithm that is currently used for dust impact detection. Section 3 describes the procedure that was used for developing the machine learning classifiers; from the downloaded data to the training– and testing of the classifiers. Section 4 investigate the performance of the classifiers and includes the resulting dust impact rates, calculated by analyzing one and a half year of automatically classified Solar Orbiter data. Finally, Section 5 presents the overall conclusions of this project.

2 Observations and Data Acquisition

2.1 The Radio and Plasma Waves (RPW) Instrument and the Time Domain Sampler (TDS) Receiver

This work focuses on electric field signals (i.e. waveforms) observed by the Radio and Plasma Waves (RPW) instrument on-board the Solar Orbiter (Maksimovic et al., 2020). The RPW instrument consist of 3 antennas operating synchronously and the measured electric potential is recorded by the Time Domain Sampler (TDS) receiver unit (Soucek et al., 2021).

The TDS receiver is designed to capture plasma waves (such as ion-acoustic and Langmuir waves) in the frequency range 200 Hz – 100 kHz, in addition to the dust impact signals (Soucek et al., 2021). The antenna voltages are converted to electric field values using the antenna effective lengths, but are otherwise uncalibrated. We consider only signals sampled with a sampling rate of 262.1 kHz in snapshots of 16384 time steps, acquired when the TDS receiver was operating in the XLD1 mode.

The XLD1 mode is the most commonly used observational mode of the RPW-TDS system (Soucek et al., 2021). XLD1 is a hybrid mode, where channel 3 (CH_3) is operating in monopole mode while channel 1 (CH_1) and channel 2 (CH_2) are operating in dipole mode:

$$CH_1 = \left(\frac{V_1 - V_{SC}}{L_1}\right)\hat{L}_1 - \left(\frac{V_3 - V_{SC}}{L_3}\right)\hat{L}_3 \tag{1}$$

$$CH_2 = \left(\frac{V_2 - V_{SC}}{L_2}\right)\hat{L}_2 - \left(\frac{V_1 - V_{SC}}{L_1}\right)\hat{L}_1 \tag{2}$$

$$CH_3 = \left(\frac{V_2 - V_{SC}}{L_2}\right)\hat{L}_2 \tag{3}$$

where $V_i - V_{SC}$ denotes the potential difference between antenna i and the spacecraft body along the antenna boom with unit vector $\hat{L}_i$ and effective length L_i. For this work however, the 3 RPW antenna signals are all converted to monopole electric field signals ($\bar{E}_1$, $\bar{E}_2$, $\bar{E}_3$) by the following conversion:

$$\bar{E}_1 = CH_3 - CH_2 = \left(\frac{V_2 - V_{SC}}{L_2}\right)\hat{L}_2 - \left(\left(\frac{V_2 - V_{SC}}{L_2}\right)\hat{L}_2 - \left(\frac{V_1 - V_{SC}}{L_1}\right)\hat{L}_1\right) = \left(\frac{V_1 - V_{SC}}{L_1}\right)\hat{L}_1 \tag{4}$$

$$\bar{E}_2 = CH_3 = \left(\frac{V_2 - V_{SC}}{L_2}\right)\hat{L}_2 \tag{5}$$

$$\bar{E}_3 = CH_3 - CH_2 - CH_1 = \bar{E}_1 - CH_1$$
$$= \left(\frac{V_1 - V_{SC}}{L_1}\right)\hat{L}_1 - \left(\left(\frac{V_1 - V_{SC}}{L_1}\right)\hat{L}_1 - \left(\frac{V_3 - V_{SC}}{L_3}\right)\hat{L}_3\right) = \left(\frac{V_3 - V_{SC}}{L_3}\right)\hat{L}_3 \tag{6}$$

2.2 The Triggered Snapshot WaveForms (TSWF) data product and the TDS Classifier

For this project, we use the Triggered Snapshot WaveForms (TSWF) data product, processed with software version 2.1.1 and acquired over a one and a half year period, spanning between June 15, 2020, to December 16, 2021. The TSWF data product consists of signal packets (63 ms snapshots) that are downlinked only if the classification algorithm on-board the Solar Orbiter is triggered. The accuracy of the on-board classification algorithm is therefore important in order to optimize the data transfer and provide reliable data products for statistical analysis.

The input to the on-board classification algorithm, hereafter named the TDS classifier or the TDS classification algorithm, is the 63 ms signal packet, while the output is categorized into one out of three labels: *dust*, *wave* or *other*. The TDS classifier assigns the label based on 3 extracted features.

1. The snapshot peak amplitude

2. The ratio of the peak amplitude to the median of the signal

3. The bandwidth of the main spectral peak identified in the Fourier spectrum

The signal label is then determined by comparing the extracted feature values against configurable thresholds. For more detailed descriptions of the TDS classifier, see Maksimovic et al. (2020) and Soucek et al. (2021). Figure 1 presents a few examples of

recorded snapshots with included labels, as classified by the TDS classification algorithm.
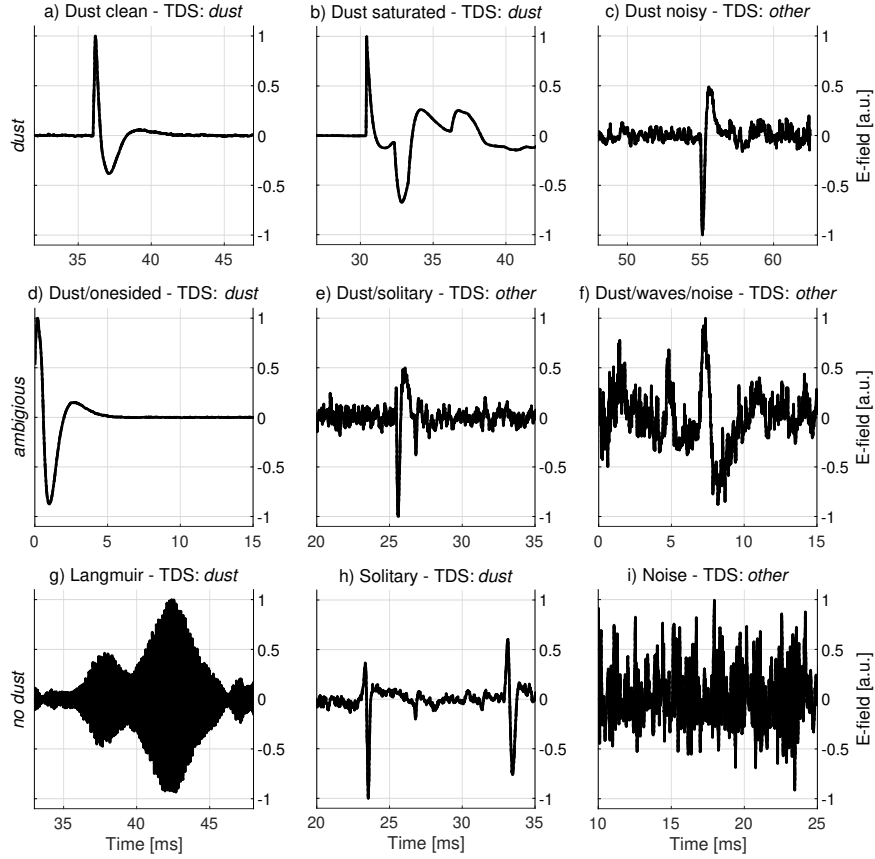

Figure 1. Waveforms recorded by the TDS receiver and measured by one of the RPW antennas. The signal label, classified by the TDS classification algorithm, is included for each snapshot in the subplot titles. The top row presents dust waveforms: a) is a clean dust impact waveform, b) shows a dust impact that saturates the receiver unit (or reaches the non-linearity limit), c) presents a weak dust impact signal that is strongly affected by noise. The middle row presents ambiguous waveforms: d) might be a dust impact, but information is limited by the signal framing, e) is likely a dust impact, but the signal shape resembles solitary waves and is strongly affected by noise, f) might be a dust impact, but noise and possible electromagnetic waves makes the signal difficult to interpret. The bottom row presents waveforms without dust: g) shows Langmuir waves, characterized by the high-frequency E-field oscillations with a lower-frequency amplitude modulation, h) presents solitary waves, which sometimes resemble dust impact waveforms, i) shows a signal dominated by noise, without any clear features. Note that the full (63 ms) snapshots are zoomed to 15 ms intervals around the interesting features and that the signal amplitudes are normalized to ±1 and centered around zero for illustrative purposes.

Figure 1 illustrates that it is challenging to detect and separate dust signals from the plural of other signal shapes. In particular, the dust waveform in Sub-figure c) is classified as *other*, while the Langmuir wave and solitary wave snapshots in Sub-figures g) and h) are erroneously classified as *dust* by the TDS classification algorithm.

3 Machine Learning-Based Framework for Automatic Dust Impact Detection

The goal of the machine learning classifier is to take a monopole RPW snapshot as an input and automatically output if the signal contains a dust impact or not. For this purpose, we use a supervised classifier. A supervised classifier relies on manually labeled data to learn (i.e. train) the function that maps the input observation (the electric field signal) to the output label. For this work, we focus on detecting dust impact signals, we therefore use a binary label: *dust* or *no dust*. Additional labels, such as: *ion-acoustic waves*, *Langmuir waves* and *solitary waves*, could however be implemented in a similar machine learning-based framework.

3.1 Data Pre-Processing for Machine Learning Classification

In order to construct a balanced data set, we selected ~ 1500 waveforms classified as *dust* and ~ 1500 waveforms classified as *wave/other* by the TDS classification algorithm. The signals were randomly drawn from the TDS data archive and acquired between 15 June 2020 to 16 December 2021. The TDS signals were then pre-processed in order to standardize the input to the classifier and speed up the training. Standardized data further reduces bias effects and makes the manual labeling of the signals easier to conduct. For this work, a 4-step pre-processing procedure was used independently on each antenna signal, the pre-processing procedure applied on a sample signal is illustrated in Figure 2.

1. **Remove the signal offset** The electric field offset is removed by subtracting the raw signal with the median of a heavily filtered version of the raw data. A sliding median filter over 21 time steps was selected by visual inspection of the noise characteristics. The removal of the electric field offset centers the signal around zero and reduces bias effects from offset waveforms.

2. **Filter the data** The signal is filtered using a sliding median filter over 7 time steps in order to reduce the high-frequency noise. The 7 time step filter was selected by inspecting the power spectrum of impact signals and by noticing that most information above ($f_N = 35$ kHz) is buried in noise, although the TDS sampling frequency is higher ($f_s = 262.1$ kHz), thus making a filter length ($< f_s/f_N \approx 7.5$) appropriate without significant loss of information.

3. **Compress the data** The signal is re-sampled with a compression factor of 4 using linear 1-dimensional interpolation. The compression is done to speed up the training of the classifier, resulting in a re-sampling from 16384 to 4096 time steps.

4. **Normalize the signal** The data is normalized to be between -1 and 1 by dividing all data samples with the maximum absolute value of the signal. The normalization makes the machine learning classifier more robust to variations in the signal strength and eases the parameter optimization.
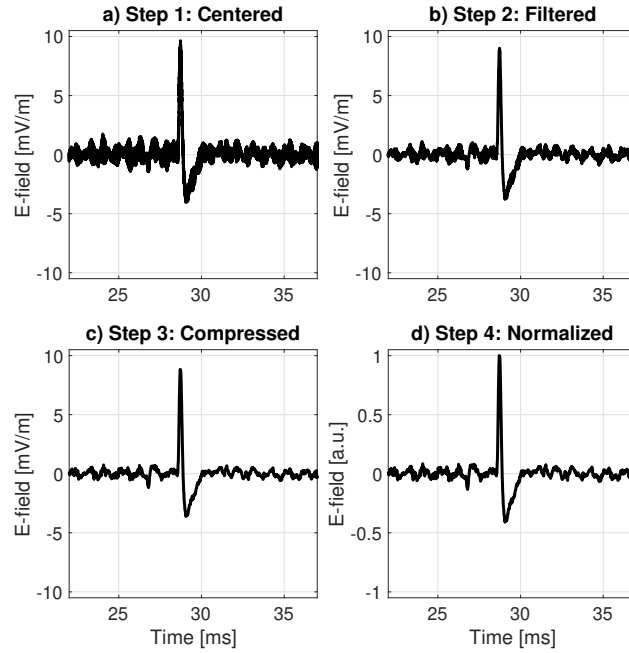
7

Figure 2. A dust waveform observed by antenna 2 on September 8, 2021. The sub-figures illustrate the different stages of the pre-processing procedure. a) The electric field offset is removed and the signal is centered around 0 mV/m. b) The signal is filtered by a median filter over 7 time steps to reduce the high-frequency noise. c) The signal is compressed by a factor of 4 to reduce the data size. d) The waveform is normalized by the maximum absolute value of the signal in order to ease the parameter optimization of the machine learning classifier. Note the waveform is zoomed to a 15 ms time period around the dust impact in order to better visualize the impact shape modification by the pre-processing procedure.

3.2 Manual Waveform Labeling

Manually labeled data is used both to train the machine learning classifiers and to test the performance of the trained models. Thus, great care is needed in order to construct a high-quality labeled data set, without significant contamination of corrupted data files, biases and mislabeled signals.

We manually labeled the data into either *dust* or *no dust*. Each signal was displayed without indications of the previously assigned label by the TDS classifier in order to reduce bias effects. Furthermore, a zoom function was used to investigate the areas of interest and options were included both to correct labeling mistakes by the user and to indicate ambiguous signals that do not clearly fit into any label (*dust* or *no dust*). Appendix A presents the Graphical User Interface (GUI) that was used to label the 3000 observations.

8

It should be noted that 134 signals (i.e. 4.5%), out of 3000 manually labeled waveforms, were marked as ambiguous and did not clearly fit into either the *dust* or *no dust* label, see Figure 1 for ambiguous examples. Furthermore, the manual waveform labeling was done by one scientist, although with consultations with other experts. Thus, it is to be expected that different scientists will disagree on a proportion (around 5%) of the the manual labels. The disagreement level could possibly be reduced if several experts labeled the same data set and the labeling consensus was used as the effective waveform label.

3.3 Developing the Machine Learning Classifiers

The manually labeled data was split into a training set (containing 80% of the data) and a testing set (with the remaining 20%). The training data is used to optimize the free parameters of the machine learning classifier with respect to the assigned labels, while the testing data is used as an independent set to test the performance of the trained classifiers. The performance of a machine learning classifier is quantified by comparing the outputs of the trained model to the labels of the testing data. Figure 3 illustrates the data flow; from the TDS data sets to the machine learning performance metrics.
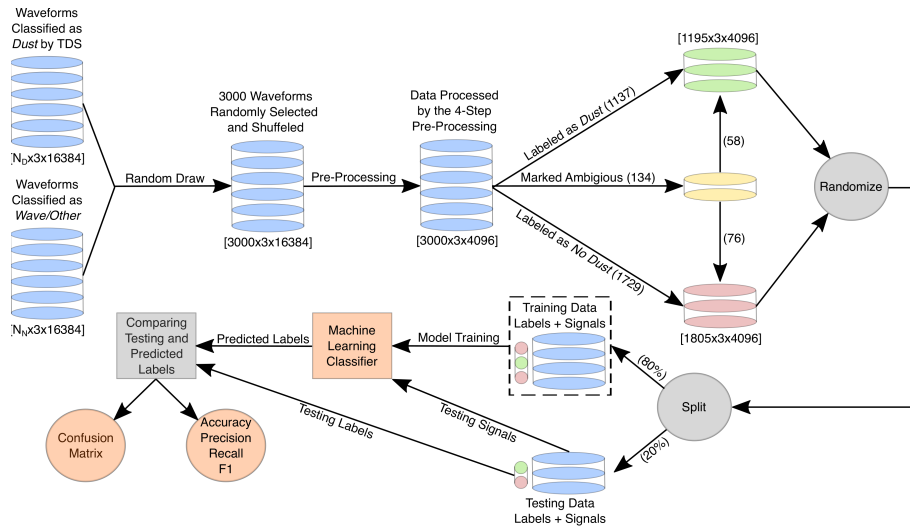
Figure 3. Data flow: from the TDS data sets to the machine learning performance metrics. The diagram illustrates the data flow by the black arrows and the applied process by the arrow label. The cylinders indicate the signal waveforms and the cylinder color indicate the associated label. The gray circles mark data transformation processes. The random draw of the TDS data and the pre-processing is explained in Sub-section 3.1, while the manual labeling is described in Sub-section 3.2. The randomization and splitting of the manually labeled data into a training and a testing set is described in Sub-section 3.3 and the training and testing of the machine learning classifiers is explained in Sub-sections 3.4 and 3.5. Finally, the performance of the machine learning classifiers are compared and evaluated in Sub-section 4.1.

There are numerous machine learning techniques that are suitable for time series classification. In this work, we focus on two well-known techniques: the Support Vector Machine (SVM) and the Convolutional Neural Network (CNN).

3.4 The Support Vector Machine (SVM)

205 The support vector machine (Boser et al., 1992; Cortes and Vapnik, 1995) is a robust and versatile classification algorithm, considered to be one of the most influential approaches in supervised learning (Goodfellow et al., 2016). SVMs learn the decision hyperplane that maximizes the discriminative power between the observations categorized into two classes (in this case: *dust* or *no dust*). However, SVMs are highly dependent on the representation of the data and often achieve sub-optimal performance on high-dimensional data (when used directly). In this case, the observation from 3 antenna measurements, each

210 with 4096 time steps, is both high dimensional and noisy (each time step contain little information). It is therefore common to extract important characteristics (i.e. features) from the data to provide the SVM with compactly represented information with less noise and redundancies.

3.4.1 Feature Extraction

215 In order to develop a baseline machine learning classifier, comparable to the on-board TDS classification algorithm, a 2-dimensional SVM classifier was considered. Thus, every observation with dimension (3x4096) is represented by a 2-dimensional feature vector (1x2). After some initial testing, we selected two features that had a high discriminative power between the *dust* and *no dust* observations.

220 1. **The standard deviation** The mean standard deviation is calculated over the 3 antenna channels, each with 4096 time steps. The standard deviation is appropriate since normalized *dust* signals typically have a lower mean standard deviation than normalized *no dust* signals.

2. **The convolution ratio** The $\log_{10}$ value of the convolution ratio ($|\mathrm{conv}|_{\mathrm{max}}/|\mathrm{conv}|_{\mathrm{median}}$) is calculated, where |conv| is the absolute values of the convolution of the antenna signals with a normalized Gaussian of width 0.5 ms. $|\mathrm{conv}|_{\mathrm{max}}$ is

225 the maximum value of |conv|, while $|\mathrm{conv}|_{\mathrm{median}}$ is the median. The convolution ratio was selected as a feature since the *dust* signals typically have a larger convolution ratio than the *no dust* signals. The Gaussian width of 0.5 ms was experimentally found to give high correlations with dust impact signals.

3.4.2 Training the Support Vector Machine

The 2 features (standard deviation and convolution ratio) were extracted from all observations in the training data. The decision
230 hyperplane, in this 2-dimensional case a decision line, is defined by a polynomial of degree 2 that is optimized by minimizing the non-separable SVM cost function, see e.g. Theodoridis and Koutroumbas (2009) for details. The SVM classifier was trained with a slack variable factor of 1 and equal weighting between the *dust* and *no dust* observations. Figure 4 illustrates the training of the SVM classifier.
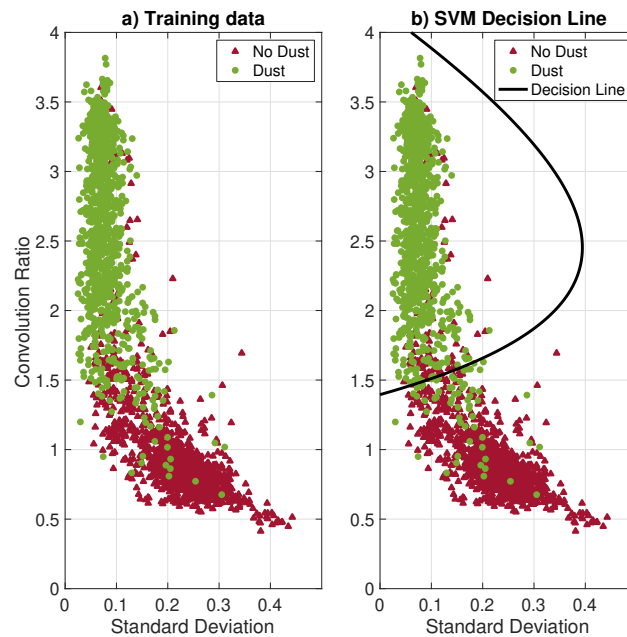
Figure 4. a) The (1x2) feature vectors extracted from all (2400) observations in the training data, the associated labels are indicated in green (*dust*) and red (*no dust*). b) The SVM decision line, the optimal second order polynomial, obtained by minimizing the non-separable SVM cost function. The SVM decision line appears to be reasonable and most observations are separable.

3.4.3 Testing the Support Vector Machine

The performance of the trained SVM classifier is evaluated using the independent testing data, i.e. the remaining manually labeled data (20 %) that was not used for training the classifier. Figure 5 presents the SVM classification performance on the testing data.

Overall, the SVM classifier achieves a classification accuracy of 94% on the testing data using the 2-dimensional feature vectors. Note that the inclusion of more extracted features could possibly enhance the SVM performance. Several additional features could be considered, such as; the mean amplitude of the signal, the range between the signal maximum and minimum values and the cross-correlation length (the time lag to the first zero crossing).

3.4.4 Explainability of the Support Vector Machine

Ideally, we want to develop a machine learning classifier that not only has a high accuracy, but also make decisions that are understandable for a human expert (Holzinger et al., 2019). In other words, we want to be able to explain why the machine learning classifier selected the predicted class for a given observation. In machine learning, this is often referred to as the explainability of the trained classifier. Figure 5 presents the testing data in the 2–D feature vector space, but this plot gives no
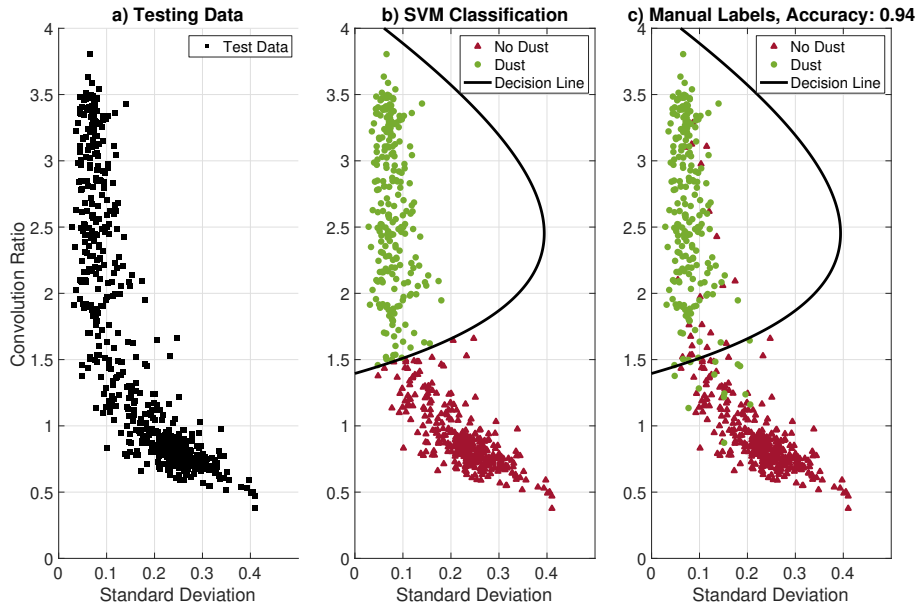
Figure 5. a) The (1x2) feature vectors extracted from the testing data (600 observations with hidden labels). b) The testing data is classified using the trained SVM decision line, where all observation within the polynomial line is classified as *dust* while all observations outside are classified as *no dust*. c) The "true" labels (from the manual labeling) are revealed. It is clear that some observations are confused, predominantly near the decision line. Still, the SVM classifier achieves an overall classification accuracy of 94%, calculated by comparing the outputs from the SVM classification (Sub-figure b) to the "true" labels (Sub-figure c).

clear indications of how different signal shapes are distributed and which signatures are confused by the SVM classifier. In
250   order to better understand the decisions made by the SVM classifier, the signal examples in Figure 1 are studied in detail. The
analysis is presented in Figure 6.

It should be noted that the signal examples in Figure 6 are not representative for the general distribution of observations
in the 2–D feature vector space, since most observations are clustered in distinct *dust* and *no dust* regions, as can be seen
255   in Figure 5. Figure 6 focuses mostly signal examples that are challenging to classify. Still, Figure 6 indicates that the SVM
classifier provides mostly comprehensible outputs, but might have difficulties classifying signals with important signatures
located at the edge of the snapshot frame.
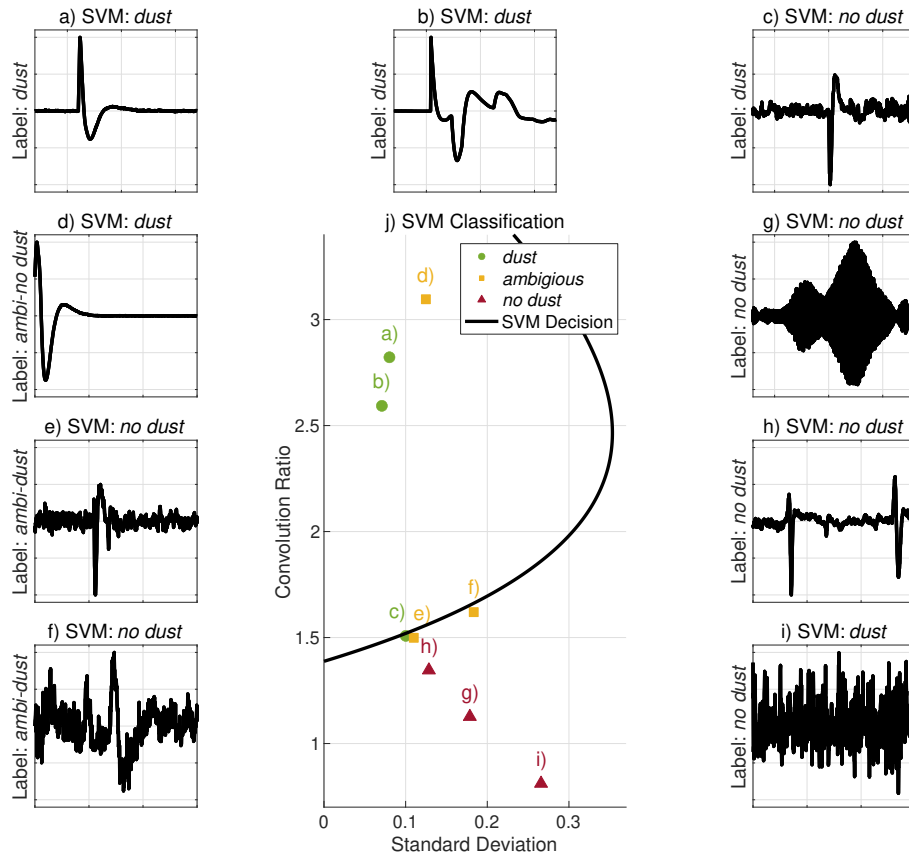
Figure 6. The signal examples are presented in Sub-figures (a-i), the manual labels are indicated along the y-axis and the predicted label, classified by the SVM decision line, are presented in the sub-plot titles. Sub-Figure j) presents the associated signal examples in the 2–D feature vector space along with the SVM decision line. The *dust* signals are illustrated in green, the *ambiguous* signals are marked in yellow and the *no dust* signals are indicated in red. The SVM classifier provides mostly explainable outputs. The clear dust signals (a-b) are located well within the SVM decision line, the *ambiguous* signals (e-f) are located near the decision line while the no dust signals (g-i) are clearly located outside. However, *dust* signal c) is erroneously located just outside the decision line, this can possibly be explained a weak signal-to-noise ratio. In addition, signal d) is located well within the decision line, although this signal is labeled *ambiguous-no dust* due to the signal framing, this indicates that the SVM might have difficulties classifying signatures located at the edge of the snapshot frame.

13

3.5 The Convolutional Neural Network (CNN)

Convolutional Neural Networks are algorithms designed for processing grid-like data and have achieved premium performance on a number of different tasks in the recent decade, such as image (He et al., 2016; Kvammen et al., 2020), video (Karpathy et al., 2014), and time series (Wang et al., 2017; Wickstrøm et al., 2021) classification.

3.5.1 Feature Extraction

Unlike the SVM, the CNN do not require pre-defined feature extraction routines. Instead, the CNN extracts the features based on a chain of convolution operations and automatically optimizes the convolution filters based on the training data and the associated labels.

For this work, we employed the 3-layer fully convolutional network architecture presented in Wang et al. (2017) and suggested for time series classification after extensive testing (Wickstrøm et al., 2022; Fawaz et al., 2020; Karim et al., 2019). The Rectified Linear Unit (ReLU) function (Glorot et al., 2011) was used as the activation function and Batch Normalization (BN) (Ioffe and Szegedy, 2015) was used at each convolutional layer in order to regularize the network and accelerate the training process. Figure 7 presents the employed CNN architecture.
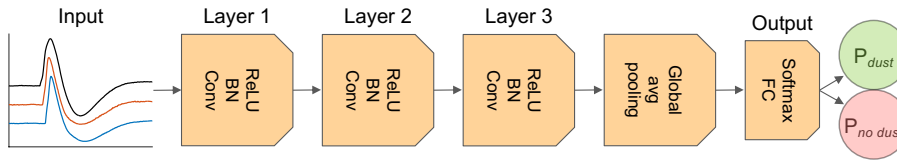
Figure 7. The 3-layer fully convolutional network used for dust impact classification. The input to the network is the (3x4096) waveform. The function that maps the input waveform to the output label: *dust* or *no dust* is defined by 3 convolutional layers, consisting of 128, 256 and 128 independent filters with kernel lengths of 8, 5 and 3 weights, respectively. Batch normalization (BN) is used at each convolutional layer to regularize the the inputs and the Rectified Linear Unit (ReLU) function was used as the activation function. Finally, the output of the convolutional layers (with dimension 128x4096) is averaged in the global pooling layer to a vector with dimension (128x1). The class score is then determined in a Fully Connected (FC) network layer and the output label probabilities (P_{dust}, $P_{no\ dust}$) are calculated using the softmax function. The Figure is adopted from Wickstrøm et al. (2021).

3.5.2 Training the Convolutional Neural Network

The 3-layer fully convolutional network consists of 267010 free parameters (weights and biases) that need to be optimized to solve the dust impact classification task. The free parameters are randomly initialized and thereafter optimized using the ADAM gradient descent optimizer (Kingma and Ba, 2014). The CNN was trained for 225 epochs with a cross-entropy loss function using the 2400 labeled observations in the training data. For more details on neural network training and optimization, see for example (Montavon et al., 2012).

3.5.3 Testing the Convolutional Neural Network

In order to visualize the features extracted by the CNN, we employ the t-distributed Stochastic Neighbor Embedding (t-SNE) method (Van der Maaten and Hinton, 2008). The t-SNE method is used for visualizing high-dimension data by assigning each observation a location in a 2–D space such that similar observations are modeled by nearby points while dissimilar observations are modeled by distant points with high probability. The (128x1) testing feature vectors, extracted in the global pooling layer, are presented in a 2–D t-SNE map in Figure 8, along with a visualization of the CNN classification performance.
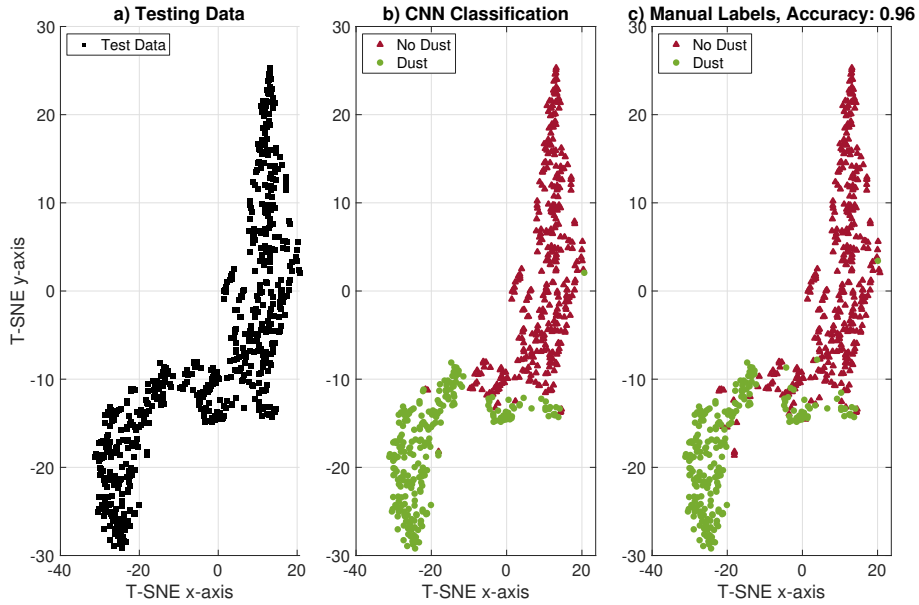
Figure 8. a) The testing data visualized by a dimension-reduced t-SNE map where similar feature vectors are modeled by nearby points while dissimilar observations are modeled by distant points with high probability. b) The testing data classified by the trained CNN. c) The "true" manual labels are presented. Only a few observations, predominantly in the transition region between the *dust* and *no dust* observations are confused. An overall classification accuracy of 96% is calculated by comparing the labels predicted by the CNN to the manual labels.

Overall, the CNN obtains a high ($\gtrsim 95\%$) classification accuracy and might therefore be suitable for automatic processing of electric field signals observed by the RPW instrument on board the Solar Orbiter.

3.5.4 Explainability of the Convolutional Neural Network

Neural networks have traditionally been regarded as black boxes (Shwartz-Ziv and Tishby, 2017; Alain and Bengio, 2016), where the network carries out the desired task, but the network decisions are difficult to interpret. However, progress have been made in recent years for making the neural network decisions more accessible and easier to interpret (i.e. explainable) for human users (Samek et al., 2021). In this section, we analyze the CNN decisions by employing Class Activation Maps and the

previously described t-SNE method.

Class Activation Maps (CAMs) (Zhou et al., 2016) highlights the regions of the data that are important for a considered label (c) by analyzing the features extracted in the global pooling layer and the weights in the FC layer that are associated with label (c), see e.g. (Wang et al., 2017) for a detailed description. The outcome of the CAM analysis is that we can visualize the sections of the signal that are influential for the CNN classification decision. Figure 9 presents the CAM analysis of the signal examples in Figure 1 along with an illustration of the signal features in a dimension-reduced t-SNE space. Note that the t-SNE mapping in Figure 9 is different from the t-SNE mapping in Figure 8, since Figure 9 considers a different CNN where the signal examples are excluded from the training data.

The CAM values in Figure 9 illustrate that the CNN make classification decisions that are comprehensible (in most cases). It is however interesting to note that signal c), manually labeled as *dust*, is erroneously classified as *no dust* by the CNN, and that this decision is largely based on the tail (the relaxation period) of the impact signal. It should however be noted that it is more difficult to explain the *no dust* predictions than the *dust* predictions since the *no dust* CNN decisions are based on the lack of a signature (*dust* impact), rather than on the presence of signature. In addition, signal d), manually labeled as *ambiguous-no dust*, is classified as *dust* by the CNN, and this decision is based on a wide region of the signal with emphasis on the tail of the (ambiguous) dust impact signal, this section might not have been highlighted as particularly important by a human expert.

In general however, the CNN achieves a high accuracy ($>95\%$) and make decisions that are mostly in-line with human interpretation. It is therefore reasonable to infer that the CNN will have a performance comparable to the agreement level between human experts, where disagreement predominantly occurs for ambiguous and noisy signals, while clear *dust* and clear *no dust* signals are classified correctly.
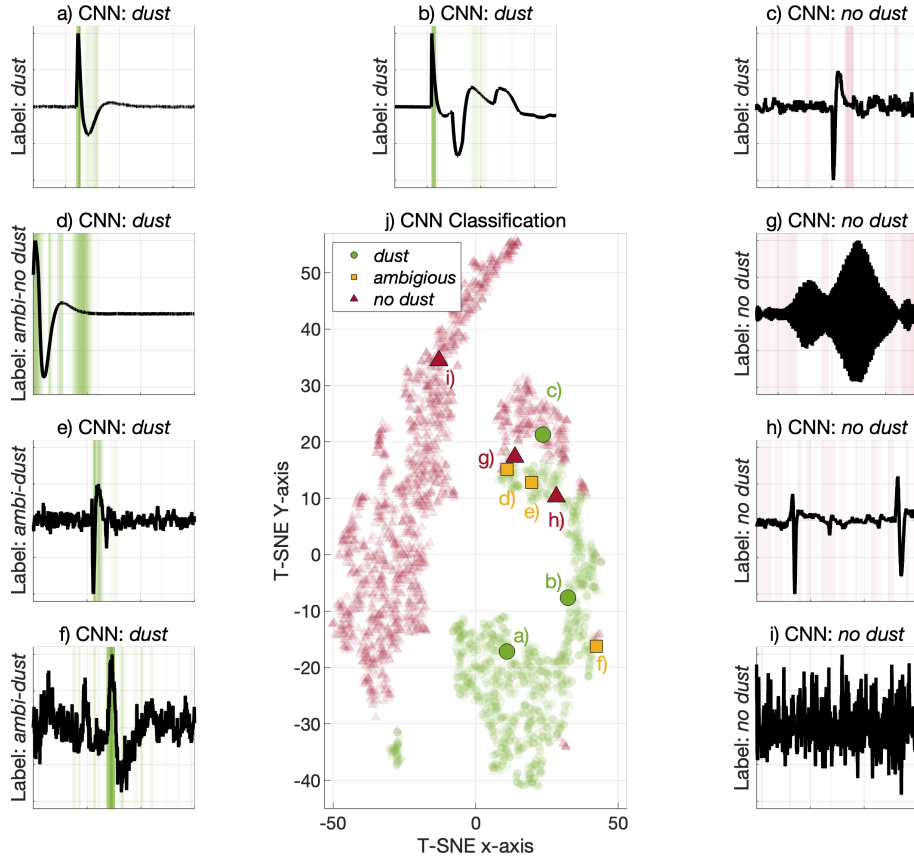
16

Figure 9. The signal examples and the CAM analysis are presented in Sub-figures (a-i), the manual labels are indicated along the y-axis and the predicted label, classified by the CNN, is presented in the sub-plot titles. Sub-figure j) presents the associated signal examples in the t-SNE space along with the training data signals as transparent points. The *dust* signals are illustrated by the green dots, the *ambiguous* signal examples are marked in yellow and the *no dust* signals are indicated in red. The CAM analysis show that the CNN emphasise the *dust* impact sections similarly to human experts, where the highlighted green regions indicate positive CAM values. Also the *no dust* CAM values (highlighted in red) are mostly understandable, although it is difficult to interpret the CNN decisions that are based on the lack of a signature (*dust* impact), rather than on the presence of signature. The t-SNE map show that the clear *dust* signals (a-b) are distinctly located in a green (*dust*) region whereas the clear *no dust* signal i) is distinctly located in a red (*no dust*) region. The remaining signals are located in more mixed regions. It should however be noted that the observations are represented by a 128 dimensional feature vector in the CNN and that the (2–D) t-SNE representation diminishes a lot of information, meaning that even the signals located in a mixed region of the t-SNE plot might be separable in the 128 dimensional feature vector space.

4 Results and Discussions

4.1 The Average Classification Performance Metrics

The average classification performance is obtained by training and testing the machine learning classifiers on 10 runs, each run with different training and testing sets. The classifiers are initialized from scratch and the testing and training sets are selected independently 10 times by randomization and splitting of the manually labeled data, as indicated by the gray circles in Figure 3. The average class-wise performance of the on-board TDS classifier and the machine learning SVM and CNN classifiers are summarized as confusion matrices in Figure 10. Overall, the CNN has the highest performance for both *dust* and *no dust* classification. In addition, both the SVM and the CNN obtain stable performance with only small variations for each run.
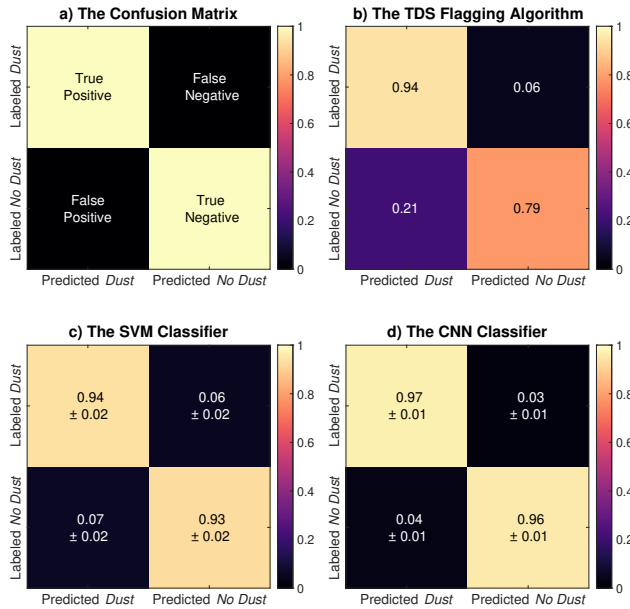
Figure 10. a) The confusion matrix entries are described by the true (correctly classified) and false (erroneously classified) values, as compared to the manual labels, positive indicate *dust* predictions and negative indicate *no dust* predictions. b) The TDS classifier confuses *dust* and *no dust* observations, where a large proportion (> 0.20) of *dust* predictions are manually labeled as *no dust*. c) The SVM classifier predicts both *dust* and *no dust* observations with a high (> 0.90) accuracy. d) The CNN classifier predicts a very large (> 0.95) proportion of both *dust* and *no dust* observations correctly.

The classification performance is further evaluated by the accuracy, precision, recall and F1 score. The definitions for the performance metrics are included in Appendix B. The average performance metrics, calculated over 10 runs, are summarized in Table 1. Again, the CNN has the highest performance across all metrics. Furthermore, the CNN obtain a significant improvement in the classification performance with a statistical significance at a level of 0.01, computed using a t-test. The t-test was

18

computed in a pairwise manner between both the CNN and the SVM, and the CNN and the TDS. In all cases, the enhanced performance of the CNN classifier was significant.

Table 1. The TDS, SVM and CNN classification performance metrics: accuracy, precision, recall and F1-score. The SVM and CNN scores and error values are the mean and the standard deviation across 10 training runs. The bold numbers indicate statistically enhanced performance with a significance level of 0.01, computed using a t-test.

Classifier	Accuracy	Precision	Recall	F1 Score
TDS	0.850	0.746	0.944	0.833
SVM	0.936 ± 0.012	0.903 ± 0.027	0.941 ± 0.017	0.921 ± 0.015
CNN	**0.964 ± 0.006**	**0.939 ± 0.020**	**0.972 ± 0.008**	**0.955 ± 0.008**

The results from both the confusion matrices and the performance metrics strongly suggest that the SVM and CNN classifiers provide binary classification results with a higher reliability than the TDS classifier. We therefore propose that the CNN classifier (or similar tools) should be considered for post-processing of the TDS data product in statistical studies of dust impacts observed by the Solar Orbiter RPW instrument. Finally, it should be noted that 134 signals (i.e. 4.5%), out of 3000 manually labeled waveforms, were marked as ambiguous, illustrated by the yellow cylinder Figure 3, and did not clearly fit into either the *dust* or *no dust* label, see Figure 1 for label examples. It is therefore improbable to achieve a classification accuracy exceeding ∼98%, and an accuracy approaching ∼99% should be considered suspicious and can be an indication of over-fitting.

4.2 The Dust Impact Rate

The trained classifiers can be used to automatically process large data sets. Figure 11 presents the TDS, SVM and CNN daily impact rates, calculated by classifying all (∼82 000) monopole triggered waveforms acquired over a one and a half year period, spanning between June 15, 2020, to December 16, 2021. The impact rate function curve is obtained by fitting the dust flux model from Zaslavsky et al. (2021) (Equation 10) with an included offset:

$$R = F_{1\mathrm{AU}} S_{col} \left(\frac{r}{1\mathrm{AU}} \right)^{-2} \frac{\nu_{\mathrm{impact}}}{\nu_\beta} \left(\frac{\nu_{\mathrm{impact}}}{\nu_{\mathrm{impact}}(1\mathrm{AU})} \right)^{\alpha\delta} + C \tag{7}$$

Where $F_{1\mathrm{AU}}$ is the unknown cumulative flux of particles above the detection threshold at 1 AU and $S_{col} = 8\mathrm{m}^2$ is the Solar Orbiter collection area, as defined in Zaslavsky et al. (2021). Furthermore, r is the radial distance from the sun, ν_{impact} is the relative velocity between the spacecraft and the dust particles, assuming a constant radial and azimuthal velocity vector: $\nu_\beta =$ [50 km/s, 0 km/s], and the product $\alpha\delta = 1.3$, as suggested in Zaslavsky et al. (2021). The assumed constant radial velocity is a good approximation for dust in hyperbolic orbits originating near the Sun that are deflected outward by the radiation pressure force. Finally, we included a constant impact rate offset: C, in order to obtain an improved fit. The description of the dust flux in Equation 7 is based on the assumption that the dust– and spacecraft orbits are in the same orbital plane.
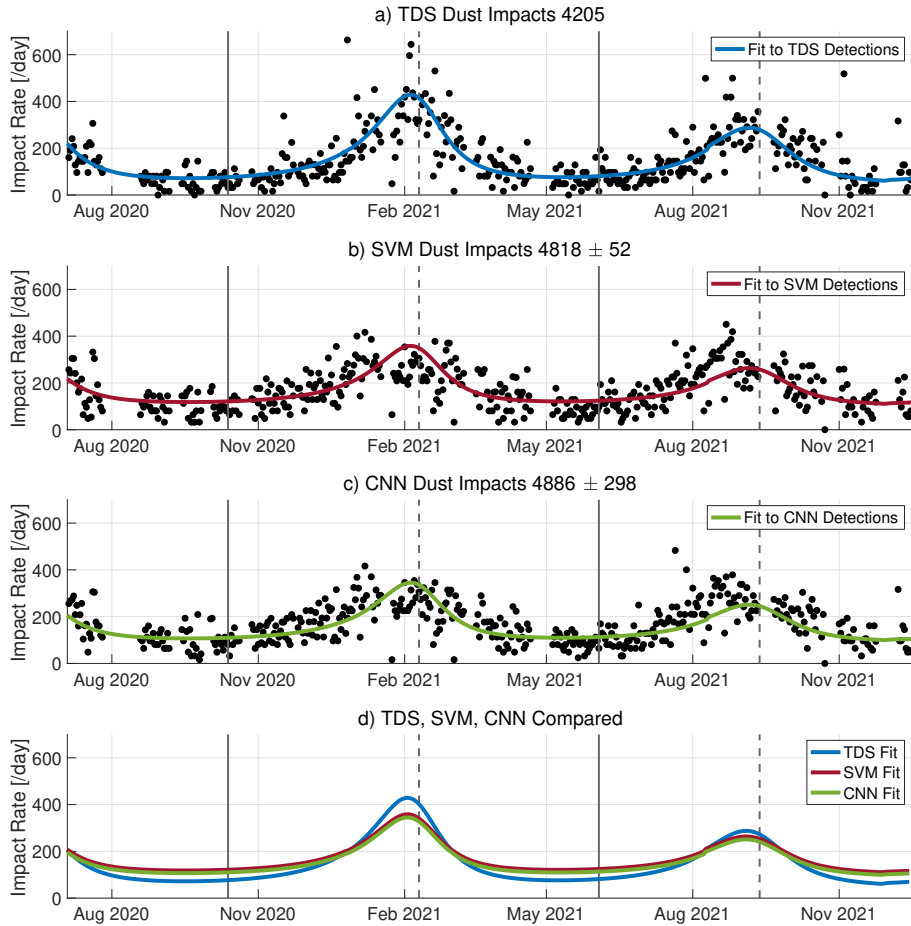
19

Figure 11. a) The daily dust impact rates according to the TDS classifier. The full vertical lines indicate times where the Solar Orbiter is at aphelion while the dashed lines indicate times at perihelion. b) The median of the daily impact rates classified by 10 trained SVM classifiers. c) The median of the daily impact rates from the 10 CNN classifiers. The impact rate function curves are obtained by fitting the dust flux model from Zaslavsky et al. (2021), Equation 7. d) The impact rate function cures are compared. The SVM and CNN dust impact rates are very similar, whereas the TDS provide notably smaller impact rates at aphelion and higher impact rates at perihelion. The daily impact rates are calculated from the daily dust impact number and the time dependent RPW duty cycle by assuming a constant impact probability for each day. The accumulated dust impact count for the TDS classification algorithm and the the mean and standard deviation of the accumulated dust impact count for the 10 CNN and SVM classifiers are presented in the sub-plot titles.

Figure 11 shows that the machine learning classifiers detected significantly more dust particles than the TDS classifier. The SVMs obtained a dust impact detection enhancement of 14% ± 1% while the CNNs had a 16% ± 7% increase. Both the SVM and the CNN classifiers obtain impact rates that are notably higher around the aphelion and distinctly lower in the vicinity of the perihelion, as compared to the dynamic range in the TDS dust impact rates.

Furthermore, Figure 11 illustrates that the fitted SVM and CNN impact rate function cures are in very good agreement. It is promising that two entirely different machine learning approaches provide comparable impact rates after classifying a large data set (consisting of ∼82 000 observations) when trained– and tested on a limited data set consisting of 3000 observations. This suggest that both the SVM and CNN classifiers have obtained stable performances and can be used to classify observations outside the domain of the training and testing data.

5 Conclusions

5.1 Summary and Scientific Implications

We have presented a machine learning-based framework for fully automated detection of dust impacts observed by the Solar Orbiter – Radio and Plasma Waves (RPW) instrument. Two different supervised machine learning approaches were considered: the Support Vector Machine (SVM) and the Convolutional Neural Network (CNN). The CNN classifier obtained the highest performance across all evaluation metrics and achieved 96% ± 1% overall classification accuracy and 94% ± 2% dust detection precision, a significant improvement to the currently used on-board TDS classification algorithm with 85% overall classification accuracy and 75% dust detection precision. We therefore conclude that the CNN classifier (or similar tools) should be considered for post-processing of the TDS data product for statistical studies of dust impacts observed by the Solar Orbiter.

The labeled data and the trained SVM and CNN classifiers are available online with included user instructions. The proposed method and the presented classifiers can thus provide the stellar dust community with thoroughly tested and more reliable data products than currently in use. It should also be noted that machine learning-based frameworks, similar to the SVM and CNN classifiers proposed in this article, can be developed for automatic processing of data acquired by radio and plasma waves instruments on-board other spacecrafts, such as: the Solar Terrestrial Relations Observatory (STEREO) (Zaslavsky et al., 2012), WIND (Malaspina et al., 2014), and the Parker Solar Probe (Szalay et al., 2020).

The SVM and CNN classifiers were used to process (∼82 000) uncalibrated monopole electric field signals acquired over a one and a half year period, spanning between June 15, 2020, to December 16, 2021. On average, the machine learning classifiers detected more dust particles than the currently used TDS algorithm, the SVMs had a 14% ± 1% detection enhancement and the CNNs had a 16% ± 7% increase. Furthermore, the SVM and CNN classifiers were in very good agreement and both classifiers obtained a notably higher dust impact rate in the vicinity of aphelion and a distinctly lower impact rate at perihelion,

21

385 as compared to the dynamic range of the TDS impact rates. This indicates a higher ambient dust distribution and/or a higher radial dust velocity than previously observed. This result is significant since it implies the presence of other dust populations in the data. Possible other populations are interstellar dust and interplanetary dust in bound orbits.

5.2 Outlook

The presented machine learning classifiers may be considered for on-board processing of the observed electric field signals.
390 However, the trained SVM and CNN classifiers presented in this article are trained on Triggered Snapshot WaveForms (TSWF) data, and should not be used for processing 'untriggered' signals without additional training and testing on 'untriggered' data. It should also be noted that the classifiers presented in this work are trained and tested on data labeled by one scientist, although with consultations with other experts. Labeled data from several experts could provide machine learning classifiers that are more in-line with the labeling consensus in the stellar dust community. Additional labeling can also be use to extended
395 the machine leaning classifiers to include automatic detection other characteristic signatures, such as: ion-acoustic, Langmuir and solitary waves.

Code and data availability. The code used for this work, the trained classifiers and the training and testing data is available at: https://github.com/AndreasKvammen/ML_dust_detection. The Triggered Snapshot WaveForms (TSWF) data files can be downloaded at: https://rpw.lesia.obspm.fr/roc/data/pub/solo/rpw/data/L2/tds_wf_e/

400 Appendix A: Graphical User Interface for Manual Labeling

Figure A1 presents the Graphical User Interface (GUI) that was used to manually label all considered (3000) signals into either *dust* or *no dust*. In addition, efforts were made to use a similar setup (with the same monitor and figure resolution) throughout the manual labeling in order to reduce bias effects.

Appendix B: The Classification Performance Metrics

405 The classification performance metrics are calculated using the True Positive (TP), True Negative (TN), False Positive (FP) and False Negative (FN) values, defined by comparing the predicted classes and the manually labeled classes, illustrated in Figure 10.

The overall accuracy of the classifier is the proportion of observations that were correctly predicted by the classifier. The
410 accuracy is mathematically defined as:

$$\text{Accuracy} = \frac{\text{TP} + \text{TN}}{\text{TP} + \text{TN} + \text{FP} + \text{FN}} \tag{B1}$$
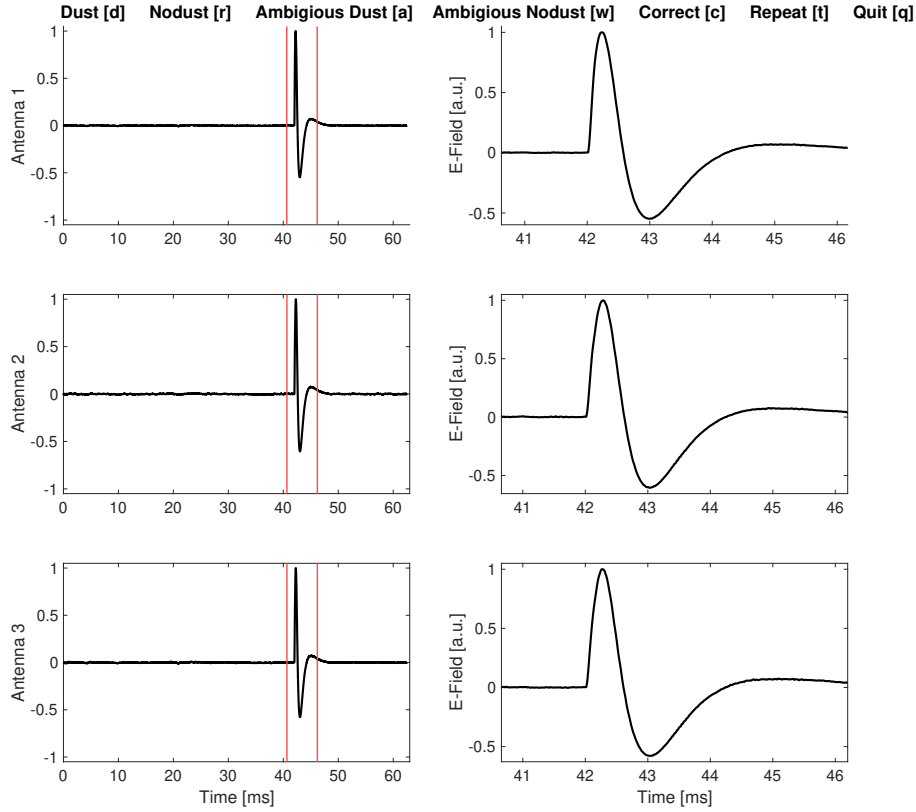
Figure A1. The manual labeling user interface showing a signal observed December 19, 2020. The left column displays the full snapshot (from 0 to ∼63 ms) at all antennas. An area of interest is selected by adjusting the red vertical lines. The right column displays the signal within the area of interest. The signal can be labeled as *dust* by pressing the [d] key on the keyboard and *no dust* by pressing the [r] key. The signal is indicated to be ambiguous if the waveform do not fit clearly into either of the two labels, note however that signals indicated to be ambiguous were also labeled into either *dust* or *no dust* using the [a] and [w] keys. There is also an option to correct [c] the previously labeled signal (in case of an error), repeat [t] the area of interest selection and quit [q] the manual labeling user interface.

Precision (in this case) is defined as the proportion of data points predicted by the classifier as *dust*, whose "true" label is indeed *dust*. Precision is therefore calculated as:

$$\text{Precision} = \frac{\text{TP}}{\text{TP} + \text{FP}} \tag{B2}$$

415   Recall (in this case) is the proportion of observations manually labeled as *dust*, that were correctly predicted as *dust* by the classifier. Recall is defined as:

$$\text{Recall} = \frac{\text{TP}}{\text{TP} + \text{FN}} \tag{B3}$$

The F1 score acts as a weighted average of precision and recall and is calculated as:

$$\text{F1} = 2 \left(\frac{\text{Precision} \cdot \text{Recall}}{\text{Precision} + \text{Recall}} \right) \tag{B4}$$

23

References

Alain, G. and Bengio, Y.: Understanding intermediate layers using linear classifier probes, ArXiv, 2016.

Aubier, M., Meyer-Vernet, N., and Pedersen, B.: Shot noise from grain and particle impacts in Saturn's ring plane, Geophysical Research Letters, 10, 5–8, 1983.

435 Boser, B. E., Guyon, I. M., and Vapnik, V. N.: A training algorithm for optimal margin classifiers, in: Proceedings of the fifth annual workshop on Computational learning theory, pp. 144–152, 1992.

Bougeret, J.-L., Kaiser, M. L., Kellogg, P. J., Manning, R., Goetz, K., Monson, S., Monge, N., Friel, L., Meetre, C., Perche, C., et al.: Waves: The radio and plasma wave investigation on the Wind spacecraft, Space Science Reviews, 71, 231–263, 1995.

Collette, A., Grün, E., Malaspina, D., and Sternovsky, Z.: Micrometeoroid impact charge yield for common spacecraft materials, Journal of
440 Geophysical Research: Space Physics, 119, 6019–6026, 2014.

Cortes, C. and Vapnik, V.: Support-vector networks, Machine learning, 20, 273–297, 1995.

Fawaz, H. I., Lucas, B., Forestier, G., Pelletier, C., Schmidt, D. F., Weber, J., Webb, G. I., Idoumghar, L., Muller, P.-A., and Petitjean, F.: InceptionTime: Finding AlexNet for time series classification, Data Mining and Knowledge Discovery, 34, 1936–1962, https://doi.org/10.1007/s10618-020-00710-y, 2020.

445 Glorot, X., Bordes, A., and Bengio, Y.: Deep Sparse Rectifier Neural Networks, in: Proceedings of the Fourteenth International Conference on Artificial Intelligence and Statistics, edited by Gordon, G., Dunson, D., and Dudík, M., vol. 15 of *Proceedings of Machine Learning Research*, pp. 315–323, PMLR, Fort Lauderdale, FL, USA, https://proceedings.mlr.press/v15/glorot11a.html, 2011.

Goodfellow, I., Bengio, Y., and Courville, A.: Deep learning, MIT press, 2016.

Gurnett, D. A., Grün, E., Gallagher, D., Kurth, W., and Scarf, F.: Micron-sized particles detected near Saturn by the Voyager plasma wave
450 instrument, Icarus, 53, 236–254, 1983.

He, K., Zhang, X., Ren, S., and Sun, J.: Deep Residual Learning for Image Recognition, in: IEEE Conference on Computer Vision and Pattern Recognition, pp. 770–778, IEEE Computer Society, https://doi.org/10.1109/CVPR.2016.90, 2016.

Holzinger, A., Langs, G., Denk, H., Zatloukal, K., and Müller, H.: Causability and explainability of artificial intelligence in medicine, Wiley Interdisciplinary Reviews: Data Mining and Knowledge Discovery, 9, e1312, 2019.

455 Hornung, K., Malama, Y. G., and Kestenboim, K. S.: Impact vaporization and ionization of cosmic dust particles, Astrophysics and Space Science, 274, 355–363, 2000.

Ioffe, S. and Szegedy, C.: Batch Normalization: Accelerating Deep Network Training by Reducing Internal Covariate Shift, in: nternational Conference on Machine Learning, edited by Bach, F. and Blei, D., vol. 37 of *Proceedings of Machine Learning Research*, pp. 448–456, PMLR, Lille, France, https://proceedings.mlr.press/v37/ioffe15.html, 2015.

460 Ishimoto, H.: Modeling the number density distribution of interplanetary dust on the ecliptic plane within 5AU of the Sun, Astronomy and Astrophysics, 362, 1158–1173, 2000.

Karim, F., Majumdar, S., Darabi, H., and Harford, S.: Multivariate LSTM-FCNs for time series classification, Neural Networks, 116, 237–245, https://doi.org/10.1016/j.neunet.2019.04.014, 2019.

Karpathy, A., Toderici, G., Shetty, S., Leung, T., Sukthankar, R., and Fei-Fei, L.: Large-Scale Video Classification with
465 Convolutional Neural Networks, in: 2014 IEEE Conference on Computer Vision and Pattern Recognition, pp. 1725–1732, https://doi.org/10.1109/CVPR.2014.223, 2014.

Kingma, D. and Ba, J.: Adam: A Method for Stochastic Optimization, in: International Conference on Learning Representations, 2014.

Kvammen, A., Wickstrøm, K., McKay, D., and Partamies, N.: Auroral image classification with deep neural networks, Journal of Geophysical Research: Space Physics, 125, e2020JA027 808, 2020.

470 Maksimovic, M., Bale, S., Chust, T., Khotyaintsev, Y., Krasnoselskikh, V., Kretzschmar, M., Plettemeier, D., Rucker, H., Souček, J., Steller, M., et al.: The solar orbiter radio and plasma waves (rpw) instrument, Astronomy & Astrophysics, 642, A12, 2020.

Malaspina, D., Horányi, M., Zaslavsky, A., Goetz, K., Wilson III, L., and Kersten, K.: Interplanetary and interstellar dust observed by the Wind/WAVES electric field instrument, Geophysical Research Letters, 41, 266–272, 2014.

Malaspina, D. M., Szalay, J. R., Pokornỳ, P., Page, B., Bale, S. D., Bonnell, J. W., de Wit, T. D., Goetz, K., Goodrich, K., Harvey, P. R., et al.:
475 In situ observations of interplanetary dust variability in the inner heliosphere, The Astrophysical Journal, 892, 115, 2020.

Mann, I. and Czechowski, A.: Dust destruction and ion formation in the inner solar system, The Astrophysical Journal, 621, L73, 2005.

Mann, I. and Czechowski, A.: Dust observations from Parker Solar Probe: dust ejection from the inner Solar System, Astronomy & Astrophysics, 650, A29, 2021.

Mann, I., Kimura, H., Biesecker, D. A., Tsurutani, B. T., Grün, E., McKibben, R. B., Liou, J.-C., MacQueen, R. M., Mukai, T., Guhathakurta,
480 M., et al.: Dust near the Sun, Space science reviews, 110, 269–305, 2004.

Mann, I., Nouzák, L., Vaverka, J., Antonsen, T., Fredriksen, Å., Issautier, K., Malaspina, D., Meyer-Vernet, N., Pavlů, J., Sternovsky, Z., Stude, J., Ye, S., and Zaslavsky, A.: Dust observations with antenna measurements and its prospects for observations with Parker Solar Probe and Solar Orbiter, Annales Geophysicae, 37, 1121–1140, https://doi.org/10.5194/angeo-37-1121-2019, 2019.

Montavon, G., Orr, G. B., and Müller, K.-R., eds.: Neural Networks: Tricks of the Trade, Springer Berlin Heidelberg,
485 https://doi.org/10.1007/978-3-642-35289-8, 2012.

Müller, D., Cyr, O. S., Zouganelis, I., Gilbert, H. R., Marsden, R., Nieves-Chinchilla, T., Antonucci, E., Auchère, F., Berghmans, D., Horbury, T., et al.: The solar orbiter mission-science overview, Astronomy & Astrophysics, 642, A1, 2020.

Samek, W. et al.: Explaining Deep Neural Networks and Beyond: A Review of Methods and Applications, Proceedings of the IEEE, pp. 247–278, 2021.

490 Shwartz-Ziv, R. and Tishby, N.: Opening the Black Box of Deep Neural Networks via Information, ArXiv, abs/1703.00810, 2017.

Soucek, J., Píša, D., Kolmasova, I., Uhlir, L., Lan, R., Santolík, O., Krupar, V., Kruparova, O., Baše, J., Maksimovic, M., et al.: Solar Orbiter Radio and Plasma Waves–Time Domain Sampler: In-flight performance and first results, Astronomy & Astrophysics, 656, A26, 2021.

Szalay, J., Pokornỳ, P., Bale, S., Christian, E., Goetz, K., Goodrich, K., Hill, M., Kuchner, M., Larsen, R., Malaspina, D., et al.: The near-sun dust environment: initial observations from parker solar probe, The Astrophysical Journal Supplement Series, 246, 27, 2020.

495 Theodoridis, S. and Koutroumbas, K.: Chapter 3 - Linear Classifiers, in: Pattern Recognition (Fourth Edition), edited by Theodoridis, S. and Koutroumbas, K., pp. 91 – 150, Academic Press, Boston, fourth edition edn., https://doi.org/https://doi.org/10.1016/B978-1-59749-272-0.50004-9, 2009.

Trosten, D. J., Strauman, A. S., Kampffmeyer, M., and Jenssen, R.: Recurrent Deep Divergence-based Clustering for Simultaneous Feature Learning and Clustering of Variable Length Time Series, in: ICASSP 2019 - 2019 IEEE International Conference on Acoustics, Speech
500 and Signal Processing (ICASSP), pp. 3257–3261, https://doi.org/10.1109/ICASSP.2019.8682365, 2019.

Van der Maaten, L. and Hinton, G.: Visualizing data using t-SNE., Journal of machine learning research, 9, 2008.

Vaverka, J., Pellinen-Wannberg, A., Kero, J., Mann, I., De Spiegeleer, A., Hamrin, M., Norberg, C., and Pitkänen, T.: Potential of earth orbiting spacecraft influenced by meteoroid hypervelocity impacts, IEEE Transactions on Plasma Science, 45, 2048–2055, 2017.

Vech, D. and Malaspina, D. M.: A novel machine learning technique to identify and categorize plasma waves in spacecraft measurements,
505 Journal of Geophysical Research: Space Physics, 126, e2021JA029 567, 2021.

Villar, J. R., Vergara, P., Menéndez, M., de la Cal, E., González, V. M., and Sedano, J.: Generalized Models for the Classification of Abnormal Movements in Daily Life and its Applicability to Epilepsy Convulsion Recognition, International Journal of Neural Systems, 26, 1650 037, https://doi.org/10.1142/s0129065716500374, 2016.

Wang, Z., Yan, W., and Oates, T.: Time series classification from scratch with deep neural networks: A strong baseline, in: 2017 International joint conference on neural networks (IJCNN), pp. 1578–1585, IEEE, 2017.

Wickstrøm, K., Mikalsen, K. Ø., Kampffmeyer, M., Revhaug, A., and Jenssen, R.: Uncertainty-Aware Deep Ensembles for Reliable and Explainable Predictions of Clinical Time Series, IEEE Journal of Biomedical and Health Informatics, 25, 2435–2444, https://doi.org/10.1109/JBHI.2020.3042637, 2021.

Wickstrøm, K., Kampffmeyer, M., Mikalsen, K. Ø., and Jenssen, R.: Mixing up contrastive learning: Self-supervised representation learning for time series, Pattern Recognition Letters, 155, 54–61, https://doi.org/10.1016/j.patrec.2022.02.007, 2022.

Zaslavsky, A.: Floating potential perturbations due to micrometeoroid impacts: Theory and application to S/WAVES data, Journal of Geophysical Research: Space Physics, 120, 855–867, 2015.

Zaslavsky, A., Meyer-Vernet, N., Mann, I., Czechowski, A., Issautier, K., Le Chat, G., Pantellini, F., Goetz, K., Maksimovic, M., Bale, S., et al.: Interplanetary dust detection by radio antennas: Mass calibration and fluxes measured by STEREO/WAVES, Journal of Geophysical Research: Space Physics, 117, 2012.

Zaslavsky, A., Mann, I., Soucek, J., Czechowski, A., Píša, D., Vaverka, J., Meyer-Vernet, N., Maksimovic, M., Lorfèvre, E., Issautier, K., et al.: First dust measurements with the Solar Orbiter Radio and Plasma Wave instrument, Astronomy & Astrophysics, 656, A30, 2021.

Zhou, B., Khosla, A., Lapedriza, A., Oliva, A., and Torralba, A.: Learning deep features for discriminative localization, in: Proceedings of the IEEE conference on computer vision and pattern recognition, pp. 2921–2929, 2016.

BIBLIOGRAPHY

Altobelli, N., S. Kempf, M. Landgraf, R. Srama, V. Dikarev, H. Krüger, G. Moragas-Klostermeyer, and E. Grün (Oct. 2003). "Cassini between Venus and Earth: Detection of interstellar dust." In: *Journal of Geophysical Research (Space Physics)* 108.A10, 8032, p. 8032. DOI: 10.1029/2003JA009874.

Aubier, M. G., N. Meyer-Vernet, and B. M. Pedersen (Jan. 1983). "Shot noise from grain and particle impacts in Saturn's ring plane." In: *Geophysical Research Letters* 10.1, pp. 5–8. DOI: 10.1029/GL010i001p00005.

Auer, Seigfried (2001). "Instrumentation." In: *Interplanetary Dust*, p. 385.

Baguhl, M., E. Grün, R. Riemann, P. Staubach, and D. P. Hamilton (June 1995). "Interstellar Dust Measurements with the Ulysses and Galileo Dust Detectors." In: *AAS/Division for Planetary Sciences Meeting Abstracts #27*. Vol. 27. AAS/Division for Planetary Sciences Meeting Abstracts, 40.10, p. 40.10.

Bale, S. D., P. J. Kellogg, D. E. Larsen, R. P. Lin, K. Goetz, and R. P. Lepping (Jan. 1998). "Bipolar electrostatic structures in the shock transition region: Evidence of electron phase space holes." In: *Geophysical Research Letters* 25.15, pp. 2929–2932. DOI: 10.1029/98GL02111.

Bale, S. D. et al. (Apr. 2008). "The Electric Antennas for the STEREO/WAVES Experiment." In: *Space Science Reviews* 136.1-4, pp. 529–547. DOI: 10.1007/s11214-007-9251-x.

Belheouane, S., A. Zaslavsky, N. Meyer-Vernet, K. Issautier, I. Mann, and M. Maksimovic (Nov. 2012). "Detection of Interstellar Dust with STEREO/WAVES at 1 AU." In: *Solar Physics* 281.1, pp. 501–506. DOI: 10.1007/s11207-012-9995-7.

Berg, O. E. and F. F. Richardson (Jan. 1969). "The Pioneer 8 cosmic dust experiment." In: *Review of Scientific Instruments* 40, pp. 1333–1337. DOI: 10.1063/1.1683778.

Bertaux, J. L. and J. E. Blamont (July 1976). "Possible evidence for penetration of interstellar dust into the Solar System." In: *Nature* 262.5566, pp. 263–266. DOI: 10.1038/262263a0.

Bougeret, J. L. et al. (Feb. 1995). "Waves: The Radio and Plasma Wave Investigation on the Wind Spacecraft." In: *Space Science Reviews* 71.1-4, pp. 231–263. DOI: 10.1007/BF00751331.

Bougeret, J. L. et al. (Apr. 2008). "S/WAVES: The Radio and Plasma Wave Investigation on the STEREO Mission." In: *Space Science Reviews* 136.1-4, pp. 487–528. DOI: 10.1007/s11214-007-9298-8.

Burns, J. A., P. L. Lamy, and S. Soter (Oct. 1979). "Radiation forces on small particles in the solar system." In: 40.1, pp. 1–48. DOI: 10.1016/0019-1035(79)90050-2.

Collette, A., E. Grün, D. Malaspina, and Z. Sternovsky (Aug. 2014). "Micrometeoroid impact charge yield for common spacecraft materials." In: *Journal of Geophysical Research (Space Physics)* 119.8, pp. 6019–6026. DOI: 10.1002/2014JA020042.

Collette, A., G. Meyer, D. Malaspina, and Z. Sternovsky (July 2015). "Laboratory investigation of antenna signals from dust impacts on spacecraft." In: *Journal of Geophysical Research (Space Physics)* 120.7, pp. 5298–5305. DOI: 10.1002/2015JA021198.

Draine, B. T. and H. M. Lee (Oct. 1984). "Optical Properties of Interstellar Graphite and Silicate Grains." In: *The Astrophysical Journal* 285, p. 89. DOI: 10.1086/162480.

Fletcher, Alex, Sigrid Close, and Donovan Mathias (Sept. 2015). "Simulating plasma production from hypervelocity impacts." In: *Physics of Plasmas* 22.9, 093504, p. 093504. DOI: 10.1063/1.4930281.

Getachew, Tibebu, Ilpo Virtanen, and Kalevi Mursula (Nov. 2017). "Structure of the Photospheric Magnetic Field During Sector Crossings

of the Heliospheric Magnetic Field." In: *Solar Physics* 292.11, 174, p. 174. DOI: 10.1007/s11207-017-1198-9.

Giese, R. H. (Mar. 1973). "Optical properties of single-component zodiacal light models." In: *Planetary and Space Science* 21.3, pp. 513–521. DOI: 10.1016/0032-0633(73)90048-2.

Gruen, E., B. Gustafson, I. Mann, M. Baguhl, G. E. Morfill, P. Staubach, A. Taylor, and H. A. Zook (June 1994). "Interstellar dust in the heliosphere." In: *Astronomy and Astrophysics* 286, pp. 915–924.

Grün, E., B. A. S. Gustafson, S. Dermott, and H. Fechtig (2001). *Interplanetary Dust*.

Grun, E., H. A. Zook, H. Fechtig, and R. H. Giese (May 1985). "Collisional balance of the meteoritic complex." In: 62.2, pp. 244–272. DOI: 10.1016/0019-1035(85)90121-6.

Grun, E. et al. (Apr. 1993). "Discovery of Jovian dust streams and interstellar grains by the Ulysses spacecraft." In: *Nature* 362.6419, pp. 428–430. DOI: 10.1038/362428a0.

Grün, E. et al. (Oct. 1997). "South-North and Radial Traverses through the Interplanetary Dust Cloud." In: 129.2, pp. 270–288. DOI: 10.1006/icar.1997.5789.

Grün, Eberhard, Ralf Srama, Harald Krüger, Sascha Kempf, Valeri Dikarev, Stefan Helfert, and Georg Moragas-Klostermeyer (Mar. 2005). "2002 Kuiper prize lecture: Dust Astronomy." In: 174.1, pp. 1–14. DOI: 10.1016/j.icarus.2004.09.010.

Gurnett, D. A., J. A. Ansher, W. S. Kurth, and L. J. Granroth (Oct. 1997). *Micron-Sized Dust Particles Detected in the Outer Solar System by the Voyager 1 and 2 Plasma Wave Instruments*. National Aeronautics and Space Administration Report.

Gurnett, D. A., E. Grun, D. Gallagher, W. S. Kurth, and F. L. Scarf (Feb. 1983). "Micron-sized particles detected near Saturn by the Voyager plasma wave instrument." In: 53.2, pp. 236–254. DOI: 10.1016/0019-1035(83)90145-8.

Gurnett, D. A., W. S. Kurth, F. L. Scarf, J. A. Burns, J. N. Cuzzi, and E. Grün (Dec. 1987). "Micron-sized particle impacts detected near Uranus by the Voyager 2 plasma wave instrument." In: *Journal of Geophysical Research* 92.A13, pp. 14959–14968. DOI: 10.1029/JA092iA13p14959.

Gurnett, D., W. Kurth, G. Hospodarsky, A. Persoon, and J. Cuzzi (Dec. 2004). "Evidence of Meteoroid Impacts on the Rings from Cassini Plasma Wave Measurements." In: *AGU Fall Meeting Abstracts*. Vol. 2004, P51C-06, P51C–06.

Gustafson, B. A. S. (Jan. 1994). "Physics of Zodiacal Dust." In: *Annual Review of Earth and Planetary Sciences* 22, pp. 553–595. DOI: 10.1146/annurev.ea.22.050194.003005.

Gustafson, B. A. S. and S. M. Lederer (Jan. 1996). "Interstellar Grain Flow Through the Solar Wind Cavity around 1992." In: *IAU Colloq. 150: Physics, Chemistry, and Dynamics of Interplanetary Dust*. Ed. by Bo A. S. Gustafson and Martha S. Hanner. Vol. 104. Astronomical Society of the Pacific Conference Series, p. 35.

Henri, P., N. Meyer-Vernet, C. Briand, and S. Donato (Aug. 2011). "Observations of Langmuir ponderomotive effects using the Solar TErrestrial RElations Observatory spacecraft as a density probe." In: *Physics of Plasmas* 18.8, pp. 082308–082308. DOI: 10.1063/1.3622667.

Horányi, M. et al. (Dec. 2014). "The Lunar Dust Experiment (LDEX) Onboard the Lunar Atmosphere and Dust Environment Explorer (LADEE) Mission." In: *Space Science Reviews* 185.1-4, pp. 93–113. DOI: 10.1007/s11214-014-0118-7.

Horanyi, Mihaly (Jan. 1996). "Charged Dust Dynamics in the Solar System." In: 34, pp. 383–418. DOI: 10.1146/annurev.astro.34.1.383.

Issautier, K., C. Perche, S. Hoang, C. Lacombe, M. Maksimovic, J. L. Bougeret, and C. Salem (Jan. 2005). "Solar wind electron density and temperature over solar cycle 23: Thermal noise measurements

on Wind." In: *Advances in Space Research* 35.12, pp. 2141–2146. DOI: 10.1016/j.asr.2005.04.085.

Jackson, J. D. (1962). *Classical Electrodynamics*.

Kellogg, P. J., K. Goetz, and S. J. Monson (Feb. 2016). "Dust impact signals on the wind spacecraft." In: *Journal of Geophysical Research (Space Physics)* 121.2, pp. 966–991. DOI: 10.1002/2015JA021124.

Kellogg, Paul J., Steven J. Monson, Keith Goetz, Robert L. Howard, Jean-Louis Bougeret, and Michael L. Kaiser (Jan. 1996). "Early Wind observations of bow shock and foreshock waves." In: *Geophysical Research Letters* 23.10, pp. 1243–1246. DOI: 10.1029/96GL01067.

Krüger, Harald, Markus Landgraf, Nicolas Altobelli, and Eberhard Grün (June 2007). "Interstellar Dust in the Solar System." In: *Space Science Reviews* 130.1-4, pp. 401–408. DOI: 10.1007/s11214-007-9181-7. arXiv: 0706.3110 [astro-ph].

Kurth, W. S., T. F. Averkamp, D. A. Gurnett, and Z. Wang (Aug. 2006). "Cassini RPWS observations of dust in Saturn's E Ring." In: *Planetary and Space Science* 54.9-10, pp. 988–998. DOI: 10.1016/j.pss.2006.05.011.

Kvammen, A. et al. (2022). "Machine Learning Detection of Dust Impact Signals Observed by The Solar Orbiter." In: *EGUsphere* 2022, pp. 1–27. DOI: 10.5194/egusphere-2022-725. URL: https://egusphere.copernicus.org/preprints/egusphere-2022-725/.

Landgraf, M. (Jan. 1998). PhD thesis. -.

— (May 2000). "Modeling the motion and distribution of interstellar dust inside the heliosphere." In: *Journal of Geophysical Research* 105.A5, pp. 10303–10316. DOI: 10.1029/1999JA900243. arXiv: astro-ph/9906300 [astro-ph].

Landgraf, M. and E. Grün (1998). "In Situ Measurements of Interstellar Dust." In: *IAU Colloq. 166: The Local Bubble and Beyond*. Ed. by Dieter Breitschwerdt, Michael J. Freyberg, and Joachim Truemper. Vol. 506, pp. 381–384. DOI: 10.1007/BFb0104750.

Lee, N. et al. (June 2012). "Measurements of Freely-Expanding Plasma From Hypervelocity Impacts." In: *International Journal of Impact Engineering* 44, pp. 40–49. DOI: 10.1016/j.ijimpeng.2012.01.002.

Lhotka, Christoph, Nazish Rubab, Owen W. Roberts, Justin C. Holmes, Klaus Torkar, and Rumi Nakamura (Oct. 2020). "Charging time scales and magnitudes of dust and spacecraft potentials in space plasma scenarios." In: *Physics of Plasmas* 27.10, 103704, p. 103704. DOI: 10.1063/5.0018170.

Malaspina, D. M., M. Horányi, A. Zaslavsky, K. Goetz, L. B. Wilson, and K. Kersten (Jan. 2014). "Interplanetary and interstellar dust observed by the Wind/WAVES electric field instrument." In: *Geophysical Research Letters* 41.2, pp. 266–272. DOI: 10.1002/2013GL058786.

Malaspina, David M., Iver H. Cairns, and Robert E. Ergun (July 2011). "Dependence of Langmuir wave polarization on electron beam speed in type III solar radio bursts." In: *Geophysical Research Letters* 38.13, L13101, p. L13101. DOI: 10.1029/2011GL047642.

Malaspina, David M. et al. (Apr. 2020). "In Situ Observations of Interplanetary Dust Variability in the Inner Heliosphere." In: *The Astrophysical Journal* 892.2, 115, p. 115. DOI: 10.3847/1538-4357/ab799b.

Mann, I., A. Czechowski, H. Kimura, M. Köhler, T. Minato, and T. Yamamoto (Jan. 2006). "Physical properties of the dust in the Solar System and its interrelation with small bodies." In: *Asteroids, Comets, Meteors*. Ed. by Daniela Lazzaro, Sylvio Ferraz-Mello, and Julio Angel Fernández. Vol. 229, pp. 41–65. DOI: 10.1017/S1743921305006678.

Mann, Ingrid (Jan. 2009). "Meteors." In: *Landolt Börnstein* 4B, p. 563. DOI: 10.1007/978-3-540-88055-4_29.

Mann, Ingrid and Andrzej Czechowski (Sept. 2004). "Dust grain dynamics in and around the heliosphere." In: *Physics of the Outer Heliosphere*. Ed. by Vladimir Florinski, Nikolai V. Pogorelov, and Gary P. Zank. Vol. 719. American Institute of Physics Conference Series, pp. 53–58. DOI: 10.1063/1.1809498.

Mann, Ingrid, Andrzej Czechowski, and Nicole Meyer-Vernet (Mar. 2010). "Dust In The Interplanetary Medium-Interactions With The Solar Wind." In: *Twelfth International Solar Wind Conference*. Ed. by M. Maksimovic, K. Issautier, N. Meyer-Vernet, M. Moncuquet, and F. Pantellini. Vol. 1216. American Institute of Physics Conference Series, pp. 491–496. DOI: 10.1063/1.3395911.

Mann, Ingrid, Alexander Krivov, and Hiroshi Kimura (2000). "Dust Cloud near the Sun." In: *Icarus* 146.2, pp. 568–582. ISSN: 0019-1035. DOI: https://doi.org/10.1006/icar.2000.6419. URL: https://www.sciencedirect.com/science/article/pii/S0019103500964194.

Mann, Ingrid et al. (Dec. 2019). "Dust observations with antenna measurements and its prospects for observations with Parker Solar Probe and Solar Orbiter." In: *Annales Geophysicae* 37.6, pp. 1121–1140. DOI: 10.5194/angeo-37-1121-2019.

McBride, N. and J. a. m. McDonnell (Aug. 1999). "Meteoroid impacts on spacecraft:. sporadics, streams, and the 1999 Leonids." In: *Planetary and Space Science* 47.8-9, pp. 1005–1013. DOI: 10.1016/S0032-0633(99)00023-9.

McDonnell, J. A. M. (1978). *Cosmic dust*.

Meyer-Vernet, N. (Jan. 1985). "Comet Giacobini-Zinner diagnosis from radio measurements." In: *Advances in Space Research* 5.12, pp. 37–46. DOI: 10.1016/0273-1177(85)90065-1.

Meyer-Vernet, N., M. G. Aubier, and B. M. Pedersen (July 1986). "Voyager 2 at Uranus: Grain impacts in the ring plane." In: *Geophysical Research Letters* 13.7, pp. 617–620. DOI: 10.1029/GL013i007p00617.

Meyer-Vernet, N., A. Lecacheux, M. L. Kaiser, and D. A. Gurnett (Feb. 2009). "Detecting nanoparticles at radio frequencies: Jovian dust stream impacts on Cassini/RPWS." In: *Geophysical Research Letters* 36.3, L03103, p. L03103. DOI: 10.1029/2008GL036752.

Meyer-Vernet, N., M. Moncuquet, K. Issautier, and A. Lecacheux (Apr. 2014). "The importance of monopole antennas for dust observations: Why Wind/WAVES does not detect nanodust." In: *Geophysi-*

cal Research Letters 41.8, pp. 2716–2720. DOI: 10.1002/2014GL059988. arXiv: 1404.2498 [astro-ph.EP].

Meyer-Vernet, N., M. Moncuquet, K. Issautier, and P. Schippers (Jan. 2017). "Frequency range of dust detection in space with radio and plasma wave receivers: Theory and application to interplanetary nanodust impacts on Cassini." In: *Journal of Geophysical Research (Space Physics)* 122.1, pp. 8–22. DOI: 10.1002/2016JA023081.

Meyer-Vernet, Nicole and Arnaud Zaslavsky (Jan. 2012). "In Situ Detection of Interplanetary and Jovian Nanodust with Radio and Plasma Wave Instruments." In: *Nanodust in the Solar System: Discoveries and Interpretations*. Ed. by Ingrid Mann, Nicole Meyer-Vernet, and Andrzej Czechowski. Vol. 385. Astrophysics and Space Science Library, p. 133. DOI: 10.1007/978-3-642-27543-2_7.

Morfill, G. E. and E. Grün (Oct. 1979). "The motion of charged dust particles in interplanetary space - II. Interstellar grains." In: *Planetary and Space Science* 27.10, pp. 1283–1292. DOI: 10.1016/0032-0633(79)90106-5.

O'Shea, E., Z. Sternovsky, and D. M. Malaspina (Dec. 2017). "Interpreting Dust Impact Signals Detected by the STEREO Spacecraft." In: *Journal of Geophysical Research (Space Physics)* 122.12, pp. 11,864–11,873. DOI: 10.1002/2017JA024786.

Oberc, P. (Jan. 1996). "Electric antenna as a dust detector." In: *Advances in Space Research* 17.12, pp. 105–110. DOI: 10.1016/0273-1177(95)00766-8.

Oberc, P., W. Parzydlo, and O. L. Vaisberg (July 1990). "Correlations between the Vega 2 plasma wave (APV-N) and dust (SP-1) observations at Comet Halley." In: 86.1, pp. 314–326. DOI: 10.1016/0019-1035(90)90221-T.

Page, Brent et al. (Feb. 2020). "Examining Dust Directionality with the Parker Solar Probe FIELDS Instrument." In: *The Astrophysical Journal, Supplement Series* 246.2, 51, p. 51. DOI: 10.3847/1538-4365/ab5f6a.

Parker, E. N. (Nov. 1958). "Dynamics of the Interplanetary Gas and Magnetic Fields." In: *The Astrophysical Journal* 128, p. 664. DOI: 10. 1086/146579.

Poynting, J. H. (Nov. 1903). "Radiation in the solar system : its effect on temperature and its pressure on small bodies." In: *Monthly Notices of the Royal Astronomical Society* 64, p. 1.

Pusack, A., D. M. Malaspina, J. R. Szalay, S. D. Bale, Keith Goetz, Robert J. MacDowall, and Marc Pulupa (Oct. 2021). "Dust Directionality and an Anomalous Interplanetary Dust Population Detected by the Parker Solar Probe." In: *The Planetary Science Journal* 2.5, 186, p. 186. DOI: 10.3847/PSJ/ac0bb9.

Rackovic Babic, K., A. Zaslavsky, K. Issautier, N. Meyer-Vernet, and D. Onic (Mar. 2022). "An analytical model for dust impact voltage signals and its application to STEREO/WAVES data." In: *Astronomy and Astrophysics* 659, A15, A15. DOI: 10.1051/0004-6361/ 202142508.

Shen, Mitchell M., Zoltan Sternovsky, Alessandro Garzelli, and David M. Malaspina (Sept. 2021). "Electrostatic Model for Antenna Signal Generation From Dust Impacts." In: *Journal of Geophysical Research (Space Physics)* 126.9, e29645, e29645. DOI: 10.1029/2021JA029645.

Simpson, J. A. and A. J. Tuzzolino (May 1985). "Polarized polymer films as electronic pulse detectors of cosmic dust particles." In: *Nuclear Instruments and Methods in Physics Research A* 236.1, pp. 187–202. DOI: 10.1016/0168-9002(85)90145-7.

Srama, R. et al. (Sept. 2004). "The Cassini Cosmic Dust Analyzer." In: *Space Science Reviews* 114.1-4, pp. 465–518. DOI: 10.1007/s11214-004-1435-z.

Sterken, V. J., N. Altobelli, S. Kempf, G. Schwehm, R. Srama, and E. Grün (Feb. 2012). "The flow of interstellar dust into the solar system." In: *Astronomy and Astrophysics* 538, A102, A102. DOI: 10.1051/0004-6361/201117119.

Thayer, Frederick M., David M. Malaspina, Andrew Collette, and Zoltan Sternovsky (2016). "Variation in relative dust impact charge recollection with antenna to spacecraft potential on STEREO." In: *Journal of Geophysical Research: Space Physics* 121.6, pp. 4998–5004. DOI: https://doi.org/10.1002/2015JA021983. eprint: https://agupubs.onlinelibrary.wiley.com/doi/pdf/10.1002/2015JA021983. URL: https://agupubs.onlinelibrary.wiley.com/doi/abs/10.1002/2015JA021983.

Vaverka, Jakub, Takuji Nakamura, Johan Kero, Ingrid Mann, Alexandre De Spiegeleer, Maria Hamrin, Carol Norberg, Per-Arne Lindqvist, and Asta Pellinen-Wannberg (2018). "Comparison of Dust Impact and Solitary Wave Signatures Detected by Multiple Electric Field Antennas Onboard the MMS Spacecraft." In: *Journal of Geophysical Research: Space Physics* 123.8, pp. 6119–6129. DOI: https://doi.org/10.1029/2018JA025380. eprint: https://agupubs.onlinelibrary.wiley.com/doi/pdf/10.1029/2018JA025380. URL: https://agupubs.onlinelibrary.wiley.com/doi/abs/10.1029/2018JA025380.

Vaverka, Jakub, Jiří Pavlů, Libor Nouzák, Jana Šafránková, Zdeněk Němeček, Ingrid Mann, Shengyi Ye, and Per-Arne Lindqvist (Nov. 2019). "One-Year Analysis of Dust Impact-Like Events Onto the MMS Spacecraft." In: *Journal of Geophysical Research (Space Physics)* 124.11, pp. 8179–8190. DOI: 10.1029/2019JA027035.

Wilck, M. and I. Mann (May 1996). "Radiation pressure forces on "typical" interplanetary dust grains." In: *Planetary and Space Science* 44.5, pp. 493–499. DOI: 10.1016/0032-0633(95)00151-4.

Wilson Lynn, III (June 2020). "Wind WAVES TDSF Dataset, version 3.0." In: *Zenodo Wind WAVES TDSF Dataset*. Vol. 56, p. 36737. DOI: 10.5281/zenodo.5636737.

Witte, M. (Nov. 2004). "Kinetic parameters of interstellar neutral helium. Review of results obtained during one solar cycle with the Ulysses/GAS-instrument." In: *Astronomy and Astrophysics* 426, pp. 835–844. DOI: 10.1051/0004-6361:20035956.

Wood, S. R., David M. Malaspina, Laila Andersson, and Mihaly Horanyi (2015). "Hypervelocity dust impacts on the Wind spacecraft: Correlations between Ulysses and Wind interstellar dust detections." In: *Journal of Geophysical Research: Space Physics* 120.9, pp. 7121–7129. DOI: https://doi.org/10.1002/2015JA021463. eprint: https://agupubs.onlinelibrary.wiley.com/doi/pdf/10.1002/2015JA021463. URL: https://agupubs.onlinelibrary.wiley.com/doi/abs/10.1002/2015JA021463.

Ye, S.-Y., T. F. Averkamp, W. S. Kurth, M. Brennan, S. Bolton, J. E. P. Connerney, and J. L. Joergensen (2020). "Juno Waves Detection of Dust Impacts Near Jupiter." In: *Journal of Geophysical Research: Planets* 125.6. e2019JE006367 2019JE006367, e2019JE006367. DOI: https://doi.org/10.1029/2019JE006367. eprint: https://agupubs.onlinelibrary.wiley.com/doi/pdf/10.1029/2019JE006367. URL: https://agupubs.onlinelibrary.wiley.com/doi/abs/10.1029/2019JE006367.

Ye, S.-Y., D. A. Gurnett, W. S. Kurth, T. F. Averkamp, S. Kempf, H.-W. Hsu, R. Srama, and E. Grün (2014). "Properties of dust particles near Saturn inferred from voltage pulses induced by dust impacts on Cassini spacecraft." In: *Journal of Geophysical Research: Space Physics* 119.8, pp. 6294–6312. DOI: https://doi.org/10.1002/2014JA020024. eprint: https://agupubs.onlinelibrary.wiley.com/doi/pdf/10.1002/2014JA020024. URL: https://agupubs.onlinelibrary.wiley.com/doi/abs/10.1002/2014JA020024.

Ye, S. Y. et al. (Oct. 2018). "Dust Observations by the Radio and Plasma Wave Science Instrument During Cassini's Grand Finale." In: *Geophysical Research Letters* 45.19, pp. 10,101–10,109. DOI: 10.1029/2018GL078059.

Ye, S.–Y., D.A. Gurnett, and W.S. Kurth (2016a). "In-situ measurements of Saturn's dusty rings based on dust impact signals detected by Cassini RPWS." In: *Icarus* 279. Planetary Rings, pp. 51–61. ISSN: 0019-1035. DOI: https://doi.org/10.1016/j.icarus.2016.05.

006. URL: https://www.sciencedirect.com/science/article/pii/S0019103516301427.

Zaslavsky, A. (Feb. 2015). "Floating potential perturbations due to micrometeoroid impacts: Theory and application to S/WAVES data." In: *Journal of Geophysical Research (Space Physics)* 120.2, pp. 855–867. DOI: 10.1002/2014JA020635.

Zaslavsky, A. et al. (May 2012). "Interplanetary dust detection by radio antennas: Mass calibration and fluxes measured by STEREO/WAVES." In: *Journal of Geophysical Research (Space Physics)* 117.A5, A05102, A05102. DOI: 10.1029/2011JA017480.

Zaslavsky, A. et al. (Dec. 2021). "First dust measurements with the Solar Orbiter Radio and Plasma Wave instrument." In: *Astronomy and Astrophysics* 656, A30, A30. DOI: 10.1051/0004-6361/202140969. arXiv: 2104.09974 [physics.space-ph].

Zel'Dovich, Ya. B. (Jan. 1968). "EMF Produced by a Shock Wave Moving in a Dielectric." In: *Soviet Journal of Experimental and Theoretical Physics* 26, p. 159.

BIOGRAFIJA

Kristina Racković Babić rođena je 18.08.1984 godine u Čačku. Osnovnu školu kao i gimnaziju završila je Čačku. Školske 2003/2004. godine upisala je osnovne studije na Matematičkom fakultetu Univerziteta u Beogradu, smer Astronomija gde je 2011. godine stekla diplomu. Školske 2015/2016. upisala je doktorske akademske studije na istom fakultetu. Školske 2018/2019. započela je doktorske akademske studije po principu komentorstva u saradnji između Univerziteta u Beogradu i Pariske Opservatorije.

U periodu 2009–2011. godine angažovana je kao nastavnik za nacionalne i međunarodne astronomske i astrofizičke olimpijade od strane Srpskog astronomskog društva, podržano od strane Ministarstva prosvete, nauke i tehnološkog razvoja (osvojene zlatna, srebrna i bronzana medalja na Olimpijskim igrama na Krimu 2010. godine). U periodu 2011–2016 godine bila je angažovana kao nastavnik matematike u srednjoj školi. U periodu 2016–2018. je angažovana kao saradnjik u nastavi na Katedri za Astronomiju Matematičkog fakulteta na predmetima: Osnovi astronomije, Racionalna mehanika 1, Opšta astronomija-praktikum. Od 17.10.2018. godine angažovana je na Matematičkom fakultetu Univerziteta u Beogradu sa zvanjem istraživač pripravnik na projektu Ministarstva prosvete, nauke i tehnološkog razvoja Republike Srbije, broj III44002 "Astroinformatika: primena IT u astronomiji i srodnim oblastima", pod rukovodstvom dr Darka Jevremoviča.

Naučno istraživački rad kandidatkinje se odvija u oblasti detekcije kosmičke prašine radio instrumentima u okviru nekoliko svemirskih letelica. Kandidatkinja je koautor 3 naučna rada u časopisima sa SCI liste, samostalnog rada objavljenog u međunarodnom časopisu sa recenzijom i 5 radova prikazanih na naučnim skupovima.

Изјава о ауторству

Име и презиме аутора   Кристина Рацковић Бабић

Број индекса   2023/2015

Изјављујем

да је докторска дисертација под насловом

Непосредна детекција космичке прашине радио-уређајима свемирских летелица

- резултат сопственог истраживачког рада;
- да дисертација у целини ни у деловима није била предложена за стицање друге дипломе према студијским програмима других високошколских установа;
- да су резултати коректно наведени и
- да нисам кршио/ла ауторска права и користио/ла интелектуалну својину других лица.

Потпис аутора

У Београду, 09.11.2022.

Изјава о истоветности штампане и електронске верзије докторског рада

Име и презиме аутора   Кристина Рацковић Бабић

Број индекса   2023/2015

Студијски програм   Астрономија и астрофизика

Наслов рада   Непосредна детекција космичке прашине радио-уређајима свемирских летелица

Ментори   Karine Issautier, Душан Онић

Изјављујем да је штампана верзија мог докторског рада истоветна електронској верзији коју сам предао/ла ради похрањена у **Дигиталном репозиторијуму Универзитета у Београду.**

Дозвољавам да се објаве моји лични подаци везани за добијање академског назива доктора наука, као што су име и презиме, година и место рођења и датум одбране рада.

Ови лични подаци могу се објавити на мрежним страницама дигиталне библиотеке, у електронском каталогу и у публикацијама Универзитета у Београду.

Потпис аутора

У Београду, 09.11.2022.

Изјава о коришћењу

Овлашћујем Универзитетску библиотеку „Светозар Марковић" да у Дигитални репозиторијум Универзитета у Београду унесе моју докторску дисертацију под насловом:

Непосредна детекција космичке прашине радио-уређајима свемирских летелица

која је моје ауторско дело.

Дисертацију са свим прилозима предао/ла сам у електронском формату погодном за трајно архивирање.

Моју докторску дисертацију похрањену у Дигиталном репозиторијуму Универзитета у Београду и доступну у отвореном приступу могу да користе сви који поштују одредбе садржане у одабраном типу лиценце Креативне заједнице (Creative Commons) за коју сам се одлучио/ла.

1. Ауторство (CC BY)

2. Ауторство – некомерцијално (CC BY-NC)

3. Ауторство – некомерцијално – без прерада (CC BY-NC-ND)

4. Ауторство – некомерцијално – делити под истим условима (CC BY-NC-SA)

5. Ауторство – без прерада (CC BY-ND)

6. Ауторство – делити под истим условима (CC BY-SA)

(Молимо да заокружите само једну од шест понуђених лиценци.
 Кратак опис лиценци је саставни део ове изјаве).

Потпис аутора

У Београду, 09.11.2022

1. **Ауторство**. Дозвољавате умножавање, дистрибуцију и јавно саопштавање дела, и прераде, ако се наведе име аутора на начин одређен од стране аутора или даваоца лиценце, чак и у комерцијалне сврхе. Ово је најслободнија од свих лиценци.

2. **Ауторство – некомерцијално**. Дозвољавате умножавање, дистрибуцију и јавно саопштавање дела, и прераде, ако се наведе име аутора на начин одређен од стране аутора или даваоца лиценце. Ова лиценца не дозвољава комерцијалну употребу дела.

3. **Ауторство – некомерцијално – без прерада**. Дозвољавате умножавање, дистрибуцију и јавно саопштавање дела, без промена, преобликовања или употребе дела у свом делу, ако се наведе име аутора на начин одређен од стране аутора или даваоца лиценце. Ова лиценца не дозвољава комерцијалну употребу дела. У односу на све остале лиценце, овом лиценцом се ограничава највећи обим права коришћења дела.

 4. **Ауторство – некомерцијално – делити под истим условима**. Дозвољавате умножавање, дистрибуцију и јавно саопштавање дела, и прераде, ако се наведе име аутора на начин одређен од стране аутора или даваоца лиценце и ако се прерада дистрибуира под истом или сличном лиценцом. Ова лиценца не дозвољава комерцијалну употребу дела и прерада.

5. **Ауторство – без прерада**. Дозвољавате умножавање, дистрибуцију и јавно саопштавање дела, без промена, преобликовања или употребе дела у свом делу, ако се наведе име аутора на начин одређен од стране аутора или даваоца лиценце. Ова лиценца дозвољава комерцијалну употребу дела.

6. **Ауторство – делити под истим условима**. Дозвољавате умножавање, дистрибуцију и јавно саопштавање дела, и прераде, ако се наведе име аутора на начин одређен од стране аутора или даваоца лиценце и ако се прерада дистрибуира под истом или сличном лиценцом. Ова лиценца дозвољава комерцијалну употребу дела и прерада. Слична је софтверским лиценцама, односно лиценцама отвореног кода.